

**Microtubules Dual Chemo- and Thermo-Responsive Depolymerization
&
Optimization of Noncovalent Loading of Vinblastine on Single-Walled
Carbon Nanotube**

by

© Zixian Li

A thesis submitted to the School of Graduate Studies
in partial fulfillment of the requirements for the degree of

Master of Science in Pharmacy

School of Pharmacy

Memorial University of Newfoundland

January 2016

St. John's, Newfoundland and Labrador, Canada

Abstract

The effects of the chemotherapeutic agent vinblastine versus the low temperature of 277 K on the structure of $\alpha\beta$ -tubulin heterodimer were investigated by means of molecular dynamics simulations. Individual experiments have shown that vinblastine-bound heterodimer, and its apo structure under low temperature of 277 K, both undergo conformational changes toward destabilization of the dimer as compared to the apo tubulin at 300 K. Both factors exhibit weakening the longitudinal interactions of tubulin heterodimer through displacing dimer interfacial segments, resulting in the dominant electrostatic repulsion at the interface of the subunits. The two independent factors of temperature and anti-mitotic agent facilitate folding alterations in the functional segments of H1-S2 loop, H3, H10 helices and T7 loop, which are known to be important in either longitudinal or lateral contacts among $\alpha\beta$ -heterodimers in microtubule protofilaments and the depolymerization mechanism of microtubules.

Carbon nanotubes have become one of the candidates for transporting drugs to target sites, because of their size scale, huge surface area and high cellular uptake. Many experimental studies of carbon nanotube drug delivery have been performed in the past decade. The delivery studies of vinblastine and its target microtubule are important, because of the significant role of vinblastine in cancer therapy. However, the interactions between vinblastine and carbon nanotubes have yet to be investigated. The computational studies of the interactions between vinblastine and carbon nanotubes under different conditions are presented in this thesis. The vinblastine-carbon nanotube interactions have been studied from the following perspectives: loading capacity (one to three vinblastine

molecules loaded); tube structure (armchair, chiral and zigzag tubes); tube functionalization; and temperature variations (277 K and 300 K). The functionalization of carbon nanotubes strengthened the drug-carrier interactions of all systems at 300 K. The functionalized carbon nanotubes of armchair type were identified suitable for drug delivery at both 277 K and 300 K, due to the relatively strong drug-carrier interactions. The functionalized chiral nanotubes were found especially useful for delivery at 277 K due to the enhanced drug-carrier interactions at this temperature.

Acknowledgement

I am very grateful to my supervisor Dr. Laleh Alisaraie for giving me the opportunity to work with her. Without her encouragement, patience and guidance, I cannot finish the program and my thesis.

I would like to thank Dr. Oliver Stueker for his kind help on writing *Python* scripts.

I would like to thank the support from my lab members: Zahed, Nathan, Brandon, Blake, Tiffany, Maria and Kali.

I would like to thank the School of Graduate Studies Memorial University of Newfoundland for partial stipend support.

This work was supported, with funding for stipend, hardware and software, by the Research & Development Corporation of Newfoundland and Labrador.

Dedicated to my beloved wife, parents and sister...

Table of Contents

Abstract	ii
Acknowledgement	iv
Table of Contents	vi
List of Figures	x
List of Tables	xiii
List of Abbreviations	xiv
CHAPTER 1 Introduction	1
1.1 Cancer	1
1.1.1 Cancerous cells	2
1.1.2 Mitosis in normal eukaryotic cells	4
1.1.3 Apoptosis	6
1.2 Microtubules	7
1.2.1 Structure and functions	7
1.2.2 Dynamic behaviors	9
1.3 Microtubule-targeted agents	11
1.3.1 Microtubule stabilizers	11
1.3.2 Microtubule destabilizers	12
1.4 Carbon nanotubes	14
1.4.1 Structure	14

1.4.2	Applications	16
1.5	Computer modeling	18
1.5.1	Molecular Docking	18
1.5.2	Molecular dynamics simulations	21
1.6	Summary	26
1.7	Bibliography	27
CHAPTER 2 Drug Binding Site at Tubulin Heterodimer and Dimer		
	Deploymerization	38
2.1	Introduction	38
2.2	Materials and Methods	41
2.2.1	<i>In silico</i> experimental setup	41
2.2.2	Molecular dynamics (MD) simulations	43
2.3	Results and Discussions	44
2.3.1	DOX binding site prediction by <i>Ghecom</i> and <i>FlexX</i>	44
2.3.2	VLB bound $\alpha\beta$ -tubulin heterodimer	46
2.3.3	MD simulation analysis	49
2.3.4	VLB-induced conformational changes	50
2.3.5	Cold-induced conformational changes	53
2.3.6	Solvent accessible surface area of heterodimer	55

2.3.7	Curvature change of heterodimer	58
2.3.8	Electrostatic potential map at the interface	62
2.4	Conclusions	66
2.5	Bibliography	68
CHAPTER 3 Interactions of Vinblastine with Single-Walled Carbon Nanotubes		
76		
3.1	Introduction	76
3.2	Materials and Methods	80
3.3	Results and Discussions	84
3.3.1	CNT-1VLB systems	84
3.3.2	CNT-2VLB systems	90
3.3.3	CNT-3VLB systems	94
3.3.4	Interaction energy levels	103
3.3.5	Effect of functionalization	104
3.3.6	Effect of temperature	106
3.4	Conclusions	107
3.5	Bibliography	108
CHAPTER 4 Summary		115
List of Appendices		117

Appendix A	118
Appendix B	127
Appendix C	131
Appendix D	133
Appendix E	138

List of Figures

Figure 1.1 Confocal immunomicrographs of HeLa cells with microtubules (green) and DNA (red) in the process of cell division.	5
Figure 1.2 Scheme of MT structure and dynamics.	9
Figure 1.3 Confocal microscopy images of cancer cells revealing the drug effects.	13
Figure 1.4 Schematic depiction of CNT formation by wrapping a graphene sheet.	15
Figure 1.5 Scheme of bonded interactions.	23
Figure 2.1 Chemical structure of mono-protonated VLB.	42
Figure 2.2 DOX binding site prediction.	45
Figure 2.3 VLB binding site.	48
Figure 2.4 The RMSD plots of the unliganded heterodimer at 300 K (black), 277 K (red) and the liganded heterodimer at 300 K (blue) within 115 ns of MD simulations.	50
Figure 2.5 Main conformational changes of the liganded heterodimer compared to the unliganded heterodimer at 300 K.	51
Figure 2.6 Major structural changes of the unliganded heterodimer at different temperatures.	54
Figure 2.7 SASA of α - and β -tubulin in three systems varying over the 115 ns simulation time.	56
Figure 2.8 Helicity plots, (A) H12 in α - and β -tubulin, (B) H5 in α -tubulin.	57
Figure 2.9 The curvature of $\alpha\beta$ -tubulin heterodimer represented by H7 orientation.	60
Figure 2.10 The surface electrostatic potential map in vacuum of the unliganded and liganded $\alpha\beta$ -heterodimer.	65

Figure 3.1 The LJ interactions between CNT and VLB for (A) SWNT-1VLB_Out and (B) fSWNT-1VLB_Out at 300 K (black) and 277 K (red), respectively.....	84
Figure 3.2 Stable VLB orientations with respect to the CNT sidewall for SWNT-1VLB system at (A) 300 K and (B) 277 K, and for fSWNT-1VLB system at (C) 300 K and (D) 277 K.....	87
Figure 3.3 The LJ interactions between CNT and VLB at (A) SWNT-1VLB_In and (B) fSWNT-1VLB_In under 300 K (black) and 277 K (red), respectively.	88
Figure 3.4 Stable orientations of encapsulated VLB with respect to CNT sidewall for SWNT-1VLB at (A) 300 K and (B) 277 K, and for fSWNT-1VLB at (C) 300 K and (D) 277 K.....	89
Figure 3.5 The LJ interactions between CNT and VLBs for SWNT-2VLB under (A) 300 K and (B) 277 K as well as for fSWNT-2VLB under (C) 300 K and (D) 277 K, respectively.	91
Figure 3.6 Stable orientations at SWNT-2VLB of (A) VLB1 and (B) VLB2 at 300 K as well as (C) VLB1 and (D) VLB2 at 277 K with respect to SWNT sidewall.....	92
Figure 3.7 The LJ interactions between CNT and VLBs at fArmchair-3VLB under (A) 300 K and (B) 277 K, respectively.	95
Figure 3.8 Stable orientations of (A) VLB1, (B) VLB2 and (C) VLB3 at 300 K with respect to fArmchair SWNT.	96
Figure 3.9 (A) LJ and (B) Coulomb interactions between fArmchair SWNT and VLB3 in the process of VLB3 entering the tube.	97

Figure 3.10 The LJ interactions between CNT and VLBs in fChiral-3VLB at (A) 300 K and (B) 277 K, respectively. 99

Figure 3.11 The LJ interactions between CNT and VLB molecules of fZigzag-3VLB at (A) 300 K and (B) 277 K, respectively..... 101

Figure 3.12 The stable orientations of VLB corresponding to different energy levels. 104

List of Tables

Table 2.1 $\Delta G_{\text{binding}}$ of the DOX docking experiments.....	46
Table 2.2 The amino acids compose the interacting network of VLB in the first ranked docking solution.....	49
Table 3.1 Composition of various sets of CNT–VLB simulation systems.	81
Table 3.2 Parameters for simulating CNT using OPLS-AA force field.	83

List of Abbreviations

ATB: Automated Topology Builder

CHO: Chinese hamster ovarian

CNT: carbon nanotube

COM: center-of-mass

DCOM: distance between centers of mass

DOX: doxorubicin

EPR: enhanced permeability and retention

E-site: exchangeable nucleotide site

fSWNT: functionalized single-walled carbon nanotube

GDP: guanosine diphosphate

GTP: guanosine triphosphate

LINCS: LINear Constraint Solver

LJ: Lennard-Jones

MAP: microtubule-associated protein

MD: molecular dynamics

M phase: mitotic phase

MT: microtubule

MWNT: multi-walled carbon nanotube

NMR: nuclear magnetic resonance

OPLS-AA: optimized potentials for liquid simulations all-atom

PDB: Protein Data Bank

PEG: poly(ethylene glycol)
PMF: potential of mean forces
PTX: paclitaxel
RES: reticuloendothelial system
RMSD: root mean square deviation
SASA: solvent accessible surface area
SLD: stathmin-like domain
SWNT: single-walled carbon nanotube
TEM: transmission electron micrograph
vdW: van der Waals
VLB: vincalokoblastine
WHO: World Health Organization

CHAPTER 1

Introduction

1.1 Cancer

Cancer is a class of diseases which can be traced back to alterations of specific genes.¹⁻² Such genome alterations are progressively developed by accumulative exposure to carcinogenic agents including chemicals, viruses and other environmental factors, such as ultraviolet radiation in the case of skin cancer.³ Although the properties of cancer vary from one type to another, cancerous cells share some common features regardless of their tissues of origin. At the cellular level, the notorious characteristic of cancerous cells is uncontrolled growth. It is the way of responding to stimulatory or inhibitory growth signals that differs cancerous cells from normal cells, rather than the capacity of growth.⁴ Stimulated by growth signaling molecules, such as diffusible growth factors, extracellular matrix components, and intercellular adhesion/interaction molecules, normal cells grow and divide at a rate comparable to their malignant counterparts; their growth and division are stopped by inhibitory growth signals under control. Conversely, cancerous cells can grow and divide even in the absence of the growth signaling molecules required for the proliferation of normal cells. They generate growth signals without depending on the signaling of normal cells and keep proliferating out of the control of normal cell

inhibitory signaling and, consequently, either a benign or malignant lump is formed at the growth site.^{2, 4} Chemotherapy and radiotherapy are conventional and powerful approaches for cancer treatment, in combination with tumor removal surgery.⁵⁻⁶ Both chemo- and radio-therapy are intended to block the fast growth of tumor cells. Chemotherapy suppresses the fast-dividing cancerous cells mainly through two strategies: interruption of DNA replication and perturbation on mitotic spindles.⁷ Radiotherapy, as another surgery adjuvant treatment, generates high-energy ionized particle to induce the breakage of single- and double-stranded DNA of cancerous cells.⁸ Under certain treatment, mitosis, the core part of cell proliferation, is arrested because the therapy-induced programmed cell death, also known as apoptosis, leading to the exit of the cell cycle.⁹ Therefore, tumor shrinkage is observed and proliferation of cancerous cells is gradually brought under control. Currently, chemotherapy still lacks specificity to target only cancerous cells without affecting normal cells. The shortcomings of commonly used anti-cancer therapeutics are seen from the side effects accompanied with the treatment, including symptoms such as nausea, hair loss and extreme fatigue.⁴

1.1.1 Cancerous cells

Apart from the loss of controlled growth, several other features also distinguish cancer as a class of complicated diseases. Tumor progression requires activated expression of the enzyme telomerase.² Tumor cells failing to express telomerase would undergo telomere shrinkage, lose chromosome ends and, eventually, die out. Only tumor cells with reactivated telomerase expression undergo indefinite division. Normal cells, on the other hand, usually lack telomerase activity; therefore, the telomeres of chromosomes get

shortened after each division. When telomere shortening reaches a critical point, triggering the inhibitory signal to cease continued growth, the cell division process stops.²

The deep cause of uncontrollable cell growth lies in the mutations of DNA. Four types of genes control the cell division process: proto-oncogenes, tumor suppressor genes, DNA-repair genes and suicide genes.^{2, 10-11} Proto-oncogenes act as an accelerator to promote cell proliferations. Tumor suppressor genes, on the contrary, act as a brake to stop growth. The mutations occurring in proto-oncogenes and tumor suppressor genes lead to the conversion of proto-oncogenes to oncogenes, as well as the loss of function on controllable growth, and thus transform a cell from the normal state to the malignant state. Furthermore, the mutations on DNA repair genes deactivate their functions of damage repair and defect correction. If the damage is beyond repair, the checkpoint mechanism signals toward cell death.¹⁰ Mutations in suicide genes cannot perform the action of cell death called by the checkpoint mechanism, which gives the cell with unrepaired genetic damage a chance to escape apoptosis, continue cell division and transform into a cancerous cell. Cancerous cells thus undergo infinite proliferation, leading to the formation of a lump or a massive tissue.¹¹

Another feature is that tumor cells have a special microenvironment different from normal cells, which triggers their independent growth. Tumor cells produce their own growth signals which are less dependent on exogenous growth stimulation, to interfere with the mechanism ensuring proper cell behaviors. The original site where cancerous cells grow is called the primary site. The new invaded sites are called secondary sites.¹² The invasion ability makes cancer cells spread to adjacent and distant tissues. Cancer

cells attach to a new site when the adhesion between cells and the extracellular matrix changes, and the interactions between cancer cells and primary sites are weakened. Cancer cells at the primary site send some pioneering molecules to nearby or remote sites to change the microenvironment, making it easier for tumor cells to attach. As cancer cells become aggressive, they spread and stick to normal healthy tissues and thus begin invasion to other sites. The uncontrolled growth on secondary sites rather than the primary site is the major cause of death.¹²

1.1.2 Mitosis in normal eukaryotic cells

The dividing cells go through a series of stages which are referred to as the cell cycle. The complete cell cycle includes “Interphase” and the “Mitotic phase” (M phase). Most of the time of the cell cycle is spent on the interphase; M phase, also known as the process of mitosis, accounts for only a small portion of the cell cycle.¹³ During mitosis in eukaryotes, a parent cell completes DNA duplication and the replicated chromosomes are equally segregated into two identical daughter cells at the final stage of M phase called cytokinesis. Although mitosis is a short stage of the cell cycle, it is further divided into 5 sub-stages: prophase, prometaphase, metaphase, anaphase and telophase. When cell division starts, chromosomes encoded with genetic information are in the form of pairs of replicated sister chromatids linked by proteins called cohesins.¹³ During prophase, chromatids condense and the nuclear envelope breaks down so that condensed chromatids are released to the cytoplasm. At prometaphase, chromatids get attached to microtubules of the mitotic spindles through proteins called kinetochores. The mitotic checkpoint signaling is active at this stage. At metaphase, mitotic spindles direct

chromosomes to congress at the central plane known as the metaphase plate. The mitotic checkpoint signal decays and eventually deactivates, then the anaphase promoting complex, an E3 ubiquitin ligase, gets activated and triggers the next stage of anaphase.¹⁴ Anaphase includes two steps: anaphase A and anaphase B. During anaphase A, the protease, called separase, cleaves cohesins and causes the separation of sister chromatids. Chromosomes segregate during this stage. At anaphase B, the mitotic spindles elongate and push the segregated identical chromatids toward each pole. Telophase is the final stage of mitosis; nuclear envelopes reform followed by the decondensation of chromosomes. The step of cytokinesis follows mitosis, where the cell is divided into two daughter cells that enter interphase.¹³⁻¹⁵ (**Figure 1.1**)

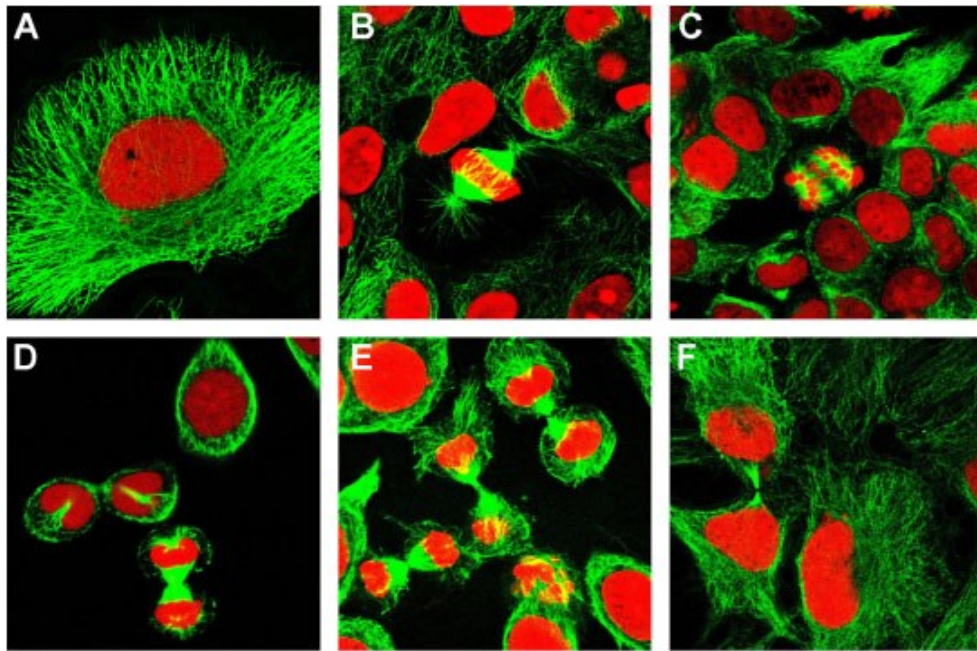


Figure 1.1 Confocal immunomicrographs of HeLa cells with microtubules (green) and DNA (red) in the process of cell division. (A) interphase, (B) metaphase, (C) anaphase,

(D) telophase, (E) initiation of the middle-body formation and (F) cytokinesis. (From Stanton *et al.*, 2011)¹⁴ This figure is adapted with permission.

The precision of chromosome alignment and segregation is crucial for the success of mitosis. A single error in the alignment or partitioning of chromosomes can prevent further progression of cell division, and lead to the arrested state ending in the mitotic checkpoint-induced apoptosis.

1.1.3 Apoptosis

Apoptosis, known as programmed cell death, is an essential process equally as important as cell division and cell migration. Apoptosis is a highly regulated self-destruction program to keep cell number and tissue size in rigorous control by eliminating over-produced and dysfunctional (aberrant) cells. It is also a self-defense mechanism to minimize the potential risk to the integrity of a cellular environment.¹⁶

The morphologic changes occurring in apoptosis include compaction and segregation of nuclear chromatin, condensation of cytoplasm, the convolution of the nuclear and cell outlines, nuclear breakdown into discrete fragments, and surface protuberance forming membrane-enclosed apoptotic bodies. The apoptotic bodies are ingested by neighboring cells and degraded in lysosomes.¹⁷ In chemotherapy, tumor regression and side effects are both caused by the enhanced extensive apoptosis induced by chemotherapeutic agents.¹⁸

The deregulated proliferation and suppressed apoptosis are the hallmarks of cancer. Accordingly, two strategies are used for cancer treatment: therapies targeting mitotic spindles to block the tumor growth by interfering with mitosis, and therapies inducing

extensive apoptosis of tumor cells. However, neither strategy has achieved the goal of confining death to cancer cells and allowing the survival of normal cells, because of the confusion caused by the similar proliferative features existing in some normal tissues such as gut epithelium and bone marrow. In order to reduce the adverse effects on normal organs and tissues, further research is still required for a deeper understanding of cancer.¹⁹

1.2 Microtubules

Microtubules (MTs), along with actin and intermediate filaments, are the three major cytoskeleton components. Cytoskeleton organizes cell contents, connects cells with their external environment, and regulates cell motility as well as morphology.²⁰ Among the three filamentous proteins, MT is the largest, with the diameter around 24 nm. Actin is the smallest type of filament, with the diameter around 7 nm. Intermediate filament, as the name implies, is mid-sized, with the diameter around 10 nm.²¹

1.2.1 Structure and functions

MT appears as a hollow tube consisting of α - and β -tubulin subunits. Both tubulin monomers are very similar globular proteins. They associate together via non-covalent bonding and form heterodimers as building blocks of MT. Tubulin heterodimers string together forming long strands called protofilaments. The alternating assembly of α - and β -tubulins leads to structural polarity of the linear protofilaments. Normally, 13 parallel protofilaments associate side-by-side and form the cylindrical tube.²² The assembled tubular structure has one end with the exposure of α -tubulins and the other end with the

exposure of β -tubulins. The polarity of MT is defined by denoting the α -tubulin end as minus (–) end and the β -tubulin end as plus (+) end. Each tubulin monomer binds to a guanosine triphosphate (GTP) molecule. The GTP molecule bound to α -tubulin is non-exchangeable, while the GTP molecule bound to β -tubulin is exchangeable. The polymerization of MT is driven by the hydrolysis of GTP binding to the subunit of β -tubulin. Only dimers with GTP at the exchangeable site can polymerize. GTP is hydrolyzed to guanosine diphosphate (GDP) and the nucleotide becomes non-exchangeable.²³ Another tubulin isoform, γ -tubulin, acts as a template for the correct assembly of MT.²⁴ The γ -tubulin ring complex forms a capping protein at the minus end to modulate the minus end dynamics.²⁵ (**Figure 1.2A**)

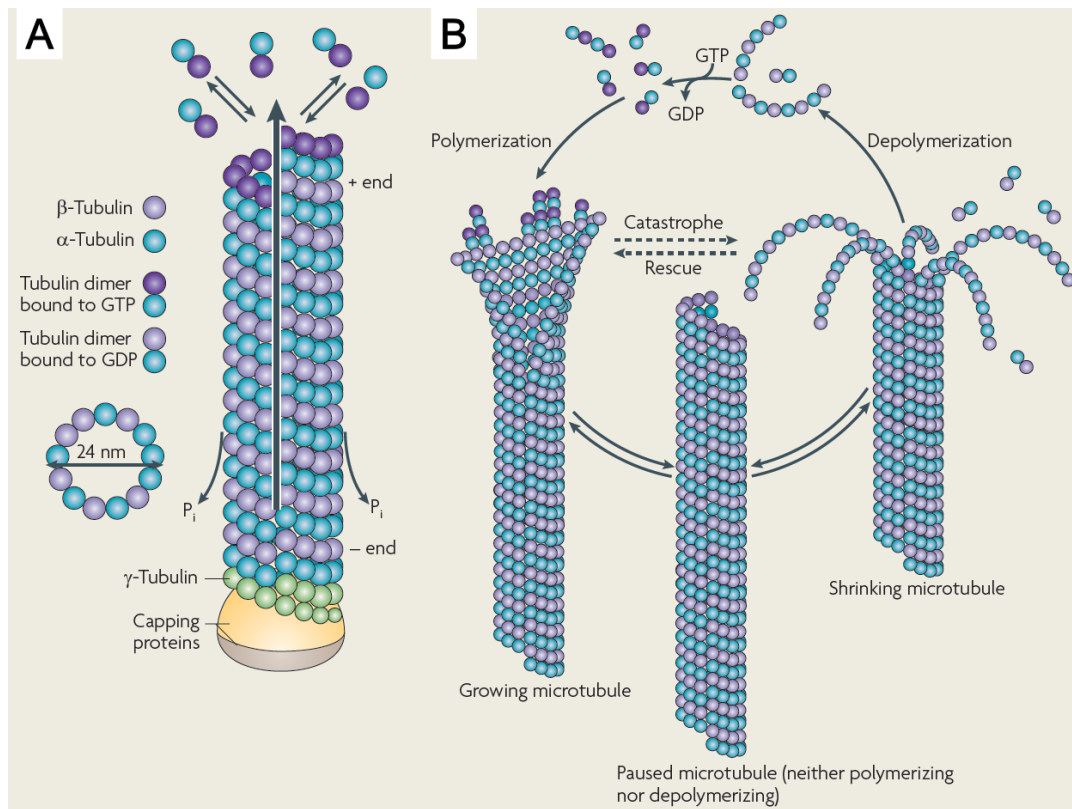


Figure 1.2 Scheme of MT structure and dynamics. (A) The polarized structure of MT with linear protofilaments laterally aligned to form a 24 nm wide hollow cylinder. (B) The MT polymerizing, paused and depolymerizing phases. (From Conde and Caceres, 2009)²⁶ This figure is adapted with permission.

Each tubulin can be divided into three sequential domains: N-terminal domain, intermediate domain and C-terminal domain. The N-terminal domain comprises the alternation of parallel beta strands (S1-S6) and helices (H1-H5). The intermediate domain comprises five helices (H6-H10) and mixed beta strands (S7-S10). The C-terminal domain comprises two anti-parallel helices (H11-H12) that cross over the other two domains.²⁷

The minus end of MT is anchored in MT organizing centers called centrosomes. MTs grow from centrosomes to the plasma membrane. MTs compose mitotic spindles, which interact with chromosomes and orchestrate the movement of chromosomes.²⁸

1.2.2 Dynamic behaviors

The length of MT is constantly changing, with heterodimers constantly adding and subtracting at both ends. The addition and subtraction at the minus end are much faster than that of the plus end, the unbalanced rate at two ends causes the dynamic change of MT length. The event with transition from growing or pausing state to shortening state is called catastrophe. On the contrary, the event with opposite transition is called rescue.²⁸

(Figure 1.2B)

The highly dynamic MT cytoskeletal fibers exhibit two types of non-equilibrium dynamic behaviors: treadmilling and dynamic instability.²⁹ Treadmilling refers to no net growth of MT because the loss of heterodimers at plus end is balanced by the addition of heterodimers at minus end. Tubulin subunits treadmill from plus end to minus end during the treadmilling process. Dynamic instability refers to the stochastic switch between the growing and the shrinking phase.²⁹ During polymerization of MTs, the addition of dimers at plus end is much faster than at minus end. During depolymerization of MTs, the loss of dimers at plus end is much faster than at minus end. Also, addition or loss of tubulin subunits at plus end is more extensive than that at minus end. Therefore, the dynamicity at plus end is much more active than that at minus end.²⁹

The dynamics of MT are essential for their functional roles. The dynamic mitotic spindles are also among the most important targets for anti-cancer drugs. The principle is that MT functions are determined by the dynamics of MT and the dynamics can be altered by MT-targeted agents. The mitotic spindles lead the movement of chromosomes during mitosis. In order to equally partition the replicated chromosomes and segregate them to two daughter cells, mitotic spindles must undergo random assembly and disassembly by continuous addition or loss of tubulin subunits.¹⁴ Any reagents binding to $\alpha\beta$ -tubulin heterodimers that block the polymerization or depolymerization of mitotic spindles would arrest the cell division.²⁹

1.3 Microtubule-targeted agents

Based on whether the MT-targeted agents promote or prevent polymerization, they can be classified into two categories: MT stabilizers and MT destabilizers. Some of the MT-targeted agents have been already developed into chemotherapeutics for cancer treatment, and are called antimetabolic drugs. Antimetabolic drugs suppress the dynamics of mitotic spindles, inhibit mitosis, and induce apoptosis. The binding sites of antimetabolic drugs are known as vinca, colchicine or taxane site.²⁹ Exceptions also exist. For instance, noscapine and estramustine are MT-targeted agents as well, but their binding sites belong to none of the three known sites above. These agents belong to a new category, whose binding site is called the novel site.³⁰

1.3.1 Microtubule stabilizers

The most well-known example of MT stabilizers is paclitaxel or taxol. MT-stabilizing agents include those targeting MT at the taxane site, such as docetaxel, discodermolide, ixabepilone, cyclostreptin, and eleutherobins. Other stabilizing agents bind MT at the novel site, such as laulimalide, peloruside A, epothilones, patupilone, sarcodictyins, dictyostatin, rhazinalam, certain steroids and polyisoprenyl benzophenones.³⁰ As the name of the category implies, MT stabilizers prevent MT from depolymerizing. MTs targeted by stabilizers keep growing, and the dynamic behaviors of treadmilling and dynamic instability are dramatically inhibited. The inhibition of MT dynamics, in turn, disrupts the functions of mitotic spindles involved in congression and segregation of chromosomes, causing the arrest of mitosis and further devastation of cell death resulting from apoptosis. The binding site of taxol is located at the interior surface of β -tubulin.³¹

The reason for stimulating polymerization is that the binding of stabilizers causes conformational changes of tubulin dimers to strengthen the contacts with neighboring subunits.²³ *In vitro* experiments showed that the chromosomes of human cells treated with taxol no longer congressed uniformly at the metaphase plate during mitosis, and some chromosomes were stuck at the pole. Due to the interference with chromosome alignment, cell division was blocked.³² **(Figure 1.3A-B)**

1.3.2 Microtubule destabilizers

The MT destabilizing agents include those targeting MT at the colchicine site and the vinca site, respectively, as well as other agents binding MT at the novel site, such as estramustine, noscapine, halichondrins and combretastatins.²⁹ The colchicine-site agents include colchicine, ombrabulin, 2-methoxyestradiol and indibulin. Among them, colchicine has not yet been used for cancer treatment due to its potent toxicity.³³ The vinca-site agents encompass cryptophycins and vinca alkaloids, including vinblastine, vincristine, vinorelbine, vindesine and vinflunine.²⁹ In contrast with the MT stabilizers, the MT destabilizers promote the depolymerization of MTs and cause perturbations on the dynamics of treadmilling as well as the random switch between growing and shortening states, which also defunctionalizes the mitotic spindles and terminates mitosis. The MT-destabilizing agents cause the conformational changes of functional segments to weaken the lateral and longitudinal contacts; thus, the structure of $\alpha\beta$ -tubulin heterodimer is destabilized and MTs tend to depolymerize.³⁴ Unlike the taxol site, the colchicine binding site is located at the exterior surface of β -tubulin.³⁵ The binding site of vinblastine is located at the interface of the $\alpha\beta$ -tubulin heterodimer comprising residues

from both α - and β -tubulin.³⁶ *In vitro* studies showed that the breast cancer MCF-7 cells proliferated smoothly and quickly without applying any treatment, however, the MT network was damaged and broken into short pieces after adding vinblastine.¹⁴ (**Figure 1.3C-D**)

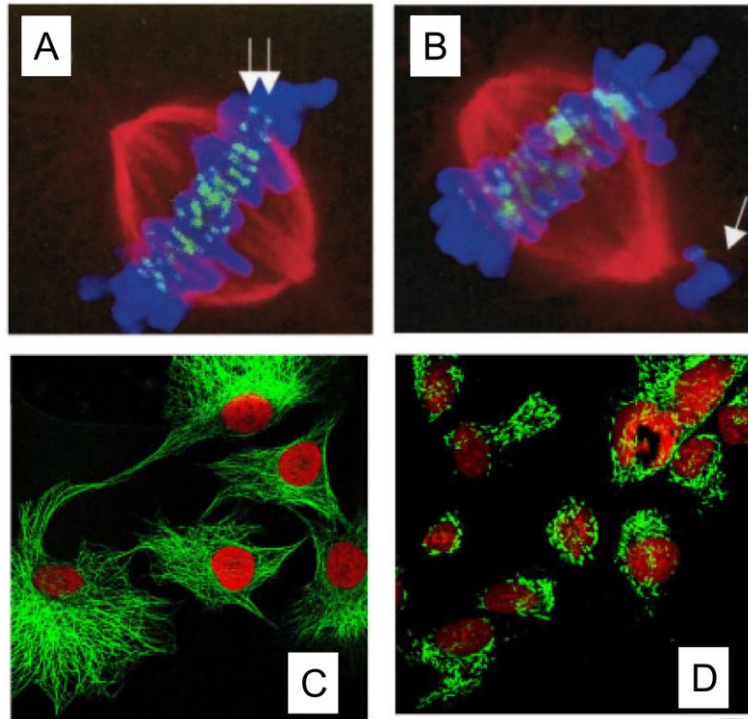


Figure 1.3 Confocal microscopy images of cancer cells revealing the drug effects. Human osteosarcoma cells at early metaphase in (A) the absence of taxol and (B) the presence of 10 nM taxol. MTs are in red, chromosomes are in blue and kinetochores are in green. (From Kelling *et al.*, 2003)³² Breast cancer MCF-7 cells (C) without any treatment and (D) with vinblastine. MTs are in green and nuclei are in red. (From Stanton *et al.*, 2011)¹⁴ These figures are adapted with permission.

1.4 Carbon nanotubes

Carbon nanotubes (CNTs) are hollow tubes with diameters in the range of a few nanometers and lengths up to hundreds of micrometers. The wall of the tube is made of a hexagonal lattice of carbon atoms, similar to the planar graphene layers in graphite. CNTs were first discovered by Iijima in the early 1990s.³⁷⁻³⁸ With extensive studies, CNTs have been applied across disciplines in composite materials, microelectronics, energy storage, biosensor and cancer treatment, due to their unique electronic, optical and chemical properties.³⁹

1.4.1 Structure

The carbon atoms in CNT are in sp^2 hybridization, they are similar to the carbons in graphite. The bonds formed by carbon atoms with sp^2 hybridization are stronger than those formed with sp^3 hybridization, contributing to the considerable strength of CNTs. CNTs are classified into two main groups: single-walled CNTs (SWNTs) and multi-walled CNTs (MWNTs). The formation of SWNTs can be visualized as one graphene sheet wrapped into a seamless cylindrical tube and, similarly, the formation of MWNTs can be pictured as multiple graphene sheets wrapped into seamless coaxial cylinders. According to the method of rolling graphite layers into a tubular structure, CNTs are distinguished by chirality as armchair, zigzag and chiral. With a pair of unit vectors (\mathbf{a}_1 , \mathbf{a}_2), the wrapping vector \mathbf{C} is defined as $\mathbf{C} = n\mathbf{a}_1 + m\mathbf{a}_2$, where n and m are two integers. The integer pair (n, m) can describe the chirality of CNTs. If $n = m$, this corresponds to the armchair type. If $m = 0$, this corresponds to the zigzag type. When non-zero n and m are not equal, this corresponds to the chiral type of CNTs.⁴⁰ (**Figure 1.4**)

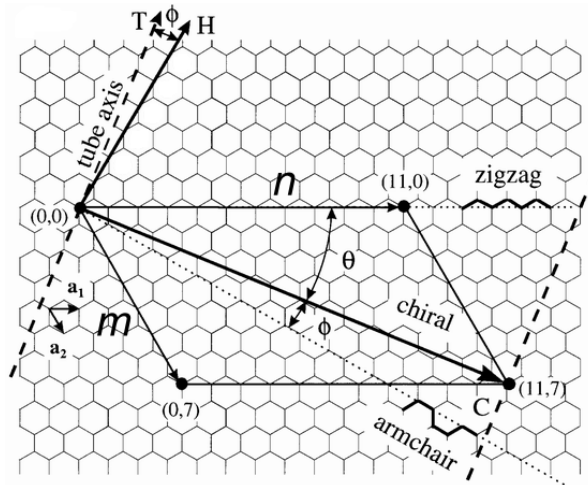


Figure 1.4 Schematic depiction of CNT formation by wrapping a graphene sheet. The tube axis **T** is shown by the dashed line. $(\mathbf{a}_1, \mathbf{a}_2)$ is a pair of unit vectors and n and m are two integers to describe the chirality. The wrapping vector **C** is defined as $\mathbf{C} = n\mathbf{a}_1 + m\mathbf{a}_2$. The solid vector **H** is perpendicular to the longitudinal axis along the armchair direction. The chiral angle ϕ is the angle between **T** and **H**. The chiral tube has a wrapping angle θ relative to the longitudinal axis along the zigzag direction. (From Wilder *et al.*, 1998)⁴¹ This figure is adapted with permission.

The ideally identical hexagonal lattice structure of CNTs does not exist in reality. Defects are inevitable during the synthesis process. Approximately, up to 1-3% of carbon atoms are oxidized and acidified during the process of synthesis by laser vaporization or electric arc discharge techniques and the subsequent purification.⁴² The defect sites are more chemically active than the regular structure and can lead to further functionalizations. Some properties of CNTs, such as solubility and dispersity, can be improved through chemical functionalization of pristine CNT structures. Two strategies

are implemented to functionalize the CNT structure: covalent modification of the CNT sidewall or ends, and non-covalent wrapping lipids or polymers on the CNT surface.⁴³ Oxygen containing groups, such as carboxyl and hydroxyl groups, are formed at some defect sites by oxidation reactions in the concentrated acidic environment of mixed nitric acid and sulfuric acid under ultrasonic treatment.⁴⁴ The carboxyl groups introduced by acidic oxidation can proceed with further reactions, such as esterification or amidization, which in turn provide covalent linkages to a wide range of functional moieties.⁴⁴ The covalent modification transforms the bonding structure from sp^2 to sp^3 at active sites resulting in the partial loss of π -conjugation. Conversely, the non-covalent functionalization maximally preserves the original properties of CNTs, and can remarkably improve solubility with the aid of hydrophilic groups. For instance, aromatic compounds interact with CNT sidewalls by π - π stacking interactions; conjugated polymers with aromatic rings can wrap CNT sidewalls through π - π stacking and van der Waals interactions.⁴³

1.4.2 Applications

The applications of CNTs range from electronics, energy conversion and storage to enhanced composite fibers, biosensors and biomedical devices. For example, the large surface area of CNTs provides sufficient electrode-electrolyte contact, expedites the charge-discharge rates, and decreases resistance for ion transport; therefore, CNTs are used as anode materials for preparing light and portable lithium-ion batteries with high energy density.⁴⁵ The low density and promising mechanical properties, such as high Young's modulus and tensile strength of CNTs⁴⁶, facilitate the usage of CNTs as fillers to

manufacture enhanced load-bearing composite fibers.⁴⁷ The large effective working area of SWNT modified glassy carbon electrodes dramatically increases the peak current of cyclic voltammogram, after coating annealed SWNT film on glassy carbon electrode surface. The nanostructured topology of annealed SWNT surface advances direct electron transfer to the adsorbed enzyme and therefore, significantly increases the electroactivity. CNT modified electrodes promote electron transfer and provide a new paradigm on the design of highly sensitive nanobiosensors to detect biological redox molecules.⁴⁸

The functionalization of CNTs by non-covalent coating of amphiphilic molecules, or covalently grafting polar functional groups onto the sidewalls creates soluble and debundled CNTs in an aqueous environment. Therefore, functionalized CNTs are widely used in biomedical areas such as transportation vehicles for therapy or diagnosis.⁴⁹ SWNTs, ~400-500 nm in length and 1.2-1.5 nm in diameter, were functionalized with poly(ethylene glycol), biotin, tyrosine and alkyl chain, showing an amphiphilic character, to deliver doxorubicin (DOX) to cervical cancer derived HeLa cells and non-cancerous Chinese Hamster Ovarian (CHO) cells. At the same drug concentration, SWNT-DOX achieved a much higher efficacy to kill the two types of cells than free DOX because of the enhanced internalization of the drug-SWNT system. HeLa cells expressed much more biotin receptors than CHO cells, the receptor-mediated specific transportation of DOX loaded on biotinylated SWNTs caused more death to HeLa cells than CHO cells.⁵⁰

CNT-based immunosensors have been developed for early cancer diagnosis through clinical detection and measurement of cancer biomarkers. The assembled immunosensors consisting of SWNT forest platforms attached by enzyme-antibody-nanotube

bioconjugates showed enhanced sensitivity and selectivity for the detection of prostate specific antigen in calf and human serum samples. Due to high conductivity and surface area of SWNT platform along with the catalytic nature of enzyme labels, a low detection limit of 4 pg/mL on the prostate carcinoma biomarker by CNT immunosensors was achieved, surpassing the detection limit of commercial immunoassay methods.⁵¹ More biomedical functions of CNTs are emerging, as the electrical, optical and thermal properties of CNTs enable the possibility to detect, monitor and cure diseases.⁵²

1.5 Computer modeling

Computer modeling refers to the computational studies of any system of interest by utilizing molecular modeling techniques with the purpose of understanding the structure-function correlation at the atomic or molecular levels, and predicting the macroscopic properties of a system. Quantum mechanics and molecular mechanics are the modeling techniques used to study systems ranging from small molecular scale to large biomacromolecular scale.

1.5.1 Molecular Docking

Molecular docking is a computational technique used to study the molecular recognition involved in protein–protein, ligand–protein (small molecule and protein) as well as ligand and nucleic acid (small molecule and DNA/RNA) interactions. The origin of such interactions is the collective effect of hydrophobic interactions, van der Waals forces, hydrogen bonding, and electrostatic forces. The docking problem can be divided into two parts: searching and scoring. Searching and scoring are coupled in the docking process:

scored decisions are made during the progression of searching. Four widely used docking programs are *DOCK*⁵³⁻⁵⁴, *FlexX*⁵⁵, *GOLD*⁵⁶ and *ICM*⁵⁷. Although each software has its unique searching and scoring algorithms, they share a mutual algorithmic foundation since they are aimed to search for a matchable conformation by taking into account all of the possible inter-atomic forces. A decision needs to be made whether to accept or reject the detected binding geometry according to criteria set in the scoring function. If accepted, a pose is generated; if rejected, a new search will start. The coupled searching and scoring step continues to generate all acceptable poses, and all candidate poses are ranked based on the scoring function correlated to the binding affinity. Three types of docking have been developed in the past: rigid body docking, with both the ligand and the receptor rigid; flexible ligand docking, with the ligand flexible but the receptor rigid; flexible docking, with both the ligand and the receptor flexible. Due to the limits on computational efficiency, flexible ligand docking is the most commonly used method to pinpoint the binding sites of small molecules interacting with macromolecules.⁵⁸ The drawback of the rigid receptor in flexible ligand docking is addressed with more advanced methods to include the flexibility of both ligand and receptor, which will be discussed later.

Several factors can affect the accuracy of the predicted binding site and the reliability of the scores for ranking docking solutions. One factor is the ligand structure, including protonation and tautomeric states. Another factor is the receptor structure in terms of the resolution of crystal structures, or the choice of template used for homology modeled structures. Apart from the candidate structure of ligand and receptor, receptor flexibility

is another key factor in determining the docking output. Despite the frequently used pattern of flexible ligand and rigid receptor, receptors are not actually rigid upon ligand binding. They most likely undergo conformational changes, such as major side chain flexibility and minor backbone displacement.⁵⁹ The ligand induced conformational changes, also known as induced fit, make the contact with ligand or solvent in more energetically favorable conformations.⁶⁰⁻⁶¹ Therefore, the rigid receptor hypothesis could lead to inaccurate binding modes and poor docking scores. In order to address challenges encountered in the rigid receptor setting, the concept of “soft docking” has been introduced to the docking algorithms. Soft docking considers geometric and energetic complementarity by allowing small conformational changes⁶² as well as the idea of side-chain flexibility by extending the search for more rotameric states of amino acid side chains.⁶³

The scoring function also plays a dominant role in the fidelity of docking solutions. The scoring functions are classified into three categories: knowledge-based, empirical and force-field based scoring function.^{58, 64} Based on the statistical analysis of experimentally determined protein-ligand complexes, knowledge-based scoring functions are developed by elucidating the rules for stable and unstable atom pair interactions from the experimental data.⁶⁵ The empirical scoring function adds up the enthalpic and entropic interactions with contributing terms of different weight, including van der Waals, electrostatic interactions and hydrogen bonding, determined by the regression of experimentally measured binding affinities from the training set of protein-ligand complexes. The *FlexX* scoring function belongs to this type.^{55, 66} The third type of scoring

function, based on the force field, is similar to the empirical type by adding up individual terms of different types of interactions for the prediction of binding affinity; however, the difference lies in the source of the terms: the interaction terms in the force-field based scoring function are extracted from the physical and chemical phenomena rather than from the experimentally determined binding free energies as in the scenario of the empirical scoring function. The scoring function utilized in *DOCK* belongs to the force-field based category.⁶⁷

Ligand–protein docking is widely used in rational drug design, for instance, the docking of small molecules with therapeutic function to protein or nucleic acid targets. Protein–protein docking, on the other hand, advances studies on molecular recognition, inhibitor design, cellular pathways, as well as macromolecular interactions and assemblies.⁶⁸

1.5.2 Molecular dynamics simulations

Molecular dynamics (MD) simulations are computer simulations of the physical motion of particles in a system. The system under study ranges from a single particle to a huge system with massive particles, such as a protein macromolecule with hundreds of amino acids and tens of thousands of atoms. The movements of particles are determined by the Newtonian equations of motion. Solving the interaction potential equations for all of the particles in a system is a core part of MD simulations.

For particle i in a system with N particles, F_i is the force applied on the particle, r_i is the coordinate for the particle at the given time t , m_i is the mass of particle i , and V is the potential function of the system.⁶⁹

The interacting forces are the negative derivatives of potential functions;

$$F_i = -\frac{\partial V}{\partial r_i} \quad \text{(Equation 1.1)}$$

Force is also determined by Newton's second law;

$$F_i = m_i \frac{\partial^2 r_i}{\partial t^2} \quad \text{(Equation 1.2)}$$

The equations for calculating the potential energies and forces along with the parameters set for the equations compose a force field. Common force fields used in MD simulations include CHARMM⁷⁰⁻⁷¹, AMBER⁷²⁻⁷³, GROMOS⁷⁴⁻⁷⁵ and OPLS⁷⁶. The equations applied in a force field are classified into two categories: equations for calculating bonded interactions and equations for non-bonded interactions. Bond stretching, angle bending and torsions are bonded interactions; van der Waals (vdW) forces and Coulomb forces are non-bonded interactions.

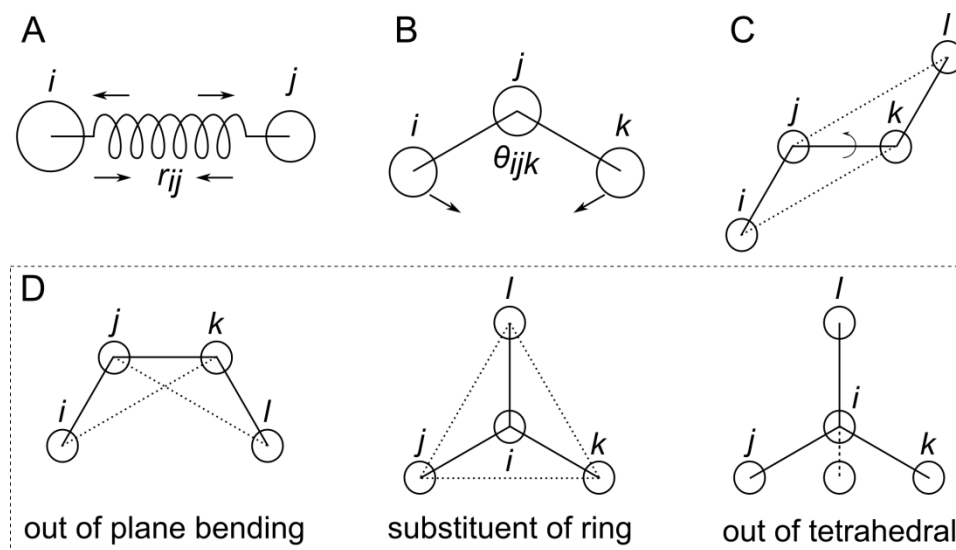


Figure 1.5 Scheme of bonded interactions. (A) Bond stretching between atom i and j , (B) angle bending among atoms i, j and k , and dihedral angles among atoms i, j, k and l in the form of (C) proper dihedral as well as (D) improper dihedral.

The potential energy for bond stretching, V_b , is calculated by Hooke's law (harmonic potential):

$$V_b(r_{ij}) = \frac{1}{2} k_{ij}^b (r_{ij} - b_{ij})^2 \quad \text{(Equation 1.3)}$$

where k_{ij}^b is the bond stretching constant, r_{ij} is the interatomic distance, and b_{ij} is the reference bond length.⁶⁹ (**Figure 1.5 A**)

The potential energy V_a for the vibration among a triplet of atoms i, j and k with the angle θ_{ijk} is also represented by a harmonic potential:

$$V_a(\theta_{ijk}) = \frac{1}{2} k_{ijk}^\theta (\theta_{ijk} - \theta_{ijk}^0)^2 \quad \text{(Equation 1.4)}$$

where k_{ijk}^θ is the angle bending force constant and θ_{ijk}^0 is the reference bond angle.⁶⁹

(Figure 1.5 B)

The 4-body dihedral angles include proper dihedrals for non-planar groups and improper dihedrals for planar groups. The proper dihedral V_d for a quartet of atoms i, j, k and l with the dihedral angle φ between the (i, j, k) and (j, k, l) planes is given by,

$$V_d(\varphi_{ijkl}) = k_\varphi(1 + \cos(n\varphi - \varphi_s)) \quad \text{(Equation 1.5)}$$

where k_φ is the rotation barrier, n is multiplicity, and φ_s is the phase factor.⁶⁹ **(Figure 1.5 C)**

The improper dihedral, V_{id} , for a planar structure with the angle ξ_{ijkl} between the (i, j, k) and (j, k, l) planes is calculated by a harmonic potential:

$$V_{id}(\xi_{ijkl}) = \frac{1}{2} k_\xi (\xi_{ijkl} - \xi_0)^2 \quad \text{(Equation 1.6)}$$

where k_ξ is the bending force constant and ξ_0 is the reference bending angle.⁶⁹ **(Figure 1.5 D)**

The vdW interactions are the combined effects of long-range attractive forces and short-range repulsive forces. vdW interactions, V_{LJ} , between atoms i and j separated by the interatomic distance r_{ij} are modeled by the Lennard-Jones (LJ) potential:

$$V_{LJ}(r_{ij}) = \frac{C_{ij}^{(12)}}{r_{ij}^{12}} - \frac{C_{ij}^{(6)}}{r_{ij}^6} \quad \text{(Equation 1.7)}$$

where $C_{ij}^{(12)}$ and $C_{ij}^{(6)}$ are LJ parameters depending on the pair of atom types. r_{ij}^{-12} and r_{ij}^{-6} indicate the terms for repulsive and attractive forces, respectively.⁶⁹

The Coulomb interactions, V_c , between atoms i and j with partial atomic charges q_i and q_j are computed by the electrostatic potential:

$$V_c(r_{ij}) = \frac{1}{4\pi\epsilon_0} \frac{q_i q_j}{\epsilon_r r_{ij}} \quad (\text{Equation 1.8})$$

where ϵ_0 is the vacuum permittivity and ϵ_r is the relative dielectric constant.⁶⁹

Taking into account the bonded and non-bonded interactions, the potential function $V(r^N)$ for a N -particle system is defined as below⁶⁹:

$$\begin{aligned} V(r^N) = & \sum_{\text{bonds}} \frac{1}{2} k_{ij}^b (r_{ij} - b_{ij})^2 \\ & + \sum_{\text{angles}} \frac{1}{2} k_{ijk}^\theta (\theta_{ijk} - \theta_{ijk}^0)^2 \\ & + \sum_{\text{torsions}} \left\{ k_\varphi (1 + \cos(n\varphi - \varphi_s)) + \frac{1}{2} k_\xi (\xi_{ijkl} - \xi_0)^2 \right\} \\ & + \sum_{i=1}^N \sum_{j=i+1}^N \left[\left(\frac{C_{ij}^{(12)}}{r_{ij}^{12}} - \frac{C_{ij}^{(6)}}{r_{ij}^6} \right) + \frac{1}{4\pi\epsilon_0} \frac{q_i q_j}{\epsilon_r r_{ij}} \right] \end{aligned} \quad (\text{Equation 1.9})$$

An initial set of coordinates for each particle in a system is required in order to start an MD simulation. The coordinates generate a three dimensional (3D) structure for the system under study. In the case of proteins, the 3D structure is obtained experimentally by X-ray crystallography or nuclear magnetic resonance (NMR), or theoretically by homology modeling provided with a known homologous structure. The initial structure is refined by energy minimization for the stress relief caused by bond length distortions or overlapped non-bonded atoms. Initial velocities are randomly assigned to each particle in

the system. The duration of an MD simulation varies from picoseconds to nanoseconds, depending on the size (complexity) of the system. In general, the more particles a system contains, the longer a simulation will run. After the system reaches equilibrium, the simulation can stop. At the post-equilibrium stage, the system shows stabilized thermodynamic properties, such as temperature, pressure and energy.⁷⁷

MD simulations can provide continual visualized information on the motion of the system; for instance, the folding change of a protein molecule can be thoroughly tracked from the MD trajectory. The structural changes sometimes relate to particular functional roles, such as the “breathing” conformational changes to open the channel for oxygen and carbon monoxide interacting with the buried haem group in haemoglobin.⁷⁷ MD simulations also assist protein crystallography to refine the experimentally determined structure. Another important application for MD simulations is to calculate the free-energy difference between similar systems, which can further elucidate the binding affinity of a ligand.⁷⁷

1.6 Summary

Targeting the mitotic spindles of microtubules in the midst of cancer cell division has been an effective way to conquer the infinite proliferation of tumor cells and will continue to be a powerful strategy in the cancer battle. Well-developed computing algorithms have advanced computer modeling, making significant contributions to the study of interactions between drugs and targets on the atomic scale. The improvement of commercially available therapeutics and the discovery of new compounds with enhanced

potency, but reduced side effects rely on the combined techniques of computational modeling, experimental tests and clinical trials. One of the solutions to seek “smart” cancer treatment with high specificity and selectivity relies on the innovations of drug delivery systems, considering the advantages of customizable carbon nanotubes as carriers for drugs and recognizing moieties. Beyond the resolution of experimentally determined three dimensional structures of macromolecules, molecular dynamics simulations based on currently available experimental data are able to dig accurate conformational details in depth assisting the design of drugs and drug delivery systems.⁷⁸

My thesis elaborates on two aspects relevant to cancer research in the following two chapters: first, the effects of one of the commonly used anti-cancer drugs on the tubulin dimer structure in contrast with the comparable influence of the low temperature; second, the non-covalent interactions between the drug and carbon nanotube based carriers under different conditions. Following the two main chapters of the work performed during the master’s degree program, the concluding chapter summarizes the entire work and provides future perspectives.

1.7 Bibliography

1. Croce, C. M. Oncogenes and Cancer. *New England Journal of Medicine* **2008**, *358*, 502-511.
2. Hanahan, D.; Weinberg, R. A. The Hallmarks of Cancer. *Cell* **2000**, *100*, 57-70.

3. Anand, P.; Kunnumakara, A.; Sundaram, C.; Harikumar, K.; Tharakan, S.; Lai, O.; Sung, B.; Aggarwal, B. Cancer Is a Preventable Disease That Requires Major Lifestyle Changes. *Pharmaceutical Research* **2008**, *25*, 2097-2116.
4. Karp, G. *Cell and Molecular Biology: Concepts and Experiments*, 7th ed.; John Wiley & Sons, Inc., 2013, pp 664-698.
5. Corrie, P. G. Cytotoxic Chemotherapy: Clinical Aspects. *Medicine* **2008**, *36*, 24-28.
6. Bucci, M. K.; Bevan, A.; Roach, M. Advances in Radiation Therapy: Conventional to 3d, to Imrt, to 4d, and Beyond. *CA: A Cancer Journal for Clinicians* **2005**, *55*, 117-134.
7. Lind, M. J. Principles of Cytotoxic Chemotherapy. *Medicine* **2008**, *36*, 19-23.
8. Pawlik, T. M.; Keyomarsi, K. Role of Cell Cycle in Mediating Sensitivity to Radiotherapy. *International Journal of Radiation Oncology Biology Physics* **2004**, *59*, 928-942.
9. Makin, G.; Hickman, J. A. Apoptosis and Cancer Chemotherapy. *Cell and Tissue Research* **2000**, *301*, 143-152.
10. Shirode, A. B.; Kovvuru, P.; Chittur, S. V.; Henning, S. M.; Heber, D.; Reliene, R. Antiproliferative Effects of Pomegranate Extract in Mcf-7 Breast Cancer Cells Are Associated with Reduced DNA Repair Gene Expression and Induction of Double Strand Breaks. *Molecular Carcinogenesis* **2014**, *53*, 458-470.
11. Portsmouth, D.; Hlavaty, J.; Renner, M. Suicide Genes for Cancer Therapy. *Molecular Aspects of Medicine* **2007**, *28*, 4-41.
12. Sporn, M. B. The War on Cancer. *The Lancet* **1996**, *347*, 1377-1381.

13. Alberts, B.; Bray, D.; Hopkin, K.; Johnson, A. D.; Lewis, J.; Raff, M.; Roberts, K.; Walter, P. *Essential Cell Biology*, 4th ed.; Garland Publishing, Inc., 2014, pp 603-633.
14. Stanton, R. A.; Gernert, K. M.; Nettles, J. H.; Aneja, R. Drugs That Target Dynamic Microtubules: A New Molecular Perspective. *Medicinal Research Reviews* **2011**, *31*, 443-481.
15. Weaver, B. A. A.; Cleveland, D. W. Decoding the Links between Mitosis, Cancer, and Chemotherapy: The Mitotic Checkpoint, Adaptation, and Cell Death. *Cancer Cell* **2005**, *8*, 7-12.
16. Hengartner, M. O. The Biochemistry of Apoptosis. *Nature* **2000**, *407*, 770-776.
17. Elmore, S. Apoptosis: A Review of Programmed Cell Death. *Toxicologic Pathology* **2007**, *35*, 495-516.
18. Kerr, J. F. R.; Winterford, C. M.; Harmon, B. V. Apoptosis. Its Significance in Cancer and Cancer Therapy. *Cancer* **1994**, *73*, 2013-2026.
19. Evan, G. I.; Vousden, K. H. Proliferation, Cell Cycle and Apoptosis in Cancer. *Nature* **2001**, *411*, 342-348.
20. Fletcher, D. A.; Mullins, R. D. Cell Mechanics and the Cytoskeleton. *Nature* **2010**, *463*, 485-492.
21. Alberts, B.; Bray, D.; Hopkin, K.; Johnson, A. D.; Lewis, J.; Raff, M.; Roberts, K.; Walter, P. *Essential Cell Biology*, 4th ed.; Garland Publishing, Inc., 2014, pp 567-592.

22. Wade, R. On and around Microtubules: An Overview. *Molecular Biotechnology* **2009**, *43*, 177-191.
23. Nogales, E. Structural Insights into Microtubule Function. *Annual Review of Biochemistry* **2000**, *69*, 277-302.
24. Erickson, H. P. Gamma-Tubulin Nucleation: Template or Protofilament? *Nature Cell Biology* **2000**, *2*, E93-E96.
25. Wiese, C.; Zheng, Y. A New Function for the Gamma-Tubulin Ring Complex as a Microtubule Minus-End Cap. *Nature Cell Biology* **2000**, *2*, 358-364.
26. Conde, C.; Caceres, A. Microtubule Assembly, Organization and Dynamics in Axons and Dendrites. *Nature Reviews Neuroscience* **2009**, *10*, 319-332.
27. Nogales, E.; Wolf, S. G.; Downing, K. H. Structure of the Alpha Beta Tubulin Dimer by Electron Crystallography. *Nature* **1998**, *391*, 199-203.
28. Honore, S.; Pasquier, E.; Braguer, D. Understanding Microtubule Dynamics for Improved Cancer Therapy. *Cellular and Molecular Life Sciences CMLS* **2005**, *62*, 3039-3056.
29. Jordan, M. A.; Wilson, L. Microtubules as a Target for Anticancer Drugs. *Nature Reviews Cancer* **2004**, *4*, 253-265.
30. Dumontet, C.; Jordan, M. A. Microtubule-Binding Agents: A Dynamic Field of Cancer Therapeutics. *Nat Rev Drug Discov* **2010**, *9*, 790-803.
31. Nogales, E.; Grayer, Wolf, S.; Khan, I. A.; Luduena, R. F.; Downing, K. H. Structure of Tubulin at 6.5 Å and Location of the Taxol-Binding Site. *Nature* **1995**, *375*, 424-427.

32. Kelling, J.; Sullivan, K.; Wilson, L.; Jordan, M. A. Suppression of Centromere Dynamics by Taxol® in Living Osteosarcoma Cells. *Cancer Research* **2003**, *63*, 2794-2801.
33. Jordan, M. A. Mechanism of Action of Antitumor Drugs That Interact with Microtubules and Tubulin. *Current Medicinal Chemistry -Anti-Cancer Agents* **2002**, *2*, 1-17.
34. Keskin, O.; Durell, S. R.; Bahar, I.; Jernigan, R. L.; Covell, D. G. Relating Molecular Flexibility to Function: A Case Study of Tubulin. *Biophysical Journal* **2002**, *83*, 663-680.
35. Ravelli, R. B. G.; Gigant, B.; Curmi, P. A.; Jourdain, I.; Lachkar, S.; Sobel, A.; Knossow, M. Insight into Tubulin Regulation from a Complex with Colchicine and a Stathmin-Like Domain. *Nature* **2004**, *428*, 198-202.
36. Gigant, B.; Wang, C.; Ravelli, R. B. G.; Roussi, F.; Steinmetz, M. O.; Curmi, P. A.; Sobel, A.; Knossow, M. Structural Basis for the Regulation of Tubulin by Vinblastine. *Nature* **2005**, *435*, 519-522.
37. Iijima, S. Helical Microtubules of Graphitic Carbon. *Nature* **1991**, *354*, 56-58.
38. Iijima, S.; Ichihashi, T. Single-Shell Carbon Nanotubes of 1-Nm Diameter. *Nature* **1993**, *363*, 603-605.
39. De Volder, M. F. L.; Tawfick, S. H.; Baughman, R. H.; Hart, A. J. Carbon Nanotubes: Present and Future Commercial Applications. *Science* **2013**, *339*, 535-539.

40. Baughman, R. H.; Zakhidov, A. A.; de Heer, W. A. Carbon Nanotubes--the Route toward Applications. *Science* **2002**, *297*, 787-792.
41. Wilder, J. W. G.; Venema, L. C.; Rinzler, A. G.; Smalley, R. E.; Dekker, C. Electronic Structure of Atomically Resolved Carbon Nanotubes. *Nature* **1998**, *391*, 59-62.
42. Hu, H.; Bhowmik, P.; Zhao, B.; Hamon, M. A.; Itkis, M. E.; Haddon, R. C. Determination of the Acidic Sites of Purified Single-Walled Carbon Nanotubes by Acid-Base Titration. *Chemical Physics Letters* **2001**, *345*, 25-28.
43. Zhao, Y.-L.; Stoddart, J. F. Noncovalent Functionalization of Single-Walled Carbon Nanotubes. *Accounts of Chemical Research* **2009**, *42*, 1161-1171.
44. Balasubramanian, K.; Burghard, M. Chemically Functionalized Carbon Nanotubes. *Small* **2005**, *1*, 180-192.
45. Candelaria, S. L.; Shao, Y.; Zhou, W.; Li, X.; Xiao, J.; Zhang, J.-G.; Wang, Y.; Liu, J.; Li, J.; Cao, G. Nanostructured Carbon for Energy Storage and Conversion. *Nano Energy* **2012**, *1*, 195-220.
46. Yu, M.-F.; Lourie, O.; Dyer, M. J.; Moloni, K.; Kelly, T. F.; Ruoff, R. S. Strength and Breaking Mechanism of Multiwalled Carbon Nanotubes under Tensile Load. *Science* **2000**, *287*, 637-640.
47. Coleman, J. N.; Khan, U.; Blau, W. J.; Gun'ko, Y. K. Small but Strong: A Review of the Mechanical Properties of Carbon Nanotube-Polymer Composites. *Carbon* **2006**, *44*, 1624-1652.

48. Anthony, G.-E.; Chenghong, L.; Ray, H. B. Direct Electron Transfer of Glucose Oxidase on Carbon Nanotubes. *Nanotechnology* **2002**, *13*, 559.
49. Heister, E.; Brunner, E. W.; Dieckmann, G. R.; Jurewicz, I.; Dalton, A. B. Are Carbon Nanotubes a Natural Solution? Applications in Biology and Medicine. *ACS Applied Materials & Interfaces* **2013**, *5*, 1870-1891.
50. Brahmachari, S.; Ghosh, M.; Dutta, S.; Das, P. K. Biotinylated Amphiphile-Single Walled Carbon Nanotube Conjugate for Target-Specific Delivery to Cancer Cells. *Journal of Materials Chemistry B* **2014**, *2*, 1160-1173.
51. Yu, X.; Munge, B.; Patel, V.; Jensen, G.; Bhirde, A.; Gong, J. D.; Kim, S. N.; Gillespie, J.; Gutkind, J. S.; Papadimitrakopoulos, F., et al. Carbon Nanotube Amplification Strategies for Highly Sensitive Immunodetection of Cancer Biomarkers. *Journal of the American Chemical Society* **2006**, *128*, 11199-11205.
52. Kostarelos, K.; Bianco, A.; Prato, M. Promises, Facts and Challenges for Carbon Nanotubes in Imaging and Therapeutics. *Nature Nanotechnology* **2009**, *4*, 627-633.
53. Kuntz, I. D.; Blaney, J. M.; Oatley, S. J.; Langridge, R.; Ferrin, T. E. A Geometric Approach to Macromolecule-Ligand Interactions. *Journal of Molecular Biology* **1982**, *161*, 269-288.
54. DesJarlais, R. L.; Sheridan, R. P.; Seibel, G. L.; Dixon, J. S.; Kuntz, I. D.; Venkataraghavan, R. Using Shape Complementarity as an Initial Screen in Designing Ligands for a Receptor Binding Site of Known Three-Dimensional Structure. *Journal of Medicinal Chemistry* **1988**, *31*, 722-729.

55. Rarey, M.; Kramer, B.; Lengauer, T.; Klebe, G. A Fast Flexible Docking Method Using an Incremental Construction Algorithm. *Journal of Molecular Biology* **1996**, *261*, 470-489.
56. Jones, G.; Willett, P.; Glen, R. C.; Leach, A. R.; Taylor, R. Development and Validation of a Genetic Algorithm for Flexible Docking. *Journal of Molecular Biology* **1997**, *267*, 727-748.
57. Abagyan, R.; Totrov, M.; Kuznetsov, D. Icm—a New Method for Protein Modeling and Design: Applications to Docking and Structure Prediction from the Distorted Native Conformation. *Journal of Computational Chemistry* **1994**, *15*, 488-506.
58. Mohan, V.; Gibbs, A. C.; Cummings, M. D.; Jaeger, E. P.; DesJarlais, R. L. Docking: Successes and Challenges. *Current Pharmaceutical Design* **2005**, *11*, 323-333.
59. Najmanovich, R.; Kuttner, J.; Sobolev, V.; Edelman, M. Side-Chain Flexibility in Proteins Upon Ligand Binding. *Proteins: Structure, Function, and Bioinformatics* **2000**, *39*, 261-268.
60. Koshland, D. E. The Key–Lock Theory and the Induced Fit Theory. *Angewandte Chemie International Edition in English* **1995**, *33*, 2375-2378.
61. Leulliot, N.; Varani, G. Current Topics in Rna–Protein Recognition: Control of Specificity and Biological Function through Induced Fit and Conformational Capture. *Biochemistry* **2001**, *40*, 7947-7956.
62. Jiang, F.; Kim, S.-H. “Soft Docking”: Matching of Molecular Surface Cubes. *Journal of Molecular Biology* **1991**, *219*, 79-102.

63. Leach, A. R. Ligand Docking to Proteins with Discrete Side-Chain Flexibility. *Journal of Molecular Biology* **1994**, *235*, 345-356.
64. Liu, J.; Wang, R. Classification of Current Scoring Functions. *Journal of Chemical Information and Modeling* **2015**, *55*, 475-482.
65. Muegge, I.; Martin, Y. C. A General and Fast Scoring Function for Protein–Ligand Interactions: A Simplified Potential Approach. *Journal of Medicinal Chemistry* **1999**, *42*, 791-804.
66. Böhm, H.-J. The Development of a Simple Empirical Scoring Function to Estimate the Binding Constant for a Protein-Ligand Complex of Known Three-Dimensional Structure. *Journal of Computer-Aided Molecular Design* **1994**, *8*, 243-256.
67. Meng, E. C.; Shoichet, B. K.; Kuntz, I. D. Automated Docking with Grid-Based Energy Evaluation. *Journal of Computational Chemistry* **1992**, *13*, 505-524.
68. Halperin, I.; Ma, B.; Wolfson, H.; Nussinov, R. Principles of Docking: An Overview of Search Algorithms and a Guide to Scoring Functions. *Proteins: Structure, Function, and Genetics* **2002**, *47*, 409-443.
69. Leach, A. R. *Molecular Modelling: Principles and Applications*, 2nd ed.; Prentice Hall, 2001, pp 165-212.
70. Brooks, B. R.; Bruccoleri, R. E.; Olafson, B. D.; States, D. J.; Swaminathan, S.; Karplus, M. Charmm: A Program for Macromolecular Energy, Minimization, and Dynamics Calculations. *Journal of Computational Chemistry* **1983**, *4*, 187-217.
71. MacKerell, A. D.; Bashford, D.; Bellott, M.; Dunbrack, R. L.; Evanseck, J. D.; Field, M. J.; Fischer, S.; Gao, J.; Guo, H.; Ha, S., et al. All-Atom Empirical

- Potential for Molecular Modeling and Dynamics Studies of Proteins. *The Journal of Physical Chemistry B* **1998**, *102*, 3586-3616.
72. Weiner, S. J.; Kollman, P. A.; Case, D. A.; Singh, U. C.; Ghio, C.; Alagona, G.; Profeta, S.; Weiner, P. A New Force Field for Molecular Mechanical Simulation of Nucleic Acids and Proteins. *Journal of the American Chemical Society* **1984**, *106*, 765-784.
73. Cornell, W. D.; Cieplak, P.; Bayly, C. I.; Gould, I. R.; Merz, K. M.; Ferguson, D. M.; Spellmeyer, D. C.; Fox, T.; Caldwell, J. W.; Kollman, P. A. A Second Generation Force Field for the Simulation of Proteins, Nucleic Acids, and Organic Molecules. *Journal of the American Chemical Society* **1995**, *117*, 5179-5197.
74. Scott, W. R. P.; Hünenberger, P. H.; Tironi, I. G.; Mark, A. E.; Billeter, S. R.; Fennen, J.; Torda, A. E.; Huber, T.; Krüger, P.; van Gunsteren, W. F. The Gromos Biomolecular Simulation Program Package. *The Journal of Physical Chemistry A* **1999**, *103*, 3596-3607.
75. Oostenbrink, C.; Villa, A.; Mark, A. E.; Van Gunsteren, W. F. A Biomolecular Force Field Based on the Free Enthalpy of Hydration and Solvation: The Gromos Force-Field Parameter Sets 53a5 and 53a6. *Journal of Computational Chemistry* **2004**, *25*, 1656-1676.
76. Jorgensen, W. L.; Tirado-Rives, J. The Opls [Optimized Potentials for Liquid Simulations] Potential Functions for Proteins, Energy Minimizations for Crystals of Cyclic Peptides and Crambin. *Journal of the American Chemical Society* **1988**, *110*, 1657-1666.

77. Karplus, M.; Petsko, G. A. Molecular Dynamics Simulations in Biology. *Nature* **1990**, *347*, 631-639.
78. Jorgensen, W. L. The Many Roles of Computation in Drug Discovery. *Science* **2004**, *303*, 1813-1818.

CHAPTER 2

Drug Binding Site at Tubulin

Heterodimer and Dimer

Depolymerization*

2.1 Introduction

Microtubules (MTs) are biopolymers comprising 13 protofilaments, each of which is built of heterodimer α - and β -tubulin subunits. The monomeric subunits are assembled in a head-to-tail alternating layout to form the protofilaments, arranged side-by-side and parallel to the MT longitudinal axis. As the polymerization proceeds, thirteen protofilaments grow spirally and gradually to form a hollow cylinder-like structure, which is the typical appearance of MTs.¹⁻²

The polymerization or assembly of MTs refers to the incorporation of new $\alpha\beta$ -tubulin subunits at MT tips, which corresponds to the elongation or growth state. The depolymerization or disassembly of MTs refers to the detachment of $\alpha\beta$ -tubulin subunits at MT ends, which corresponds to its shortening or shrinkage status. The dynamic

* This chapter was modified from “Microtubules dual chemo and thermo-responsive depolymerization” Li, Z. & Alisaraie, L., *Proteins: Structure, Function, and Bioinformatics* **2015**, 83, 970-981. Used with permission.

variability of MT structure, i.e., random transitions between assembly and disassembly states, is essential for the cellular functions of MTs.³ For instance, kinetochores in the centromere region of chromosomes bind to spindle MTs during mitosis, and mitotic spindles control the movement, alignment and segregation of chromosomes throughout the assembly and disassembly of MTs, coping with each phase in the process of cell division.⁴ The successful process of mitosis strongly depends on high MT dynamicity, since any misalignment or replication error of chromosomes can terminate mitosis and eventually lead to mitotic checkpoint-induced apoptosis.⁵ However, the important dynamics of spindle MTs can be suppressed by some small molecules binding at different sites of MT. The MT-targeted compounds are usually anti-mitotic drugs because they are capable of slowing-down or blocking mitosis, inhibiting fast proliferation of cancer cells and killing tumor cells. Anti-mitotic agents can be classified into two main groups: MT-stabilizing and MT-destabilizing agents. The MT-stabilizers, such as taxanes and eleutherobins, stimulate MT polymerization. The MT-destabilizers, including colchicine, vinca alkaloids such as vincristine and vinblastine, by contrast, inhibit MT polymerization.⁶⁻⁸

Vincalukoblastine, commonly known as vinblastine (VLB, C₄₆H₅₈N₄O₉), is a vinca alkaloid derived from the periwinkle plant *Catharanthus roseus*. It is an indole rich alkaloid comprising catharanthine and vindoline. The World Health Organization (WHO) has listed VLB as one of the most essential medications needed in the health care system because of its powerful efficacy for treatment of Hodgkin's lymphoma, non-small cell lung cancer, breast cancer, head, neck and testicular cancer types.⁹ VLB has been shown

to inhibit the dynamics of growing and shortening at MT plus ends when used at low concentration and hinder MT polymerization at high concentration. The first crystal structure of VLB-tubulin complex was solved by Gigant *et al.*,¹⁰ where the VLB binding site was identified at the inter-dimer interface of $\alpha\beta$ -tubulin heterodimers. Apart from MT-targeted drugs, several other factors, including microtubule-associated proteins (MAPs), temperature, hydrolysis of guanosine triphosphate (GTP) and critical concentration of free tubulins, have been suggested to be crucial in regulating the dynamics of MT polymerization and depolymerization.¹¹⁻¹²

Temperature, a key factor in controlling the switch between growth and shrinkage of MTs, can be used to tune the MTs/tubulins conversion *in vitro*. Early studies showed cold-induced disassembly by monitoring the change of turbidity, polymer weight and length, when a polymerized MT solution at 303 K was rapidly cooled down to 278 K. A conclusion that depolymerization proceeded by the consecutive loss of subunits at MT-ends was drawn based on the significant decrease of the optical density, polymer weight and length.¹³⁻¹⁴ While conformational changes of tubulins seem to play a central role in MT assembly/disassembly processes,¹⁵ no explicit study has yet been reported on associating the drug-induced and low temperature-induced disassembly mechanism with structural variations of MT-heterodimers at the atomic level. The study presented in this chapter examines this importance and investigates induced changes on the structural conformation of MT imposed by both VLB binding, and reduction of temperature to 277 K as opposed to room temperature of 300 K.

Another widely used anticancer drug, doxorubicin (DOX), causes DNA damage to tumor cells but has not yet been further explored in terms of the possible binding site and mechanism of action on MTs at an atomistic level. In fact, the positive effects of DOX on the structural damage and the assembly inhibition of MTs¹⁶ as well as the reorganization of tubulins¹⁷ have been reported. Fromes *et al.* investigated the interference of fluoro-DOX on tubulin polymerization and pointed out that a possible site for fluoro-DOX binding to MT was related to the MAP binding site.¹⁸ The sister drug of DOX in the anthracycline family, daunomycin, was reported to interact with tubulin heterodimers through H bonding and electrostatic force.¹⁹ However, neither explicit experimental evidence nor computational studies have reported detailed DOX interactions with MT. The work presented in this chapter also explores possible binding sites for DOX targeting MT based on a binding pocket finder followed by a refined localization.

2.2 Materials and Methods

2.2.1 *In silico* experimental setup

The $\alpha\beta$ -tubulin heterodimer was retrieved from the Protein Data Bank (PDB)²⁰ with the access code of 1JFF²¹. The missing residues sequenced as 1, 35-60, 440-451 of α -tubulin and 1, 438-445 of β -tubulin were constructed and merged with the X-ray structure of the protein in 1JFF as described elsewhere²² using the complete amino acid sequences of α -tubulin with 451 residues and β -tubulin with 445 residues and respective UniProt²³ access code of Q2HJ86 (Bovine) and P02554 (Pig).

DOX was extracted from 2DR6 in PDB.²⁴ The grid-based HECOMi finder, a web server called *Ghecom*,²⁵ was used to predict the possible binding sites of DOX interacting with $\alpha\beta$ -tubulin heterodimers. Through simultaneous calculations of shallowness and depth of probes with multiple sizes binding to the protein surface, *Ghecom* applies the mathematical morphology idea to detect pockets of ligands, and shows greater advantages than other binding-site searching servers in terms of efficiency and accuracy on binding pocket predictions.²⁵

The *FlexX* package (version 2.1.3)²⁶⁻²⁸ was utilized as the docking tool to search for the most energetically favorable binding conformation of VLB in MT and calculate its total binding score to be used as the starting structure for MD simulations. Polar and non-polar hydrogen atoms were assigned to VLB, while the whole molecule had a net charge of (+1) due to protonation under physiological conditions. Hence, the nitrogen at position 6' in the catharanthine sub-structure of VLB was set as protonated under physiological conditions.²⁹ (**Figure 2.1**)

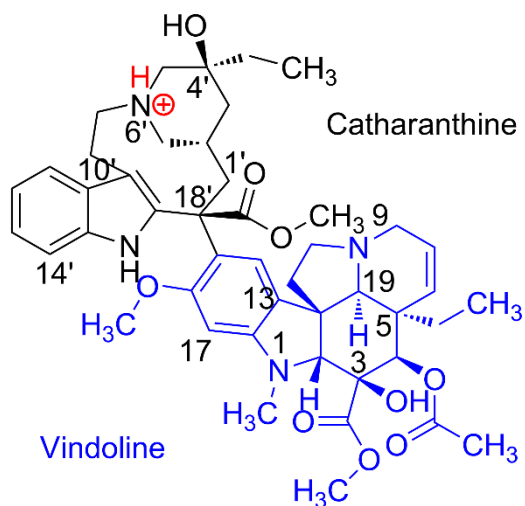


Figure 2.1 Chemical structure of mono-protonated VLB.

FlexX applies an incremental construction algorithm as it selects a fragment of VLB as the base-fragment to place into the designated binding site and adds the remaining fragments of the molecule to connect with the base in an incremental fashion. The output docking solutions of VLB are ranked according to their corresponding total binding energies ($\Delta G_{\text{binding}}$) calculated based on the Böhm scoring function³⁰.

2.2.2 Molecular dynamics (MD) simulations

In order to study the individual effects of VLB and low temperature on tubulin heterodimer structure in dynamic mode, MD simulations were performed after docking VLB into the $\alpha\beta$ -tubulin heterodimer. The starting point structure of the liganded tubulin heterodimer for MD simulations was the heterodimer with VLB docked by *FlexX*. The starting point structure of the unliganded tubulin heterodimer for MD simulations was the heterodimer with VLB removed from the liganded heterodimer. The topology of mono-protonated VLB was generated by Automated Topology Builder (ATB, version 2.0)³¹⁻³² based on Gromos96 force field 53A6³³ followed by a minimization using the Hartree-Fock/STO-3G basis-set. MD simulations were implemented by utilizing the *Gromacs* package (version 4.5.5)³⁴⁻³⁵, with the force field of Gromos96 53A6.

The bonded interactions, including bond stretching, valence angle bending and bond rotation, were modeled based on specific functions; the non-bonded interactions including van der Waals and electrostatic interactions were modeled by the Lennard-Jones potential and electrostatic potential functions, respectively.³³ A cut-off distance of 1.4 nm was assigned for both the Lennard-Jones and electrostatic interactions. The

calculation of electrostatic interactions contributing to energies and forces was carried out based on the Particle Mesh Ewald algorithm³⁶. The LINear Constraint Solver (LINCS) algorithm³⁷ was applied to constrain all bond lengths including those involved in hydrogen bonding. The time constant for pressure coupling was set to 1.0 ps, with compressibility set as $4.5\text{e-}5 \text{ bar}^{-1}$. The temperature was set to either 277 K or 300 K with a temperature coupling of 0.1 ps.

Each simulated system was first energy minimized using the steepest descent algorithm followed by a 100 ps all-bonds position restraint. The harmonic constraints were gradually released during MD simulations. The simulations of three systems converged before 70 ns and proceeded to additional steps until 115 ns. When the first round of simulations for the three systems was completed, a second round of simulations was performed for the sake of validation and improvement of the accuracy of predictions. The velocities assigned to the energy minimized structure were set differently at random; all other settings of the second round simulations were identical to the first round. The results discussed below were based on the dynamic changes observed in both the first and second rounds of simulations. The calculations were performed on WestGrid high performance computer clusters of Compute Canada.³⁸

2.3 Results and Discussions

2.3.1 DOX binding site prediction by *Ghecom* and *FlexX*

The possible binding sites predicted by *Ghecom* were ranked into three areas in ascending order: grid 1, grid 2 and grid 3. Part of grid 1 also overlapped with the binding

site of VLB in the crystal structure of 4EB6³⁹. Central residues at each predicted spot were used to guide the docking of DOX. The radius around the central residues was set to 10 Å. Amino acids within this radius were selected to form the binding site. The central residues represent the center of the estimated site region, the envelope of which encloses the binding site.⁴⁰ Because of the spread area of grid 1, grid 1 was further divided into two areas: one at the top of grid 1, with central residues Ala12, Pro173 and Tyr224 surrounded by H1, T5 loop, H5, H6 and H7 of α -tubulin; the other at the bottom of grid 1, with central residues Ala247 surrounded by T7 loop of α -tubulin and Pro70 surrounded by T2 loop of β -tubulin. The central residues of grid 2 were Gly244 and Thr351, which were surrounded by T7 loop and S9 strand of β -tubulin. The central residues of grid 3 were Lys164 and Leu252 surrounded by H3-S4 loop, H4-S5 loop and H8 of α -tubulin, as well as Ala102 surrounded by T3 loop and H11-H12 loop of β -tubulin. (**Figure 2.2 A-B**)

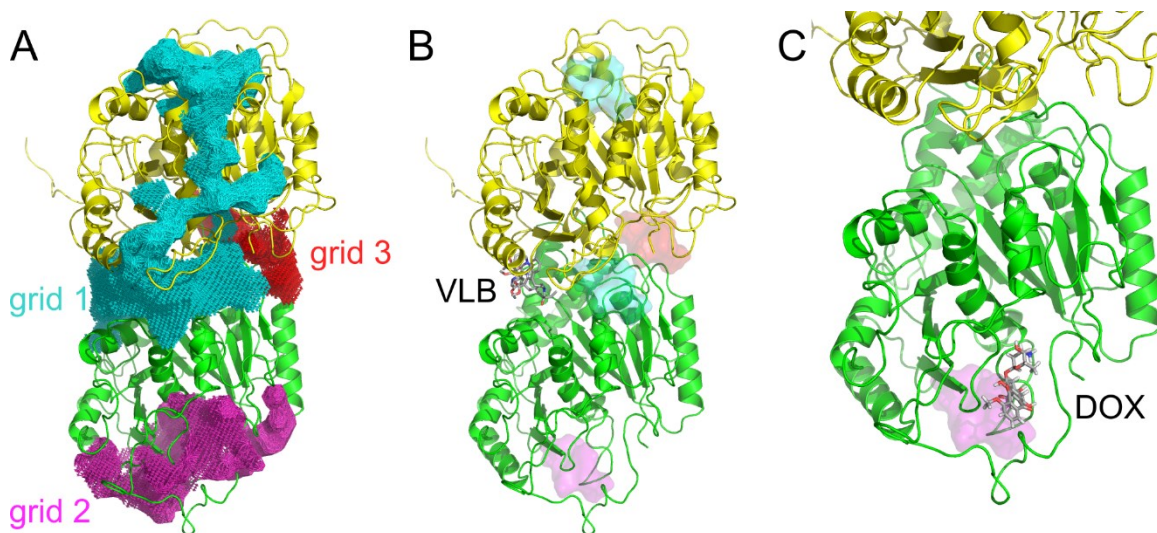


Figure 2.2 DOX binding site prediction. α -tubulin is in yellow and β -tubulin is in green. (A) Binding area predicted by *Ghecom*. Grid 1, the highest ranked cluster, is in cyan. Grid 2 is in magenta, Grid 3 is in red. (B) The positions of the central residues are shown

in surface mode. For comparison, VLB in the crystal structure of 4EB6 is shown in stick mode. (C) The top ranked docking pose of DOX.

Five sets of docking experiments were performed based on the binding sites predicted by *Ghecom*. Grid 2, with the lowest binding free energy, was the most favorable binding site for DOX. The bind pocket refined further by *FlexX* was located at the edge of β -tubulin surrounded by H1-S2 loop, T7 loop, and S9-S10 loop. (Table 2.1 & Figure 2.2 C)

Table 2.1 $\Delta G_{\text{binding}}$ of the DOX docking experiments.

	1	2	3	4	5
Center of prediction	Grid 1 top	Grid 1 bottom	Grid 2	Grid 3	VLB binding site
$\Delta G_{\text{binding}}$ (kJ/mol)	-26.01	-24.66	-29.73	-23.09	-25.61

The binding site of the derivative of DOX, fluoro-doxorubicin, was related to the binding sites of MAPs.¹⁸ Littauer *et al.* reported that residue 434-440 on β -tubulin was crucial for MAPs interacting with tubulins.⁴¹ However, the binding site which was predicted by *Ghecom* and further assessed using *FlexX*, was not close to the carboxyl-terminal of β -tubulin. This inconsistency might be due to the different interactions of DOX and fluoro-DOX with MT, as well as the incomplete sequence of β -tubulin in Littauer's study⁴¹.

2.3.2 VLB bound $\alpha\beta$ -tubulin heterodimer

To benefit from both available crystal structures of tubulin, the uniprot sequence identities as well as tertiary structures of 1JFF²¹ and 4EB6³⁹ were compared. As a result, five residues in α -tubulin and six residues in β -tubulin of 4EB6 were found non-identical

to the counterparts of 1JFF. However, these residues, in either the α - or β -subunit, were far from the VLB binding site, such that the closest non-identical residue was ~ 22 Å away from atom C18' of VLB in 4EB6. This indicates that the VLB surrounding environment in 1JFF is identical to the VLB binding site in 4EB6. As described by Ranaivoson *et al.* the crystal structure of the tubulin was molded in 4EB6, and the ligand location and its coordination were manually corrected to match the electron density map.³⁹ Considering the fact that VLB has a complex chemical structure, and the resolution of the X-ray diffraction data “R” for solving VLB-tubulin in 4EB6 is 3.47 Å, these factors could affect the accuracy of the observed VLB conformational pose in the process of solving the VLB density map and the precise identification of its absolute conformational pose. Moreover, due to the technical limitation in crystallography, hydrogen atoms are not detected. Hence they are not included in the solved structure of VLB-tubulin. As a result, protonation states of amino acids and the ligand are not assigned to the solved structure. To address these issues concerning the conformation of the protonated VLB and identify the ligand coordination more accurately than manually placing the ligand in the crystal structure, the most energetically favorable conformation of VLB in the bound state was searched using docking. (**Figure 2.3**)

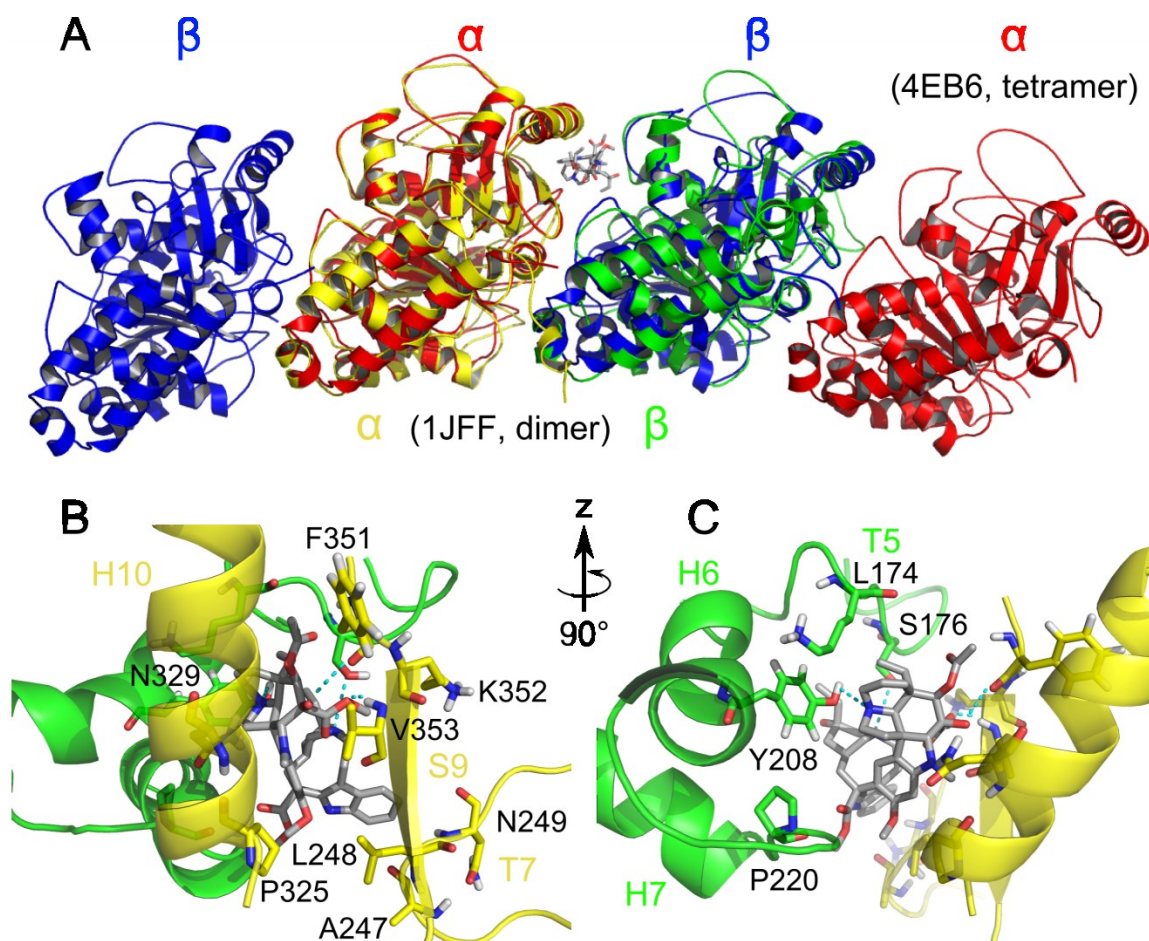


Figure 2.3 VLB binding site. (A) Tubulin heterodimer from 1JFF (α -tubulin yellow, β -tubulin green) superimposed on the VLB-bound tubulin tetramer structure in 4EB6 (α -tubulin red, β -tubulin blue). Residues interacting with VLB in (B) α -tubulin and (C) β -tubulin. VLB in gray stick, hydrogen bonds in cyan dashed line.

Among the top 10 docking solutions, the first ranked and sixth ranked were found close to the crystallographic geometry of VLB by the smallest root mean square deviation (RMSD) of ~ 6 Å. The vindoline part of the two docking geometries were overlapping, the only difference was the orientation of a nine-membered ring where the protonated N

was located. The $\Delta G_{\text{binding}}$ of the first ranked docking solution was calculated to be -8.08 kJ/mol, which was much lower than the sixth ranked solution. Therefore, the geometry of the first ranked docking solution was chosen as the starting structure for the ligand. (**Appendix A** Table A1 & Figure A1)

This binding conformation of VLB is linked to 8 amino acids from α -tubulin and 4 amino acids from β -tubulin in the binding site. Phe351 and Val353 (strand S9) of α -tubulin along with Ser176 (loop T5) and Tyr208 (helix H6) of β -tubulin interact with VLB through hydrogen bonding, where the hydroxyl oxygen on the side chain of Ser176 forms a hydrogen bond with the hydrogen atom of the protonated nitrogen 6' at a distance of 2.4 Å. Val353, Ser176, and Tyr208 interact with VLB via hydrophobic interactions, along with Ala247, Leu248 and Asn249 (loop T7), Pro325 and Asn329 (helix H10), Lys352 (strand S9) of α -tubulin plus Lys174 (loop T5) and Pro220 (the loop between H6 and H7) of β -tubulin. (**Table 2.2** & **Figure 2.3B-C**)

Table 2.2 The amino acids compose the interacting network of VLB in the first ranked docking solution.

Subunit	Binding site							
α-tubulin	Ala247	Leu248	Asn249	Pro325	Asn329	Phe351	Lys352	Val353
β-tubulin	Lys174	Ser176	Tyr208	Pro220				

2.3.3 MD simulation analysis

The RMSD of the protein backbone of the unliganded tubulin heterodimer at 300 K and 277 K, as well as the liganded tubulin heterodimer at 300 K were monitored for the three individual MD simulated experiments within a 115 ns MD trajectory. Each system

converged at a different time step because each had a different path on the energy surface and each simulation was performed independently. For instance, the liganded system was converged (stabilized) at approximately 35 ns, roughly 35 ns earlier than the convergence of the unliganded structures under temperatures of 300 K and 277 K nearly at 70 ns. Thus, the frames from 70 to 115 ns of the trajectories were analyzed throughout the presented work. (Figure 2.4)

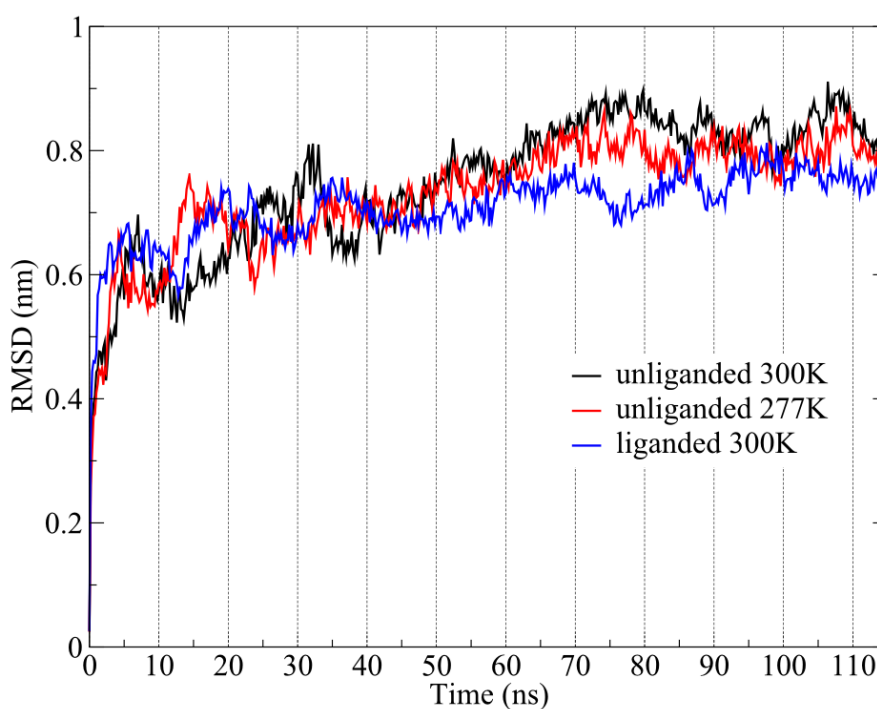


Figure 2.4 The RMSD plots of the unliganded heterodimer at 300 K (black), 277 K (red) and the liganded heterodimer at 300 K (blue) within 115 ns of MD simulations.

2.3.4 VLB-induced conformational changes

When a ligand binds to a protein, it causes the binding site to change its shape. This is known as induced fit that affects the shape, folding, and activity of the targeted protein.⁴²⁻

⁴⁴ The induced fit occurred as a result of VLB binding. For instance, H10 (α 325-331) occupied a portion of the binding site in the absence of VLB. However, it shifted away from VLB and partially unfolds to a loop (residues 325-327) in the presence of VLB, due to the expanding of the binding site space. (**Figure 2.5A**)

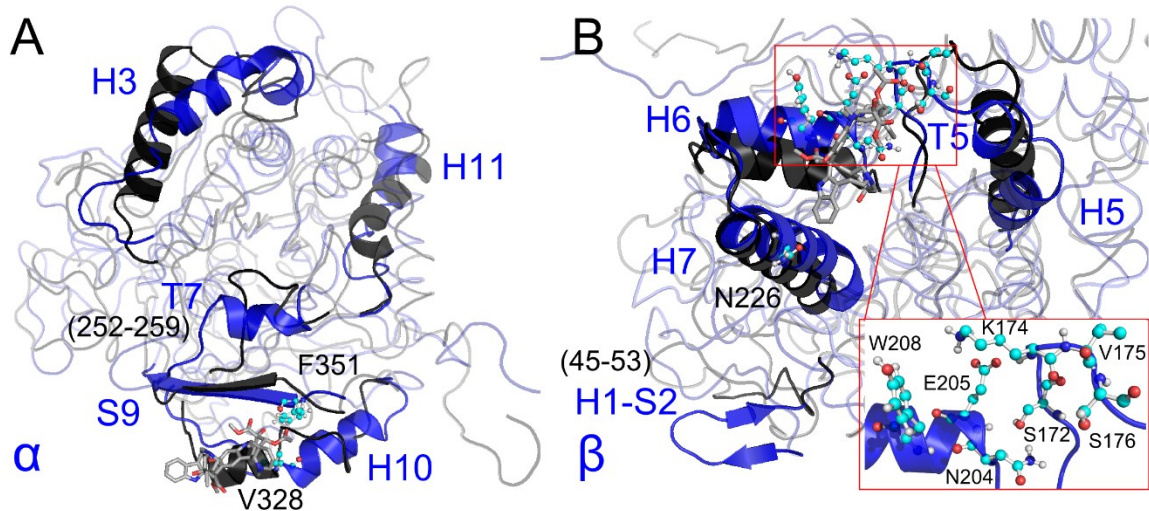


Figure 2.5 Main conformational changes of the liganded heterodimer compared to the unliganded heterodimer at 300 K. Both structures are taken from the 105 ns frames of the two separate experiments. The liganded (A) α -tubulin and (B) β -tubulin (blue) are superimposed on the corresponding unliganded tubulins (black). Residues interacting with VLB (cyan ball-and-stick). The inset at (B) shows a close-up of the interacting residues of T5 and H6.

The repositioning and folding changes of H10 are mainly due to the contribution of Val328 in the VLB-tubulin interaction. Furthermore, S9 in the liganded α tubulin extended three residues, from α 352-356 to α 351-358, and moved ~ 1.7 Å toward VLB as compared to the unliganded state. The interaction of Phe351 with VLB facilitated the

extension of the S9 strand length. H3 and H11, located away from the binding site, both shrank and became shorter than their unliganded counterparts as a result of the partial unfolding to a simple coil. Particularly noteworthy is a newly formed helix which consists of residues α 252-259 at the T7 loop. Helicity plot shows that the newly formed helix exists for as long as ~65% of the entire simulation time. (**Appendix A Figure A2**)

Conformational changes are also seen in β -tubulin. In the presence of VLB, H6 shifted ~3.5 Å away from its unliganded pose, increasing the volume of the VLB binding site. Meanwhile, Asn204, Glu205 and Tyr208 at H6 developed interactions with VLB. H7 shifted ~1.8 Å toward VLB and contributed Asn226 to the interaction network. Residues β 181-186 of H5 were unfolded to a loop along with T5 shifting toward VLB, such that Ser172, Lys174, Val175 and Ser176 on the loop established interactions with VLB via hydrophobic interactions. This apparently caused unfolding of the adjacent H5. The loop H1-S2 (residues 45-47 and 51-53) was located away from VLB binding site but changed to a β -hairpin. This flexible loop is effective in the longitudinal interaction and stabilization of MT, hence the diminishing conformational freedom through the partial conversion of the loop to a β -sheet could have a destabilization effect. (**Figure 2.5B & Appendix A Figure A3**)

Water molecules have shown an important role in stabilizing VLB through the water-mediated hydrogen bonds. The H-bonding network at the 110 ns frame of the liganded system started with Gln15 of H1 in β -tubulin, extended via 7 water molecules, and ended with Val353 of S9 in α -tubulin. VLB formed two hydrogen bonds with water molecules: one occurred at the hydrogen atom on protonated N6' at the catharanthin moiety, and the

other was at the carbonyl oxygen of the ester group at C3 in the vindoline sub-structure of VLB. At the same carbonyl oxygen, VLB also formed a hydrogen bond with Val353. Water molecules built a link between β -tubulin, VLB and α -tubulin, and enhanced the drug-receptor interactions through H-bonding network. Therefore, both water mediated H-bonding and the hydrophobic interactions between the drug and the tubulin heterodimer, contribute to the folding alterations and relocations of the segments around the binding site as seen in S9 moving toward VLB.

2.3.5 Cold-induced conformational changes

As compared to the unliganded tubulin heterodimer at 300 K, five major variations were found in α -tubulin and four major variations in β -tubulin under the low temperature condition of 277 K. In α -tubulin, H5 (185-197) was unfolded to a loop whereas H3, H10 and H11 were elongated, covering residues 106-111, 323-337 and 398-401, respectively. (**Figure 2.6A & Appendix A Figure A4**)

Under the aforementioned condition in β -tubulin, the H3 shrank from residues 110-125 down to residues 110-122. H5 was shortened from residues 180-193 down to residues 184-190. H7 was shortened from residues 222-241 to residues 222-233. A β -hairpin was also created by H1-S2 loop (residues 34-36, 41-43). (**Figure 2.6B & Appendix A Figure A5**)

A newly formed helix (252-259) was also found at the same region of the loop T7 as in the liganded system. The helix was formed in both experiments: VLB binding and low temperature. The helix existed for $\sim 70\%$ of the simulation time in the unliganded and low

temperature systems at 277 K, which lasted a shorter period of time than that of the liganded system. (Appendix A Figure A2 & A4)

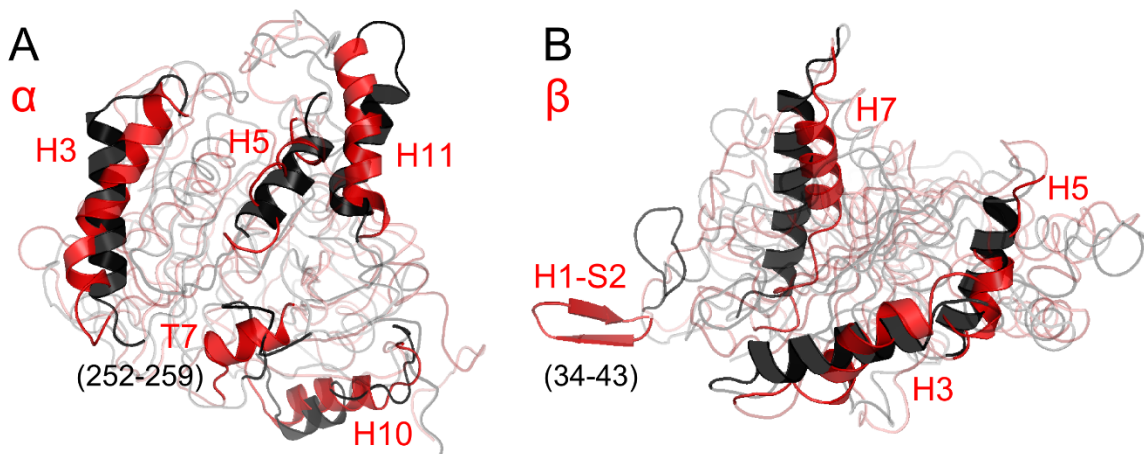


Figure 2.6 Major structural changes of the unliganded heterodimer at different temperatures. (A) α -tubulin and (B) β -tubulin at 277 K (red) superimposed on the equivalent unliganded subunits at 300 K (black) at 105 ns frame of MD trajectory.

VLB and low temperature both triggered the formation of a new helix at the same region of T7 loop; the elongation of H10 in α -tubulin. They also caused the formation of a β -hairpin at H1-S2 loop and the partial unfolding of H5 in β -tubulin. However, H3 and H11 of α -tubulin were partially unfolded in the VLB-bound system but their folding was enhanced in the low temperature system.

The region of α -T7-H8 along with β -T3 and T5 loops in MT may be coordinated by the exchangeable nucleotide site (E-site) and behave like a cohesive structural unit across the longitudinal interface.^{22, 44} The interaction of β -T5 with VLB and the partial conversion of α -T7 to a helix containing the key residue Glu254 for GTPase activity,^{10,45} as shown by MD simulations at both the drug-binding and low temperature scenarios,

imply that low temperature and VLB could potentially affect the contact of E-site nucleotide, and consequently slow down the hydrolysis or exchange rate of E-site nucleotide suppressing MT polymerization.⁴⁶

A previous study has shown that the H1-S2 loop functionalized the lateral contacts of protofilaments and H3 involved in the longitudinal contacts of heterodimers. H10 participated in both the longitudinal and lateral contacts and T7 involved the nucleotide region interaction.⁴⁷ For example, the transformation of H1-S2 loop to a β -hairpin stimulated by VLB and low temperature causes the loss of structural flexibility and further leads to MT depolymerization by weakening lateral contacts. Correlating with the aforementioned data⁴⁷, the structural variations affecting the longitudinal and lateral contacts through the H1-S2 loop, H3, and H10 imposed by both the drug and low temperature in MD simulations demonstrate their potential depolymerization effects.

2.3.6 Solvent accessible surface area of heterodimer

The solvent accessible surface area (SASA) is defined as the total surface area of an atom subtracting the contact area with its neighboring atoms, where the more contacts with surrounding atoms, the less the SASA.⁴⁸ Because the unliganded and liganded tubulins are immersed in water, one tubulin heterodimer with less water accessible surface area corresponds to more interatomic interactions. To minimize the effects of highly fluctuating simple coils on SASA plots, the C-terminal extended loop of α -tubulin (437-451) and β -tubulin (426-445) were omitted for SASA calculations. The SASA for the rest of α - and β -tubulin shows α -tubulin is more water-exposed than β -tubulin for each system.

(Figure 2.7)

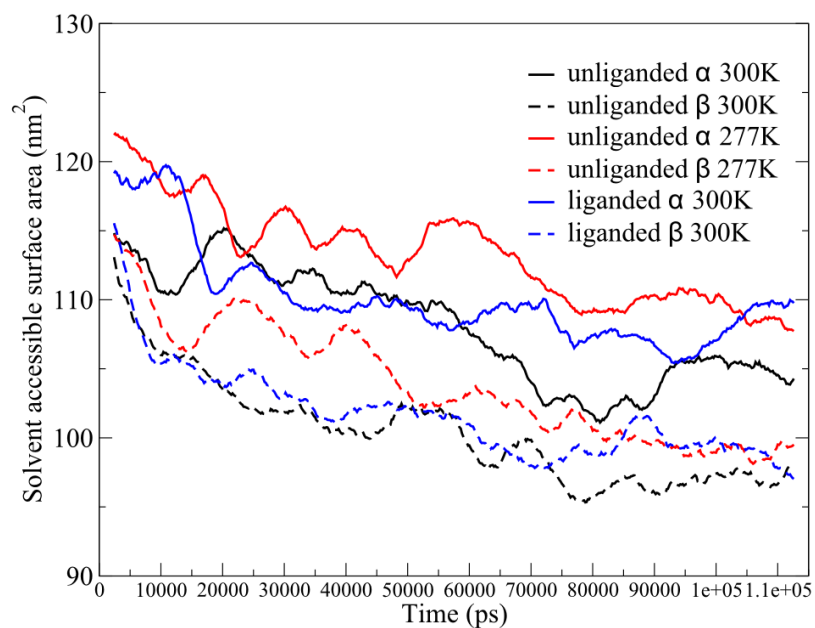


Figure 2.7 SASA of α - and β -tubulin in three systems varying over the 115 ns simulation time.

Furthermore, there is higher percentage of helically folded segments in β -tubulin versus α -tubulin. For instance, a longer H12 is seen in β -tubulin than in α -tubulin for all three systems. This is revealed by the helicity plot over the entire simulation time. **(Figure 2.8A)**

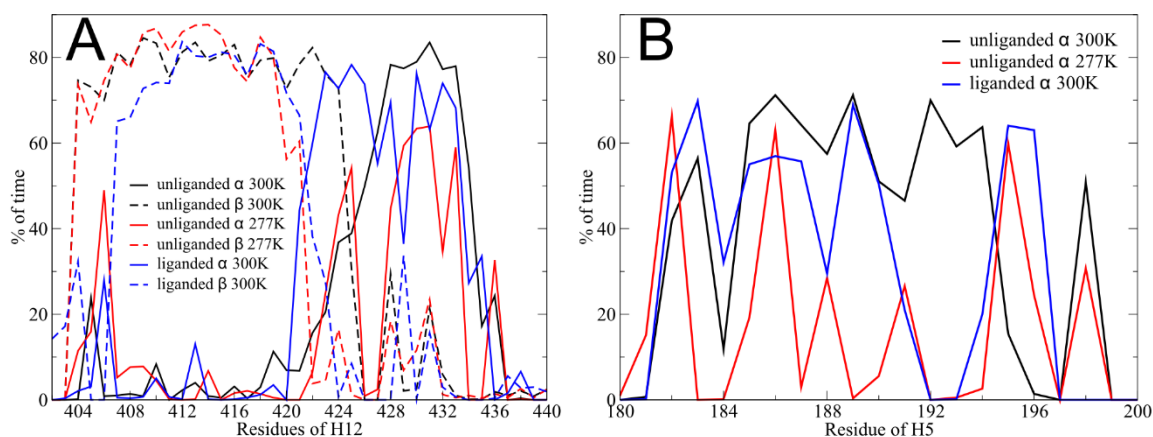


Figure 2.8 Helicity plots, (A) H12 in α - and β -tubulin, (B) H5 in α -tubulin.

The average SASA values were estimated after the convergence of each system. For the unliganded heterodimer at 300 K, the average SASA of the α -tubulin and β -tubulin were $\sim 104 \pm 2 \text{ nm}^2$ and $\sim 97 \pm 1 \text{ nm}^2$, respectively. For the unliganded heterodimer at 277 K, the average SASA of its α - and β -tubulin were $\sim 109 \pm 1 \text{ nm}^2$ and $\sim 99 \pm 1 \text{ nm}^2$, respectively. The α - and β -tubulin of the unliganded system at 277 K are more accessible to water than those at 300 K by $\sim 5 \text{ nm}^2$ and $\sim 2 \text{ nm}^2$, respectively. For the liganded heterodimer at 300 K, the average SASA of its α - and β -tubulin were $\sim 108 \pm 2 \text{ nm}^2$ and $\sim 99 \pm 1 \text{ nm}^2$, respectively. The α - and β -tubulin of the liganded system at 300 K are more water-exposed than those of the unliganded system at 300 K by $\sim 4 \text{ nm}^2$ and $\sim 2 \text{ nm}^2$, respectively. (**Figure 2.7**)

The SASA plots demonstrate that the overall comparable destabilization effect to the α - and β -tubulin is caused by low temperature and VLB, because the average SASA value of each subunit is greater than the corresponding subunit of the unliganded system

at 300 K. For instance, the destabilization of α -H5 occurred in the low temperature and liganded systems over the course of simulation time. (**Figure 2.8B**)

While some segments in scattered areas were stabilized, such as the elongation of α -H3, H10 and H11 in the low temperature system, α -H10 and S9 in the liganded system and the newly formed helix (α 252-258) at T7 loop as well as the β -hairpin at β H1-S2 loop in both the low temperature and liganded systems, the dominant effect attributed to low temperature and VLB is to reduce the stability of the whole structure when taking into account all the changes in the secondary structure.

The SASA plots of the H1-S2 loop of α - and β -subunit for the three systems exhibited an average water accessible area of nearly 25 nm² after the corresponding convergence time of each system. The SASA plots were calculated for 40 residues of H1-S2 loops in each subunit. In α - and β -subunits, 21 and 24 residues respectively were polar resulting in the relatively large SASA. (**Appendix A Figure A6**)

2.3.7 Curvature change of heterodimer

H7 is a central helix in α - and β -tubulin that orients along the longitudinal axis of MT protofilaments. It translates accordingly during the reversible straight to bent conformational conversion under the disassembly or assembly process.⁴⁹⁻⁵⁰ Therefore, H7 helices in monomers were chosen for monitoring the curvature change of heterodimers under different conditions. The reference structure for the comparison was the crystal structure of the tubulin with VLB in 4EB6³⁹, because the bent conformation of a tubulin complex with the stathmin-like domain of the RB3 protein (SLD-RB3) was similar to the

curved protofilaments, which caused a loss of lateral contacts and subsequent disassembly.⁴⁹

Heterodimer structures were taken from the 70, 90, 100, and 110 ns frames of the three MD simulation systems, in order to assess the trend of conformational changes as compared to the VLB-bound dimer in the crystal structure as the reference structure. Keeping the β -subunit of the VLB-bound 4EB6 fixed, and superimposing the β -H7 of MD simulated structures on the β -H7 in 4EB6, the orientation of α -H7 exhibited the curvature deviating from the observed bent conformation in the crystal structure. (**Figure 2.9**)

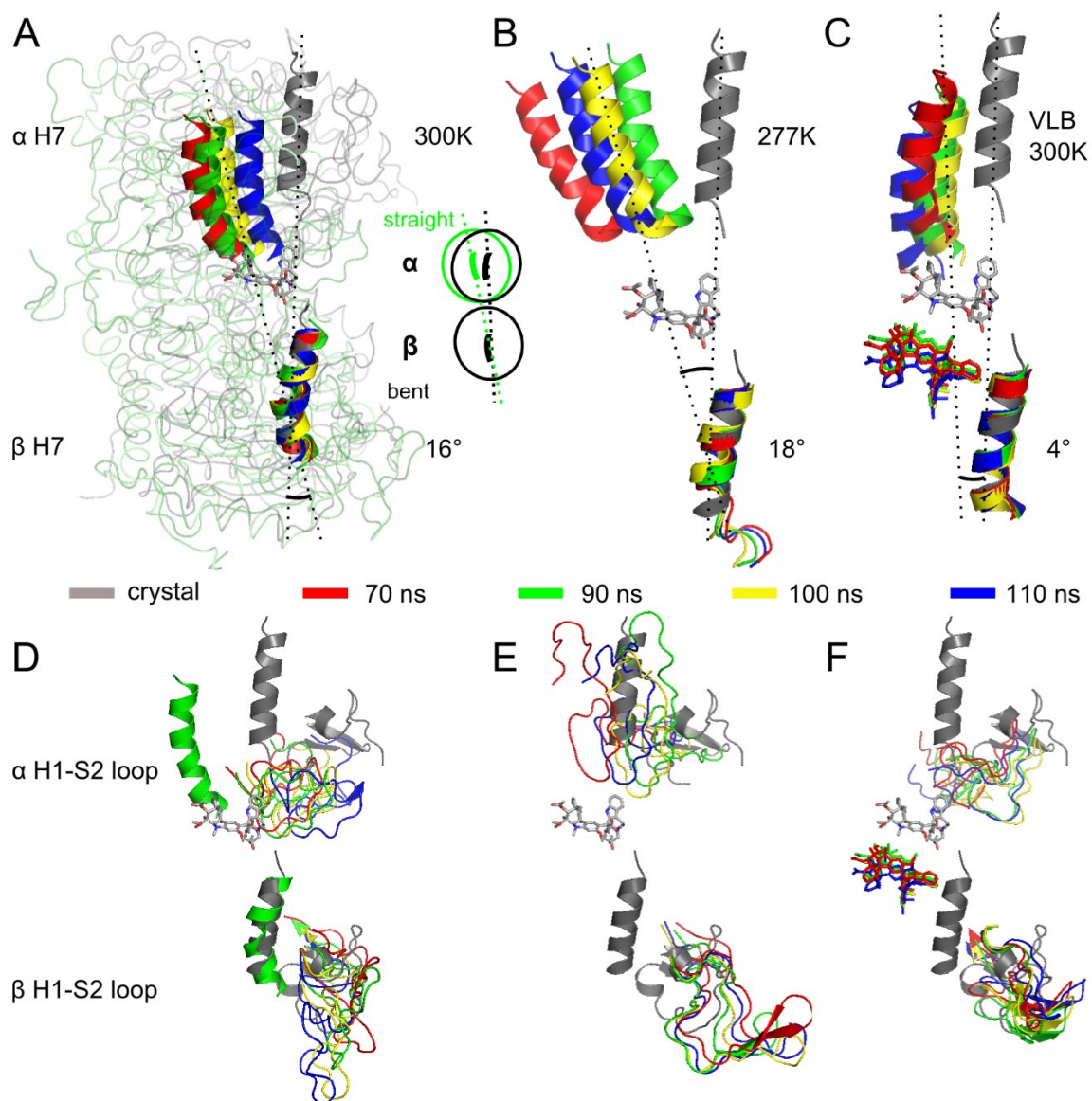


Figure 2.9 The curvature of $\alpha\beta$ -tubulin heterodimer represented by H7 orientation. The unliganded heterodimer at (A) 300 K and (B) 277 K as well as (C) the liganded heterodimer at 300 K. The angles indicate the average deviation of heterodimers shifting from the curved conformation in the crystal structure. The inset scheme at (A) describes a bent to straight conversion. The conformation of H1-S2 loops in the unliganded

heterodimer at (D) 300 K, (E) 277 K and in (F) the liganded heterodimer at 300 K. For clarity, only H7 helices are highlighted in cartoon mode.

The unliganded α -H7 at 300 K was ~ 12 - 25° shifted away from the reference line passing through the H7 helices in the crystal structure, while the unliganded α -H7 at 277 K was ~ 15 - 28° shifted away from the reference line. The liganded α -H7 of 300 K oriented in a similar way to the α -H7 in the crystal structure. It was shifted ~ 0 - 4° away from the reference line and nearly parallel to the orientation of that in the crystal structure.

The conformation and orientation of the monomers in the starting structure, obtained from the position restraint step of the calculations, were similar in all three systems. For instance, the orientation of H7 pair in the starting structure exhibited the same bent structural posture as in 4EB6³⁹. The unliganded systems at both 277 K and 300 K showed significant deviations from the curved conformation in the crystal structure during the course of simulation time, indicating the bent to straight conformation conversion in the absence of the drug. However, the liganded system at 300 K maintained similar curved conformation to the crystal structure during the MD simulation. Although the low temperature can cause changing the curvature of the heterodimer structure, it has less effect on bending than that of the drug due to the direct interactions between the drug and the β -H7. These observations correlate with the results of the second MD trajectories for each of the aforementioned experimental conditions. Compared with the first round trajectories, in the second set of experiments, the same frames exhibited stronger effect of

drug on bending the structure, more than shown in the X-ray structure. (**Figure 2.6B**, **Figure 2.9** & **Appendix A** Figure A7)

Several tubulin segments have been reported to play vital roles in establishing the lateral contacts, including the loop H1-S2, H2-S3, H4-T5 and the M loop (272-288).⁴⁷ According to our MD simulation results, the H1-S2 loop (residues 24-63) showed noticeable conformational changes. For the unliganded system at 300 K, no significant change occurred on the H1-S2 loop in both α - and β -subunit. However, the H1-S2 loop in the β -subunit converted to a β -hairpin at frame 70 and 90 ns at 277 K. For the liganded system at 300 K, no significant change occurred on the H1-S2 loop in α -subunit, whereas the H1-S2 loops of β -subunit altered to β -hairpins at 70, 90, 100, and 110 ns time frames. (**Figure 2.9D-F**)

The curvature of protofilaments accompanied by the loss of lateral interactions leads to MT disassembly.⁴⁹ The loss of lateral contacts can be seen from the change of H1-S2 loops into β -hairpins, identified in β -subunit of both the unliganded and liganded systems at low temperature. This means β -subunit is more sensitive than α -subunit in responding to low temperature and the drug binding. Since the conversion of the H1-S2 loop to a β -hairpin in the liganded system is more prevalent than that in the low temperature system, we may infer that VLB presumably has a stronger effect than low temperature on causing the loss of lateral contacts established by the H1-S2 loop in β -subunit.

2.3.8 Electrostatic potential map at the interface

The distribution of electrostatic potential map at the interdimeric interface reflects the strength of longitudinal contacts contributed by electrostatic forces. At the heterodimer

interface region of the unliganded heterodimers at 300 K, a groove was observed with higher accumulation of positively charged residues inside and surrounded by negatively charged residues. At the equivalent region of the unliganded heterodimer under low temperature, a groove was seen with less accumulation of positively charged residues, which was surrounded by a dense negatively charged surface. (**Figure 2.10A-D**)

The electrostatic forces among oppositely charged residues in the groove at 300 K occurred among amino acids, including Lys103, Glu108, Glu401 in β -subunit, and Arg2, Lys163-164, Arg264 in α -subunit. (**Figure 2.10E**)

The repulsive forces in the groove dominated by negatively charged residues at the interface of the heterodimer at 277 K occurred between Glu196 in α -subunit and Glu401, Trp101, Trp397 as well as Tyr398 in β -subunit. Thus, the electrostatic repulsion in the unliganded system at 277 K is larger than in the unliganded system at 300 K based on the density, arrangement and orientation of negatively charged residues. (**Figure 2.10A-E**)

The electrostatic attraction as well as repulsive forces occurring among charged residues of α - and β -subunits influence the geometry, shape and size of the groove. Among these charged residues were β Glu108- α Arg2, β Glu401- α Lys163, and α Glu196- β Glu401. (**Figure 2.10E**)

The distances between centers of mass (DCOMs) of charged amino acids were relatively stable, consequently, the size, shape and distribution of the electrostatic surface remained relatively steady throughout the 115 ns simulation time. (**Appendix A Figure A8 A-C**)

VLB binding also affects the distribution of the electrostatic potential map of the binding site. (**Figure 2.10F-I**)

In the absence of VLB, the two aspartate residues of β -Asp209 in H6 and α -Asp327 in H10 were located 4.9 Å apart from each other, that contribute to the negatively charged region around the pocket. They were surrounded by the positively charged β -Arg213, Lys297 and α -Lys336. (**Figure 2.10J**)

Residues β Asp209 and β Asp304 were close to α Lys326. The surrounded positively charged residues of the site, including β Lys174, β Arg213, β Lys216, and α Lys326, contributed to repulsive forces between the two subunits.

In the presence of VLB, β -Asp209 and α -Asp327 were separated by 14 Å away because the possessing helices, β -H6 and α -H10, shifted away from the drug, providing additional space for its binding. Since they were negatively charged, these displacements resulted in reducing the distribution of the negative electrostatic surface at the center of the binding site.

In the VLB-bound system, the N-terminal end of H10 unfolded to a loop, shifting Lys326 away from the two aspartate residues. The displacement of the charged residues altered the distribution of the map, as the DCOMs changed among the residues. This occurred, for instance, in the pair of β Asp209- α Lys326 for ~1.56 nm versus ~0.60 nm, and ~2.92 nm versus ~0.51 nm in the pair of β Asp304- α Lys326.

The attractions of other contributing charged residues, such as β Arg213 and α Asp327, were also undermined as a result of VLB binding based on the alteration of DCOM between these two residues, by a separation of up to 0.86 nm versus ~1.85 nm. These

alterations were observable throughout the 115 ns trajectories. (**Appendix A** Figure A8 D–F)

VLB and low temperature both alter the distribution of the electrostatic surface such that they weaken the longitudinal interactions of the tubulin heterodimer.

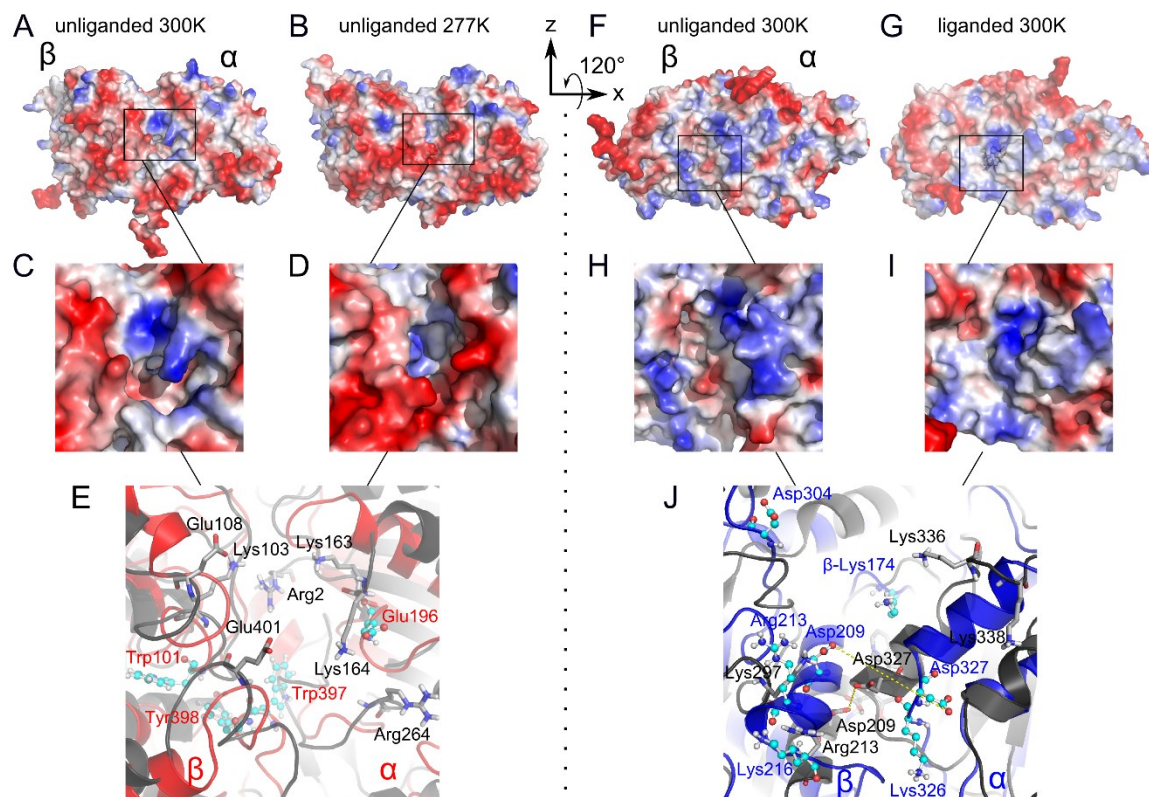


Figure 2.10 The surface electrostatic potential map in vacuum of the unliganded and liganded $\alpha\beta$ -heterodimer. The unliganded heterodimer at (A) 300 K and (B) 277 K. Negatively charged surface (red) and positively charged surface (blue). (C) and (D) are the close-up view of the selected area in (A) and (B), respectively. The surface electrostatic potential map *in vacuo* of (F) the unliganded and (G) the liganded $\alpha\beta$ -heterodimer at 300 K. (H) and (I) are the enlarged view of the selected areas in (F) and (G), respectively. (E) and (J) are residues contributing to the electron distribution in the

selected areas. Residues from the unliganded system at 300 K (gray stick), those of the unliganded system at 277 K as well as residues from the liganded system at 300 K (cyan ball-and-stick). Structures of each system are from the 100 ns frame of MD trajectories.

2.4 Conclusions

This work explores the possible binding site of doxorubicin at the $\alpha\beta$ -tubulin heterodimer. We provide insights into the conformational changes of tubulin dimer imposed by binding to the anti-mitotic drug vinblastine, and a low temperature condition by means of molecular dynamics simulation.

The DNA targeted reagent doxorubicin showed favorable affinity to the $\alpha\beta$ -tubulin heterodimer with the lowest binding free energy of -29.73 kJ/mol. The binding site of DOX predicted by *Ghecom* and *FlexX* is located at the edge of β -tubulin, surrounded by H1-S2 loop, T7 loop, and S9-S10 loop.

Taking into account the temperature variable in VLB-MT systems, this study has assessed various possible conformations of the heterodimer to fill the knowledge-gap between the data available from the low resolution crystal structures of tubulin and information from *in vivo/in vitro* experiments, for its applications on intensifying MT-depolymerization process toward suppressing mitosis in cancerous cells.

Our computational calculation results are in line with the experimental data showing the compressive and bending modulus of MT at different temperatures (5-37 °C) using atomic force microscopy, where the temperature-induced changes were correlated to the strength of lateral interactions between MT protofilaments.⁵¹

In this study, VLB has been shown to have a major effect on folding H10 and S9 in α -tubulin. Not only was the secondary structure of the segments around the binding pocket influenced by the binding of an anti-mitotic drug, but also H3 and H11 of α -tubulin as well as the H1-S2 loop of β -tubulin were altered, even though they were away from the binding site as shown in the variation of helicity percentage throughout the entire simulation time.

Low temperature of 277 K caused the unfolding of H5 and simultaneously resulted in the elongation of H3 and H11 in α -tubulin. Reducing temperature also caused the partial unfolding of H7 to a simple coil in β -tubulin.

Interestingly, the two independent factors of temperature and an anti-mitotic agent in some regions of the protein facilitated similar changes, such as the formation of a new helix at T7 and the elongation of H10 in α -tubulin, the partial unfolding of H5 and formation of the β -hairpin at H1-S2 in β -tubulin. H1-S2, H3, T7 and H10 are functional segments; they are known to play key structural roles in depolymerization of MT protofilaments by involving in either the longitudinal or lateral contacts.

The α - and β -tubulin of the unliganded system at 277 K and those of the liganded system at 300 K are more water-exposed than those of the unliganded system at 300 K, indicating their overall destabilization effects on the heterodimer structure as a whole. The curvature of the dimer structure represented by the orientation of the central H7 helices demonstrates the bent to straight conversion in the absence of VLB. By contrast, the liganded system maintains similar curved conformation as in the crystal structure due to the interactions of VLB with H7 in β -subunit. VLB presumably has a stronger effect

than low temperature on causing the loss of lateral contacts of H1-S2 loop in β -subunit based on the more prevalent folding change from a loop to a β -hairpin. Flexibility of the loop facilitates a larger number of interactions, hence, its folding to a more rigid β -hairpin results in decreasing the number of interactions and the destabilization at contact areas.

The distribution of the electrostatic potential map is altered by the variation of the distances among the contributing charged and polar amino acids in and around the VLB binding site as well as those at the interface of two subunits. The observations indicate weakening the longitudinal interactions as a result of VLB binding or reducing temperature from 300 to 277 K.

The insights of this study assist in better understanding the dynamics of tubulin depolymerization, caused by the chemotherapeutic agent vinblastine, and a physical factor such as temperature. The results are beneficial for developing more effective and tolerable drug-responsive and temperature-responsive therapeutic strategies to serve cancer patients through the inhibition of mitosis in cancerous cells. This study also provides foundational knowledge for developing effective drug delivery systems by taking into account specific chemical and environmental variables for increasing the drug–target sensitivity.

2.5 Bibliography

1. Mandelkow, E.; Mandelkow, E.-M. Microtubule Structure. *Current Opinion in Structural Biology* **1994**, *4*, 171-179.

2. Desai, A.; Mitchison, T. J. Microtubule Polymerization Dynamics. *Annual Review of Cell and Developmental Biology* **1997**, *13*, 83-117.
3. Fygenson, D. K.; Braun, E.; Libchaber, A. Phase Diagram of Microtubules. *Physical Review E* **1994**, *50*, 1579-1588.
4. Wade, R. On and around Microtubules: An Overview. *Molecular Biotechnology* **2009**, *43*, 177-191.
5. Stanton, R. A.; Gernert, K. M.; Nettles, J. H.; Aneja, R. Drugs That Target Dynamic Microtubules: A New Molecular Perspective. *Medicinal Research Reviews* **2011**, *31*, 443-481.
6. Jordan, M. A. Mechanism of Action of Antitumor Drugs That Interact with Microtubules and Tubulin. *Current Medicinal Chemistry -Anti-Cancer Agents* **2002**, *2*, 1-17.
7. Jordan, M. A.; Wilson, L. Microtubules as a Target for Anticancer Drugs. *Nature Reviews Cancer* **2004**, *4*, 253-265.
8. Bau, R.; Jin, K. K. Crystal Structure of Vinblastine. *Journal of the Chemical Society, Perkin Transactions 1* **2000**, 2079-2082.
9. WHO Model Lists of Essential Medicines.
<http://www.who.int/medicines/publications/essentialmedicines/en/> (accessed January 11, 2016).
10. Gigant, B.; Wang, C.; Ravelli, R. B. G.; Roussi, F.; Steinmetz, M. O.; Curmi, P. A.; Sobel, A.; Knossow, M. Structural Basis for the Regulation of Tubulin by Vinblastine. *Nature* **2005**, *435*, 519-522.

11. Correia, J. J.; Williams, R. C. Mechanisms of Assembly and Disassembly of Microtubules. *Annual Review of Biophysics and Bioengineering* **1983**, *12*, 211-235.
12. Valiron, O.; Caudron, N.; Job, D. Microtubule Dynamics. *Cellular and Molecular Life Sciences CMLS* **2001**, *58*, 2069-2084.
13. Johnson, K. A.; Borisy, G. G. Kinetic Analysis of Microtubule Self-Assembly in Vitro. *Journal of Molecular Biology* **1977**, *117*, 1-31.
14. Karr, T. L.; Kristofferson, D.; Purich, D. L. Mechanism of Microtubule Depolymerization. Correlation of Rapid Induced Disassembly Experiments with a Kinetic Model for Endwise Depolymerization. *Journal of Biological Chemistry* **1980**, *255*, 8560-6.
15. Valiron, O.; Arnal, I.; Caudron, N.; Job, D. Gdp-Tubulin Incorporation into Growing Microtubules Modulates Polymer Stability. *Journal of Biological Chemistry* **2010**, *285*, 17507-17513.
16. Rabkin, S. W.; Sunga, P. The Effect of Doxorubicin (Adriamycin) on Cytoplasmic Microtubule System in Cardiac Cells. *Journal of Molecular and Cellular Cardiology* **1987**, *19*, 1073-1083.
17. Grzanka, A.; Grzanka, D.; Orlikowska, M. Cytoskeletal Reorganization During Process of Apoptosis Induced by Cytostatic Drugs in K-562 and HI-60 Leukemia Cell Lines. *Biochemical Pharmacology* **2003**, *66*, 1611-1617.
18. Fromes, Y.; Gounon, P.; Tapiero, H.; Fellous, A. Effects of Fluoro-Doxorubicin (Me2303) on Microtubules: Influence of Different Classes of Microtubule-Associated Proteins. *Journal of Protein Chemistry* **1996**, *15*, 561-573.

19. Na, C.; Timasheff, S. N. Physical-Chemical Study of Daunomycin-Tubulin Interactions. *Archives of Biochemistry and Biophysics* **1977**, *182*, 147-154.
20. Protein Data Bank. <http://www.pdb.org> (accessed October 15, 2015).
21. Löwe, J.; Li, H.; Downing, K. H.; Nogales, E. Refined Structure of A β -Tubulin at 3.5 Å Resolution. *Journal of Molecular Biology* **2001**, *313*, 1045-1057.
22. Alisaraie, L.; Tuszynski, J. A. Determination of Noscapine's Localization and Interaction with the Tubulin-A/B Heterodimer. *Chemical Biology & Drug Design* **2011**, *78*, 535-546.
23. UniProt. <http://www.uniprot.org> (accessed October 11, 2015).
24. Murakami, S.; Nakashima, R.; Yamashita, E.; Matsumoto, T.; Yamaguchi, A. Crystal Structures of a Multidrug Transporter Reveal a Functionally Rotating Mechanism. *Nature* **2006**, *443*, 173-179.
25. Kawabata, T. Detection of Multiscale Pockets on Protein Surfaces Using Mathematical Morphology. *Proteins: Structure, Function, and Bioinformatics* **2010**, *78*, 1195-1211.
26. Rarey, M.; Kramer, B.; Lengauer, T.; Klebe, G. A Fast Flexible Docking Method Using an Incremental Construction Algorithm. *Journal of Molecular Biology* **1996**, *261*, 470-489.
27. Gohlke, H.; Hendlich, M.; Klebe, G. Knowledge-Based Scoring Function to Predict Protein-Ligand Interactions. *Journal of Molecular Biology* **2000**, *295*, 337-356.
28. Rarey, M.; Kramer, B.; Lengauer, T. Docking of Hydrophobic Ligands with Interaction-Based Matching Algorithms. *Bioinformatics* **1999**, *15*, 243-250.

29. Pajeva, I. K.; Wiese, M. Pharmacophore Model of Drugs Involved in P-Glycoprotein Multidrug Resistance: Explanation of Structural Variety (Hypothesis). *Journal of Medicinal Chemistry* **2002**, *45*, 5671-5686.
30. Böhm, H.-J. Prediction of Binding Constants of Protein Ligands: A Fast Method for the Prioritization of Hits Obtained from De Novo Design or 3d Database Search Programs. *Journal of Computer-Aided Molecular Design* **1998**, *12*, 309-309.
31. Canzar, S.; El-Kebir, M.; Pool, R.; Elbassioni, K.; Malde, A. K.; Mark, A. E.; Geerke, D. P.; Stougie, L.; Klau, G. W. Charge Group Partitioning in Biomolecular Simulation. *Journal of Computational Biology* **2013**, *20*, 188-198.
32. Malde, A. K.; Zuo, L.; Breeze, M.; Stroet, M.; Poger, D.; Nair, P. C.; Oostenbrink, C.; Mark, A. E. An Automated Force Field Topology Builder (Atb) and Repository: Version 1.0. *Journal of Chemical Theory and Computation* **2011**, *7*, 4026-4037.
33. Oostenbrink, C.; Villa, A.; Mark, A. E.; Van Gunsteren, W. F. A Biomolecular Force Field Based on the Free Enthalpy of Hydration and Solvation: The Gromos Force-Field Parameter Sets 53a5 and 53a6. *Journal of Computational Chemistry* **2004**, *25*, 1656-1676.
34. Van Der Spoel, D.; Lindahl, E.; Hess, B.; Groenhof, G.; Mark, A. E.; Berendsen, H. J. C. Gromacs: Fast, Flexible, and Free. *Journal of Computational Chemistry* **2005**, *26*, 1701-1718.
35. Hess, B.; Kutzner, C.; van der Spoel, D.; Lindahl, E. Gromacs 4: Algorithms for Highly Efficient, Load-Balanced, and Scalable Molecular Simulation. *Journal of Chemical Theory and Computation* **2008**, *4*, 435-447.

36. Darden, T.; York, D.; Pedersen, L. Particle Mesh Ewald: An N·Log(N) Method for Ewald Sums in Large Systems. *The Journal of Chemical Physics* **1993**, *98*, 10089-10092.
37. Hess, B.; Bekker, H.; Berendsen, H. J. C.; Fraaije, J. G. E. M. Lincs: A Linear Constraint Solver for Molecular Simulations. *Journal of Computational Chemistry* **1997**, *18*, 1463-1472.
38. WestGrid consortium. <http://www.westgrid.ca/> (accessed November 25, 2013).
39. Ranaivoson, F. M.; Gigant, B.; Berritt, S.; Joullie, M.; Knossow, M. Structural Plasticity of Tubulin Assembly Probed by Vinca-Domain Ligands. *Acta Crystallographica Section D* **2012**, *68*, 927-934.
40. *Flexx Protein-Ligand Docker User & Technical Reference*, version 2.1.3; BioSolveIT GmbH: St. Augustin, Germany, 2012.
41. Littauer, U. Z.; Giveon, D.; Thierauf, M.; Ginzburg, I.; Ponstingl, H. Common and Distinct Tubulin Binding Sites for Microtubule-Associated Proteins. *Proceedings of the National Academy of Sciences* **1986**, *83*, 7162-7166.
42. Kaarsholm, N. C.; Kolstrup, A. M.; Danielsen, S. E.; Holm, J.; Hansen, S. I. Ligand-Induced Conformation Change in Folate-Binding Protein. *Biochemical Journal* **1993**, *292*, 921-925.
43. Celej, M. S.; Montich, G. G.; Fidelio, G. D. Protein Stability Induced by Ligand Binding Correlates with Changes in Protein Flexibility. *Protein Science* **2003**, *12*, 1496-1506.

44. Feeney, J.; Birdsall, B.; Kovalevskaya, N. V.; Smurnyy, Y. D.; Navarro Peran, E. M.; Polshakov, V. I. Nmr Structures of Apo L. Casei Dihydrofolate Reductase and Its Complexes with Trimethoprim and Nadph: Contributions to Positive Cooperative Binding from Ligand-Induced Refolding, Conformational Changes, and Interligand Hydrophobic Interactions. *Biochemistry* **2011**, *50*, 3609-3620.
45. Nogales, E.; Downing, K. H.; Amos, L. A.; Löwe, J. Tubulin and Ftsz Form a Distinct Family of Gtpases. *Nature Structural Biology* **1998**, *5*, 451-458.
46. David-Pfeuty, T.; Simon, C.; Pantaloni, D. Effect of Antimitotic Drugs on Tubulin Gtpase Activity and Self-Assembly. *Journal of Biological Chemistry* **1979**, *254*, 11696-702.
47. Keskin, O.; Durell, S. R.; Bahar, I.; Jernigan, R. L.; Covell, D. G. Relating Molecular Flexibility to Function: A Case Study of Tubulin. *Biophysical Journal* **2002**, *83*, 663-680.
48. Eyal, E.; Najmanovich, R.; McConkey, B. J.; Edelman, M.; Sobolev, V. Importance of Solvent Accessibility and Contact Surfaces in Modeling Side-Chain Conformations in Proteins. *Journal of Computational Chemistry* **2004**, *25*, 712-724.
49. Ravelli, R. B. G.; Gigant, B.; Curmi, P. A.; Jourdain, I.; Lachkar, S.; Sobel, A.; Knossow, M. Insight into Tubulin Regulation from a Complex with Colchicine and a Stathmin-Like Domain. *Nature* **2004**, *428*, 198-202.
50. Peng, L. X.; Hsu, M. T.; Bonomi, M.; Agard, D. A.; Jacobson, M. P. The Free Energy Profile of Tubulin Straight-Bent Conformational Changes, with

Implications for Microtubule Assembly and Drug Discovery. *PLoS Computational Biology* **2014**, *10*, e1003464.

51. Kis, A.; Kasas, S.; Kulik, A. J.; Catsicas, S.; Forró, L. Temperature-Dependent Elasticity of Microtubules. *Langmuir* **2008**, *24*, 6176-6181.

CHAPTER 3

Interactions of Vinblastine with Single-Walled Carbon Nanotubes*

3.1 Introduction

Carbon nanotubes (CNTs) have been extensively studied in the last 25 years. They have shown tremendous applications in multiple disciplines, including composite material, microelectronics, energy storage, sensors, biomedicine and imaging.¹⁻³ The medical applications of CNTs are especially inspiring for their prospective contribution to medicine. CNT-based carriers tailored for drug delivery have been extensively investigated and have shown promising outcomes.⁴⁻⁵ In general, nanoparticles are good vehicles for drug delivery as they can bind with drugs either by covalent conjugation or non-covalent absorption through π - π stacking⁶, hydrophobic effects⁷, or electrostatic interactions⁸. CNTs can bind drug molecules, protect them from degradation, transport them to cells and enter cells via endocytosis mechanism depending on the surface chemistry and dimensions of CNTs as well as cell types.⁹⁻¹¹ They can accumulate in

* This chapter was based on “Molecular Dynamics Studies for Optimization of Noncovalent Loading of Vinblastine on Single-Walled Carbon Nanotube” Li, Z.; Tozer, T. & Alisaraie, L., *The Journal of Physical Chemistry C* **2016**, 120, 4061-4070. Used with permission.

tumor tissues due to the enhanced permeability and retention (EPR) effect. Modified or functionalized CNTs, as carriers, are particularly useful as they are less toxic than non-functionalized CNTs¹² and have higher solubility¹³.

Liu *et al.* compared the binding energy and drug release rate of the non-covalently loading doxorubicin (DOX) on poly(ethylene glycol) (PEG) functionalized SWNTs of ~ 200 nm in length with two diameters: ~ 1.3 and ~ 1.9 nm. They found that DOX on the larger tube had a higher affinity and was released with a slower rate due to the stronger π -stacking with the larger tube.¹⁴ The same research group also functionalized SWNTs with phospholipids conjugated to branched PEG chains, and loaded paclitaxel (PTX) onto the carrier via cleavable ester bonds linking to the termini of PEG. An *in vitro* toxicity test on murine breast cancer 4T1 cells showed that the toxicity of SWNT-PTX was similar to clinical taxol and PEGylated PTX. The CNT-based delivery of PTX increased the blood circulation time much longer than the circulation time of taxol and PEGylated PTX, resulting in the high tumor accumulation through EPR effect. The high uptake of SWNT-PTX significantly reduced the dose required for the desired efficacy, which in turn reduced toxic effects to normal cells. Based on the 4T1 breast cancer mouse model, SWNT-PTX had high efficiency in inhibiting proliferation and inducing apoptosis of tumor cells. The *in vivo* release of PTX was through the cleavage of ester bond by carboxylesterases, and the drugs and carriers were eliminated by the reticuloendothelial system.¹⁵ Kang *et al.* tested the cell response to SWNTs with the diameter of 1-3 nm with two different length ranges of 50-100 nm and 100-200 nm. The cellular uptake of short (less than 50 nm) SWNTs was through energy-independent insertion and diffusion.

SWNTs of 50-100 and 100-200 nm in length internalized cells through the endocytosis pathway. Folate conjugated functionalized SWNTs significantly improved the selectivity and efficiency of penetration into human hepatocellular carcinoma (human liver tumor cell line, commonly known as Hep G2) cells which over expressed folate receptors. On the other hand, the high uptake led to the enhanced cytotoxicity. SWNTs of 100-200 nm mainly distributed in cytoplasm, SWNTs of 50-100 nm could even internalize in the cell nucleus. They suggested that the appropriate length of SWNTs for targeted drug delivery purpose was around 200 nm.¹⁶

Compared to the abundant experimental studies on CNT-based drug delivery, only a few modelling studies related to the interactions between CNT and drug molecules have been reported. Hilder and Hill established models to calculate the suction energy of CNT for the maximum uptake of cisplatin, PTX and DOX, and to optimize the range of CNT radius for three individual drugs. But the model highly depended on the Lennard-Jones (LJ) potential, without considering the electrostatic potential and solvent effects.¹⁷⁻¹⁸ SWNT-based *in vitro* or *in silico* delivery of Vinblastine (VLB), a prominent anti-mitotic drug used as widely as PTX and DOX for cancer treatment,¹⁹ has yet to be studied. Only one computational study by Mollaamin *et al.* reported comparisons of VLB–CNT stabilized energies mainly by quantum mechanics calculations for energy and geometry optimizations.²⁰ The lack of thorough studies on the CNT-based delivery of VLB motivated us to explore the interactions of VLB with CNTs under different loading conditions and to investigate the influence of temperature change, functionalization and chirality of CNT on VLB–CNT interactions.

Molecular dynamics (MD) simulation, a powerful and accurate computational technique, has been widely used to study the interactions of CNTs with biomolecules, polymers and drug molecules. For example, researchers have utilized MD simulations to study CNT-DNA interactions²¹, the wrapping of polyethylene on nanotube sidewall²², and the heat-driven drug release of the encapsulated ciprofloxacin²³. As a continuation of our earlier studies on microtubules²⁴⁻²⁵, we investigated the chemo- and thermo-induced depolymerizing effects on $\alpha\beta$ -tubulin heterodimer through MD simulations. Three systems were designed to compare the conformational changes of VLB-bound heterodimer at 300 K, apo-heterodimer at 277 K and apo-heterodimer at 300 K. The effects of VLB and low temperature were thoroughly studied from several perspectives, including conformational changes, structural stability as well as lateral and longitudinal contacts. We have found the thermo-effect is in line with the chemo-effect: they both triggered conformational changes resulting in the depolymerization of microtubules; furthermore, VLB displays stronger influence to disassemble microtubules than low temperature based on the overall effects on tubulin dimer structure. The studies foreshadowed the feasibility of a combinational therapy involving both therapeutics and temperature control for cancer treatment.²⁶

The work presented in this chapter has made a step forward in the study of drug-carrier interactions under different conditions. MD simulations of VLB-SWNT non-covalent binding at 277 K and 300 K were performed to examine the effect of temperature on the CNT-based delivery of VLB. Additionally, our studies have provided in-depth

knowledge on drug–carrier interactions through the discussion of loading positions, interaction energy, loading capacities, CNT functionalization and chirality effects.

3.2 Materials and Methods

Considering the size of the VLB molecule (**Appendix B** Figure B1), the armchair (16, 16) SWNT, ~50 Å in length and 21.7 Å in diameter, was used as the carrier for the delivery of VLB, unless otherwise stated. SWNTs were functionalized by esterification²⁷, through which four methyl ester groups covalently adjoined four carbon atoms at each end of the tube. (**Appendix B** Figure B2)

Systems consisted of one CNT carrier and one to three VLB molecules attached to the exterior wall or encapsulated within the CNT. The CNT carrier is either non-functionalized or functionalized, with a CNT of armchair, chiral or zigzag structure. (**Table 3.1, Appendix B** Figure B3 & Table B1, B2)

Table 3.1 Composition of various sets of CNT–VLB simulation systems.

Systems	VLB molecules loaded		CNT Structure
	Amount	Location	
SWNT-1VLB_Out	1	Outside	Armchair (16, 16)
fSWNT-1VLB_Out	1	Outside	Armchair (16, 16)
SWNT-1VLB_In	1	Inside	Armchair (16, 16)
fSWNT-1VLB_In	1	Inside	Armchair (16, 16)
SWNT-2VLB_Out	2	Both outside	Armchair (16, 16)
fSWNT-2VLB_Out	2	Both outside	Armchair (16, 16)
fArmchair-3VLB	3	2 Outside, 1 Inside	Armchair (16, 16)
fChiral-3VLB	3	2 Outside, 1 Inside	Chiral (17, 15)
fZigzag-3VLB	3	2 Outside, 1 Inside	Zigzag (28, 0)

The optimized potentials for liquid simulations all-atom (OPLS-AA) force field²⁸⁻³¹ was utilized to perform simulations with *Gromacs* (version 4.5.5)³²⁻³³. The topology of VLB generated by ATB was based on Gromos96 force field 53A6,³⁴ therefore the MKTOP³⁵ was used to generate OPLS-AA topology for VLB. Partial atomic charge refinement was performed according to the chemical environment in VLB molecule and the corresponding atom type defined in OPLS-AA force field library. After charge refinement, the net charge of VLB was rounded to +1 due to the mono-protonation state.²⁶ The refinement for bond and angle adapted by MKTOP program was implemented similarly as for the charge. The unrecognizable dihedrals in VLB were assigned by searching the closest dihedral type in terms of chemical environment

available in the OPLS-AA force field library and applying it to the matched dihedral type in VLB molecule.

SWNT structures were generated by *Nanotube Modeler* (version 1.7.3, JCrystalSoft).³⁶ The charge for carbon atoms of the pristine SWNT was zero based on the atom type defined for naphthalene in OPLS-AA force field. The bond type for carbon atoms in CNT was defined in the same way as in tryptophan, tyrosine and phenylalanine, the angle type was defined as a phenylalanine angle and the dihedral angle type as an aromatic ring dihedral angle.²⁹⁻³⁰ (**Table 3.2**)

The parameters for simulating CNT in this work agreed well with parameters used elsewhere.³⁷⁻³⁸ For the functionalized SWNTs (fSWNTs), the partial atomic charge for functional groups were assigned based on the atom type defined in OPLS-AA force field and adjusted to ensure the net neutral charge for the whole functional group. The parameters for angles and dihedrals in esterified SWNTs were undefined in the OPLS-AA force field library. Therefore, parametrization was performed by searching the closest angle and dihedral types in terms of chemical environment available in the OPLS-AA force field parameters and applying them to fSWNTs.

Table 3.2 Parameters for simulating CNT using OPLS-AA force field. (k^b , k^θ and k_ϕ are force constants of stretching, bending and torsional potentials. b_0 and θ_0 are reference geometry parameters. ϵ is the well depth, and σ is the separation distance at which the inter-particle potential is zero.)

Items	Parameters	
Bond	$k^b = 392.4592 \text{ kJ mol}^{-1} \text{ \AA}^{-2}$	$b_0 = 1.4 \text{ \AA}$
Angle	$k^\theta = 527.184 \text{ kJ mol}^{-1} \text{ rad}^{-2}$	$\theta_0 = 120^\circ$
Dihedral	$k_\phi = 30.334 \text{ kJ mol}^{-1}$	
Lennard-Jones	$\epsilon = 0.29288 \text{ kJ mol}^{-1}$	$\sigma = 3.55 \text{ \AA}$

The non-bonded interactions, including van der Waals (vdW) interactions and electrostatic interactions, were modelled by LJ potential and Coulomb potential, respectively.³⁴ A cut-off distance of 1.0 nm was assigned for both Lennard-Jones and electrostatic interactions. The calculation of electrostatic forces and energies was carried out based on the Particle Mesh Ewald algorithm³⁹. The LINear Constraint Solver (LINCS) algorithm⁴⁰ was applied to constrain all bond lengths. The temperature was set to 277 K or 300 K with the temperature coupling of 0.1 ps. The time constant for pressure coupling was set to 1.0 ps with compressibility of $4.5\text{e-}5 \text{ bar}^{-1}$.

Each simulation system was first energy minimized using the steepest descent algorithm and then a 4-ns all-bonds position restraint was applied. The MD simulations were implemented to gradually release constraints. The MD simulations for SWNT-1VLB_In systems and fSWNT-1VLB_In systems were run for 350 ns. The MD

simulations for the two systems of fArmchair-3VLB at 300 K and fZigzag-3VLB at 277 K were run for a total of 350 ns. Other simulations were run for 180 ns. All the simulations were performed on WestGrid high performance computer clusters of Compute Canada.⁴¹ (Table 3.1)

3.3 Results and Discussions

3.3.1 CNT-1VLB systems

3.3.1.1 vdW force between VLB and SWNT

For non-functionalized SWNT carrier, after convergence at ~ 150 ns, the stable LJ interactions of SWNT-1VLB_Out were -101.09 kJ/mol at 300 K and -119.65 kJ/mol at 277 K. For fSWNT carrier, after convergence at ~ 150 ns, the stabilized LJ interactions of fSWNT-1VLB_Out were -121.80 kJ/mol at 300 K and -85.17 kJ/mol at 277 K. (Figure 3.1)

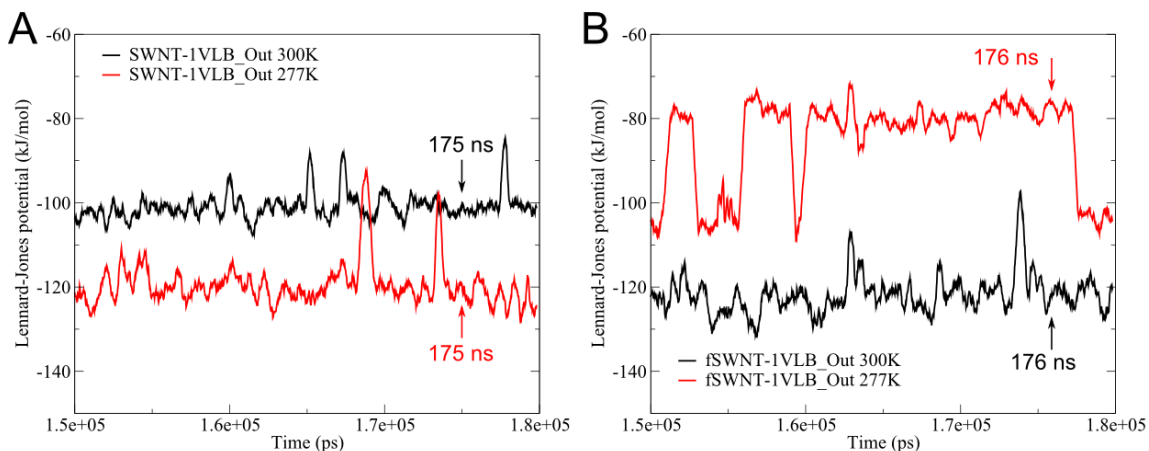


Figure 3.1 The LJ interactions between CNT and VLB for (A) SWNT-1VLB_Out and (B) fSWNT-1VLB_Out at 300 K (black) and 277 K (red), respectively. Arrow indicates one of the time frames corresponding to stable LJ energy.

Before functionalization, VLB–CNT interactions were 18.6 kJ/mol stronger at 277 K than at room temperature. After functionalization, the trend was reversed: VLB–CNT interactions were 36.6 kJ/mol stronger at room temperature than at 277 K. Therefore, functionalization strengthened the SWNT–VLB interactions at room temperature but greatly weakened the interactions at 277 K.

3.3.1.2 VLB orientations with respect to SWNT

Temperature dramatically affected the level of stable interaction energy, for both non-functionalized and functionalized SWNT carriers. The non-hydrogen atoms of vindoline and catharanthine components of VLB were numbered in two sequences⁴² to monitor the orientation of VLB with respect to SWNT surface. (**Appendix B** Figure B4)

VLB had the exterior-bound position parallel to the CNT surface, wherein both the vindoline and catharanthine sub-parts were ~ 3.5 Å away from the nearest CNT sidewall; or the exterior-bound position nonparallel to the CNT surface, wherein the vindoline sub-part was ~ 3.5 Å away from the nearest CNT sidewall but the catharanthine sub-part was ~ 7 Å away. When VLB had the parallel exterior-bound position, the co-planar structure of the aromatic ring and its adjacent pyrrole ring in vindoline flexibly changed the angle with SWNT surface such that the methyl ether group bound to C16 and the methyl group bound to N1 could orient either downward or upward to the SWNT surface. When VLB had the nonparallel exterior-bound position, the co-planar structure was no longer partially parallel to CNT sidewall but nearly perpendicular to the sidewall, which elevated the catharanthine part of VLB. (**Figure 3.2**)

The distances between the CNT sidewall and atoms C6, C8, C26, O31, C8', as well as O24' in VLB were tracked over the entire simulation. (**Appendix C** Figure C1)

The similar parallel exterior-bound position in which C16 and N1 were facing away from the CNT shown in SWNT-1VLB_Out at 277 K and fSWNT-1VLB_Out at 300 K, resulting in a similar stable level of LJ interactions nearly -120 kJ/mol. However, the parallel exterior-bound position in which C16 and N1 facing downward the CNT shown in SWNT-1VLB_Out at 300 K, almost a flip-over pose of -119.65 kJ/mol parallel exterior-bound position, reduced LJ interactions to -101.09 kJ/mol. The nonparallel exterior-bound position shown in fSWNT-1VLB_Out at 277 K further reduced LJ interactions to -85.17 kJ/mol. (**Figure 3.1 & 3.2**)

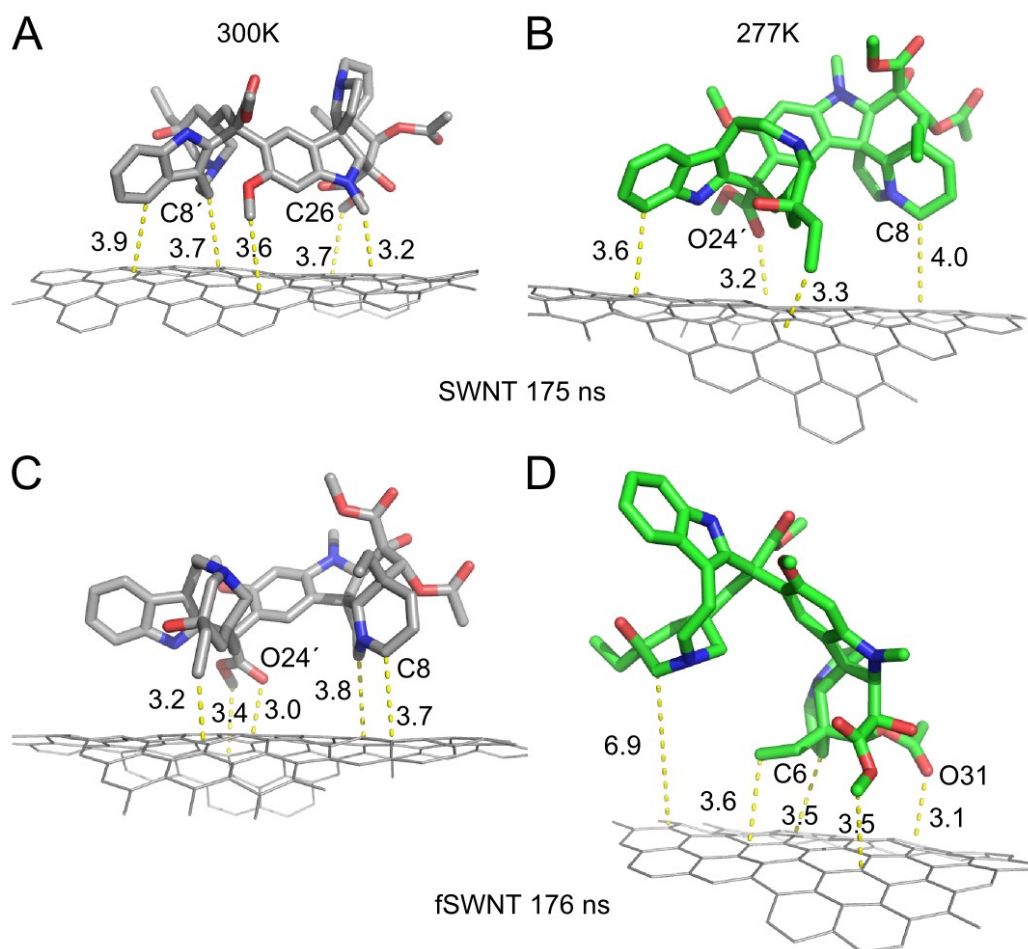


Figure 3.2 Stable VLB orientations with respect to the CNT sidewall for SWNT-1VLB system at (A) 300 K and (B) 277 K, and for fSWNT-1VLB system at (C) 300 K and (D) 277 K. Dashed lines indicate the nearest distance to the sidewall in Å.

3.3.1.3 Encapsulation

The stable LJ interactions for SWNT-1VLB_In at 300 K had energy levels of -239.66 kJ/mol at 300 K and -179.33 kJ/mol at 277 K after convergence at ~ 300 ns. With functionalization, the LJ interactions for fSWNT-1VLB_In at 300 K and 277 K were stabilized at -206.09 kJ/mol and -206.23 kJ/mol, respectively. Functionalization reduced

the average stable LJ interactions at 300 K by 33.6 kJ/mol. Nevertheless, the average interactions between fSWNT and the encapsulated VLB at low temperature were 26.9 kJ/mol stronger than those between non-functionalized SWNT and the encapsulated VLB.

(Figure 3.3)

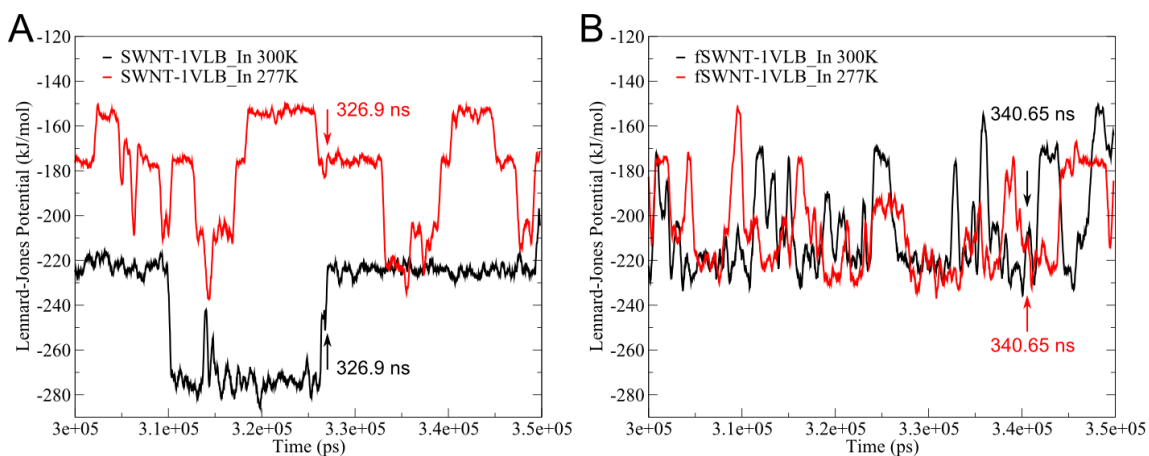


Figure 3.3 The LJ interactions between CNT and VLB at (A) SWNT-1VLB_In and (B) fSWNT-1VLB_In under 300 K (black) and 277 K (red), respectively. Arrow indicates one of the time frames corresponding to stable LJ energy.

For non-functionalized SWNT carriers, the parallel encapsulated-bound position of VLB at 300 K led to stronger interactions with SWNT sidewall than the nonparallel encapsulated-bound position at 277 K. For fSWNT carriers, VLB had the parallel encapsulated-bound position at both 300 K and 277 K, leading to the almost equal strength of VLB–CNT interactions. **(Figure 3.4)**

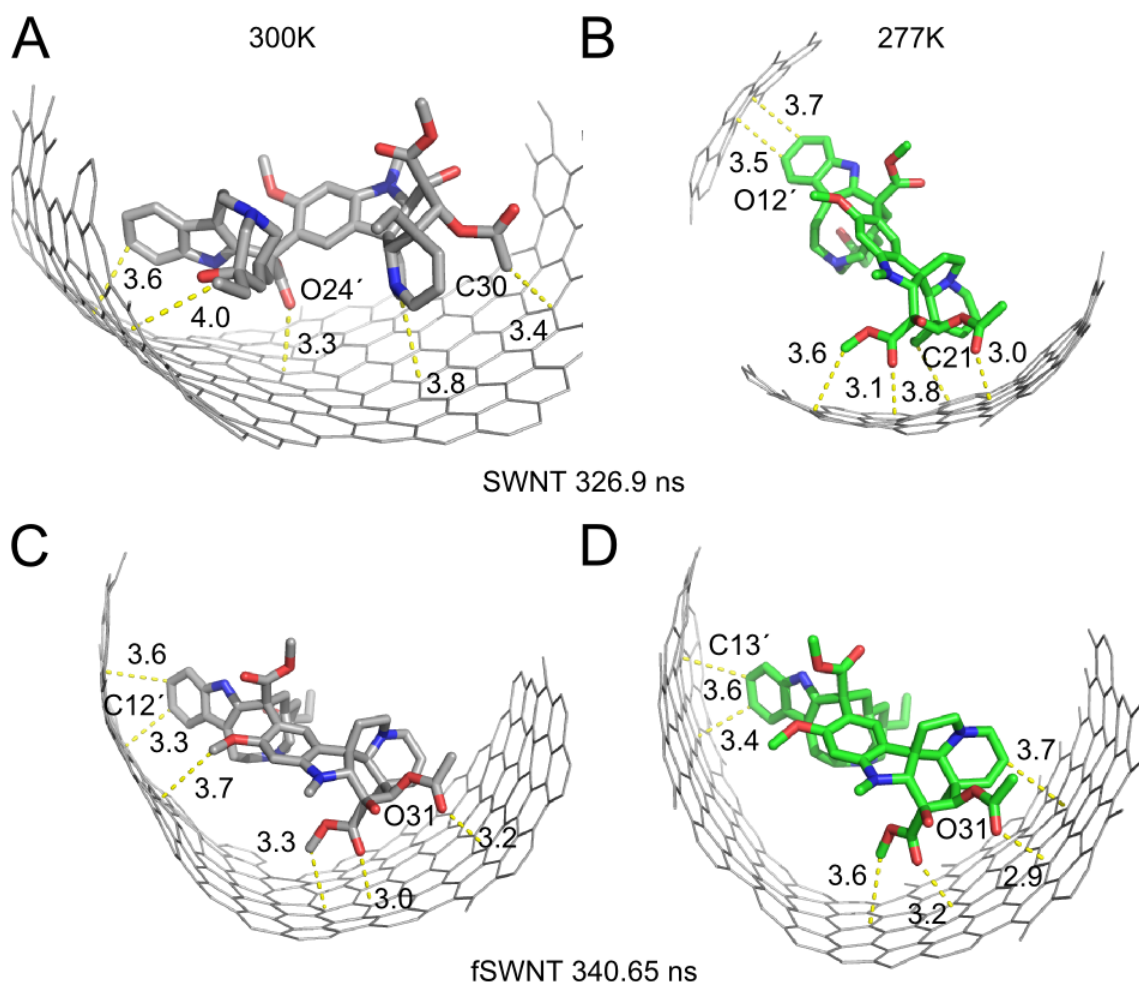


Figure 3.4 Stable orientations of encapsulated VLB with respect to CNT sidewall for SWNT-1VLB at (A) 300 K and (B) 277 K, and for fSWNT-1VLB at (C) 300 K and (D) 277 K. Dashed lines indicate the nearest distance to the sidewall in Å.

Compared with the scenario that VLB was attached outside, the VLB–CNT interactions were much stronger when VLB was encapsulated. The strong encapsulated VLB–CNT interactions resulted from the large exposed surface area to VLB when it was encapsulated in the tube. The minimum distances between the CNT sidewall and VLB

atoms C21, C30, O31, C12', C13' as well as O24' were tracked over the simulation. (Appendix C Figure C2)

3.3.2 CNT-2VLB systems

3.3.2.1 vdW force between VLB and SWNT

An additional VLB was loaded onto the carrier in the CNT-2VLB systems. When the SWNT carrier was non-functionalized, the average LJ interactions for VLB1 and VLB2 of SWNT-2VLB at 300 K were -83.91 kJ/mol and -100.62 kJ/mol, respectively, after convergence at ~150 ns. The stable LJ interactions for VLB1 and VLB2 of SWNT-2VLB system at 277 K were -117.65 kJ/mol and -84.08 kJ/mol, respectively. (Figure 3.5A-B)

For the functionalized carrier after convergence at ~ 150 ns, the average LJ interactions for VLB1 and VLB2 of fSWNT-2VLB at 300 K were -81.07 kJ/mol and -85.59 kJ/mol, respectively; and -81.85 kJ/mol and -80.96 kJ/mol, respectively, at 277 K. (Figure 3.5C-D)

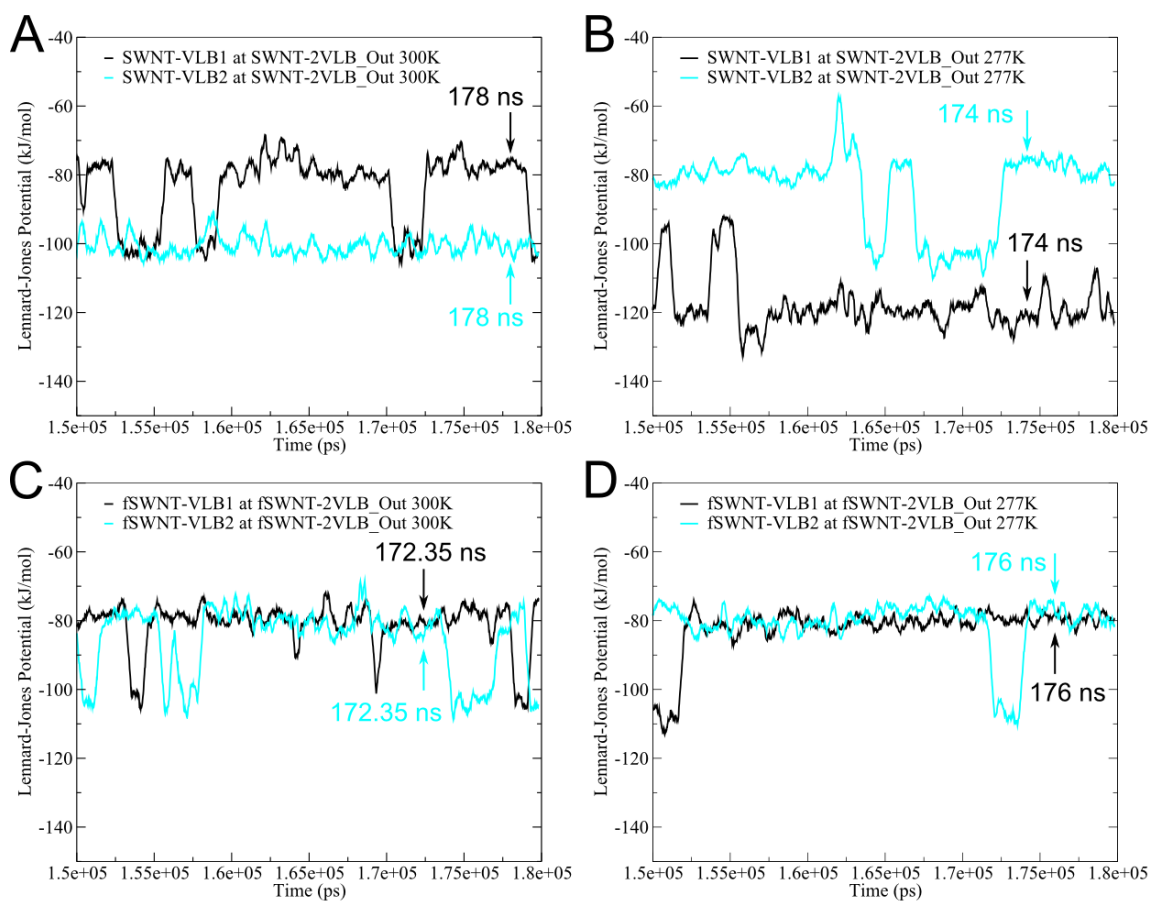


Figure 3.5 The LJ interactions between CNT and VLBs for SWNT-2VLB under (A) 300 K and (B) 277 K as well as for fSWNT-2VLB under (C) 300 K and (D) 277 K, respectively. Arrow indicates one of the time frames corresponding to stable LJ energy. VLB1 is in black and VLB2 is in cyan.

3.3.2.2 VLB orientations with respect to SWNT

The orientations corresponding to different energy levels, approximately -80 kJ/mol, -100 kJ/mol and -120 kJ/mol, were consistent with those shown in SWNT-1VLB_Out. The non-parallel exterior-bound position corresponded to LJ interaction of \sim -80 kJ/mol, as VLB1 in SWNT-2VLB at 300 K and VLB2 in SWNT-2VLB at 277 K. The parallel

exterior-bound position with C16 and N1 facing away from the CNT sidewall corresponded to LJ interaction of -117.65 kJ/mol, as VLB1 in SWNT-2VLB at 277 K; the parallel exterior-bound position with C16 and N1 facing toward the CNT sidewall corresponded to -100.62 kJ/mol, as VLB2 in SWNT-2VLB system at 300 K. (**Figure 3.6**)

The distances between the CNT sidewall and VLB atoms C26, O31, C5', N6', C11', C21' as well as O24' were tracked over the entire simulation time. (**Appendix D** Figure D1)

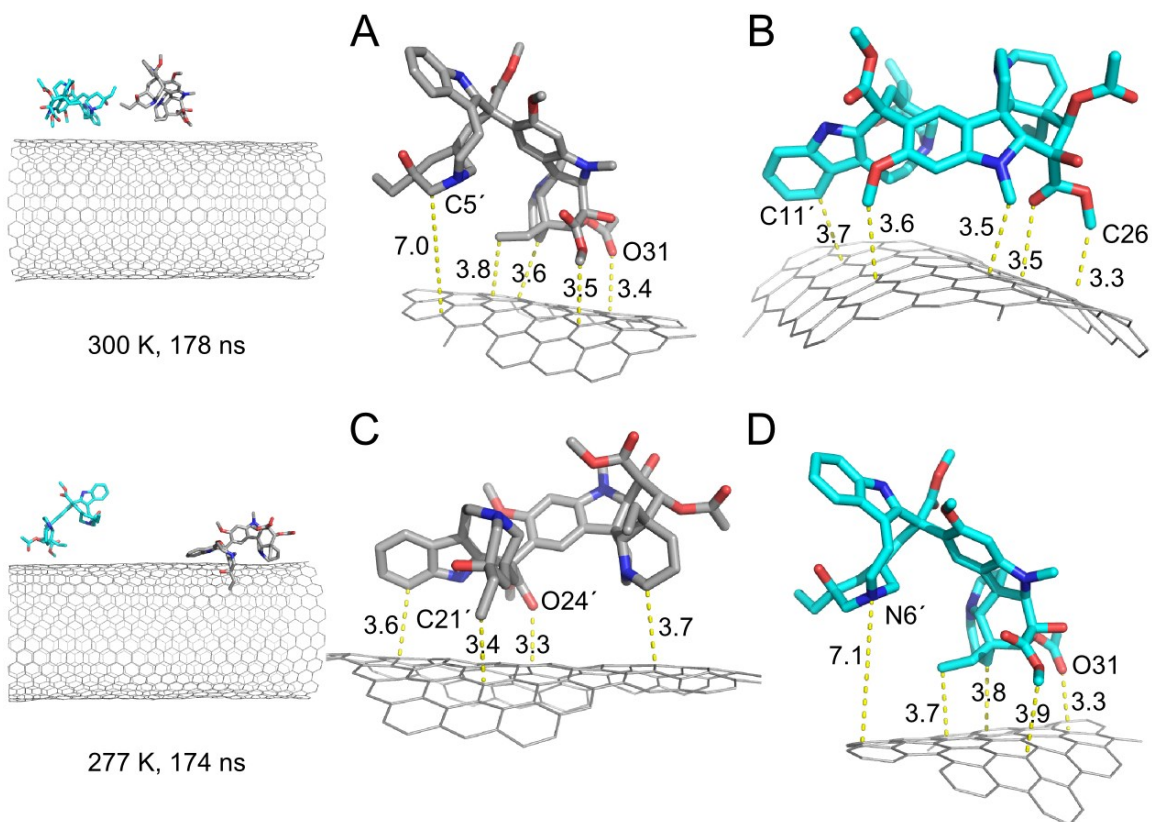


Figure 3.6 Stable orientations at SWNT-2VLB of (A) VLB1 and (B) VLB2 at 300 K as well as (C) VLB1 and (D) VLB2 at 277 K with respect to SWNT sidewall. Dashed lines indicate the nearest distance to the sidewall in Å. VLB1 is in gray and VLB2 is in cyan.

All of the VLB molecules in fSWNT-2VLB had the nonparallel exterior-bound position at both temperatures. (**Appendix D** Figure D2)

The distances between the CNT sidewall and VLB atoms C6, O24, O31 as well as N6' were tracked over the simulation. (**Appendix D** Figure D3)

When the temperature was changed from 300 K to 277 K for the non-functionalized system, the VLB1–CNT interactions were strengthened by 33.7 kJ/mol while the VLB2–CNT interactions were weakened by 16.5 kJ/mol. However, the decrease of temperature did not affect the VLB–CNT interactions of the functionalized system. If the two VLB molecules were treated as indistinguishable, functionalization showed no effect to one of the VLB but weakened the interactions for the other VLB. The functionalization on CNT termini was not expected to affect the interactions of VLB with CNT sidewall. We elucidated that the undermined interactions were due to the loading capacity of the SWNT used. A CNT with the length of 50 Å may not be long enough to accommodate two dynamic VLB molecules with the dimension of 16 Å. The VLB–CNT interactions were weakened at both 300 K and 277 K, when an additional VLB was loaded onto the tube sidewall. (**Figure 3.1 & 3.5**)

3.3.2.3 Inter-drug interactions

In addition to the LJ interactions between CNT and VLB, the LJ and electrostatic interactions between the two VLB molecules loaded on SWNT-2VLB were also investigated. At 300 K, the maximum inter-drug LJ interactions were -25.5 kJ/mol and the maximum inter-drug electrostatic interactions were -9.8 kJ/mol for attractions and

+4.8 kJ/mol for repulsions. At 277 K, the maximum inter-drug LJ interactions were -35.9 kJ/mol and the maximum inter-drug electrostatic interactions were -14.2 kJ/mol for attractions and +11.2 kJ/mol for repulsions. The inter-drug interactions existed only when the center-of-mass (COM) distance between VLB1 and VLB2 was less than 2 nm. The interactions vanished at the COM distance greater than 2 nm. (**Appendix D** Figure D4)

For fSWNT-2VLB systems at 300 K, the maximum inter-drug LJ interactions were -24.1 kJ/mol and the maximum inter-drug electrostatic interactions were -5.8 kJ/mol for attractions and +6.7 kJ/mol for repulsions. At 277 K, the maximum inter-drug LJ interactions were -29.9 kJ/mol and the maximum inter-drug electrostatic interactions were -7.0 kJ/mol for attractions and +7.5 kJ/mol for repulsions. The inter-drug interactions existed only when the COM distance between VLB1 and VLB2 was below 2 nm. The LJ and Coulomb interactions reached the maximum approximately at the time corresponding to the minimum COM distance. (**Appendix D** Figure D5)

3.3.3 CNT-3VLB systems

The CNT-3VLB systems include three sub-systems: fArmchair-3VLB, fChiral-3VLB and fZigzag-3VLB; each sub-system was studied at 277 K and 300 K.

3.3.3.1 fArmchair-3VLB

3.3.3.1.1 vdW force between VLB and SWNT

For the functionalized armchair SWNT carrier, the stable LJ interactions for VLB1, VLB2 and VLB3 of fArmchair-3VLB at 300 K were -116.72 kJ/mol, -199.13 kJ/mol and -230.01 kJ/mol, respectively, after convergence at ~150 ns. At 277 K, the stable LJ

interactions for VLB1, VLB2 and VLB3 were -121.98 kJ/mol, -203.37 kJ/mol and -101.77 kJ/mol, respectively, after convergence at ~150 ns. (**Figure 3.7**)

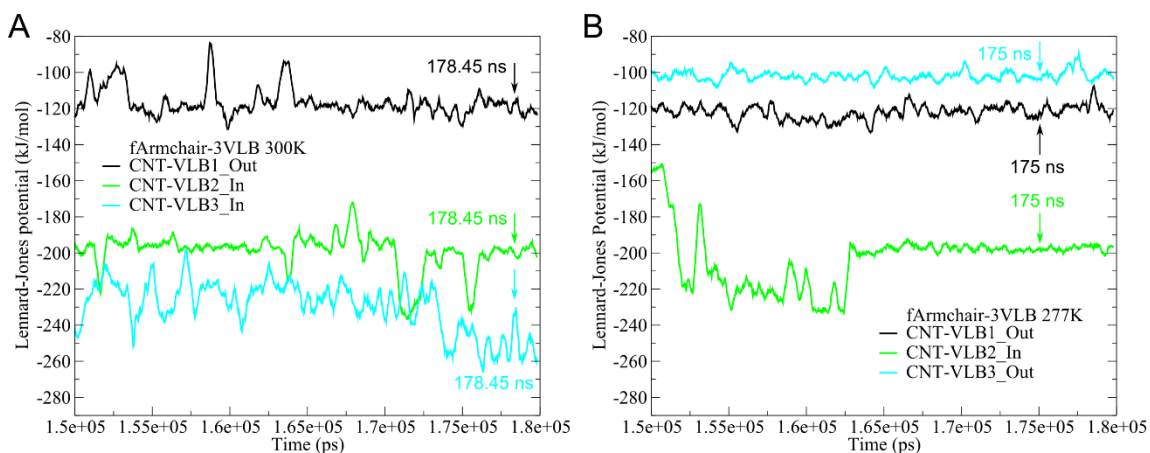


Figure 3.7 The LJ interactions between CNT and VLBs at fArmchair-3VLB under (A) 300 K and (B) 277 K, respectively. Arrow indicates one of the time frames corresponding to stable LJ energy. VLB1 is in black, VLB2 is in green and VLB3 is in cyan.

3.3.3.1.2 VLB orientations with respect to fArmchair SWNT

At 300 K, VLB1, initially set outside the tube, continuously moved along the exterior of the tube during the simulation in the parallel exterior-bound position; VLB2, initially encapsulated in the tube, continuously moved in the tube during the entire simulation time; VLB3, initially set outside the tube, entered the tube shortly after the start of the simulation (~1 ns) and remained encapsulated during the rest of the simulation time. (**Figure 3.8**)

The distances between the CNT sidewall and VLB atoms C7, C8, C22, C13' as well as C21' were tracked over the simulation. (**Appendix E** Figure E1)

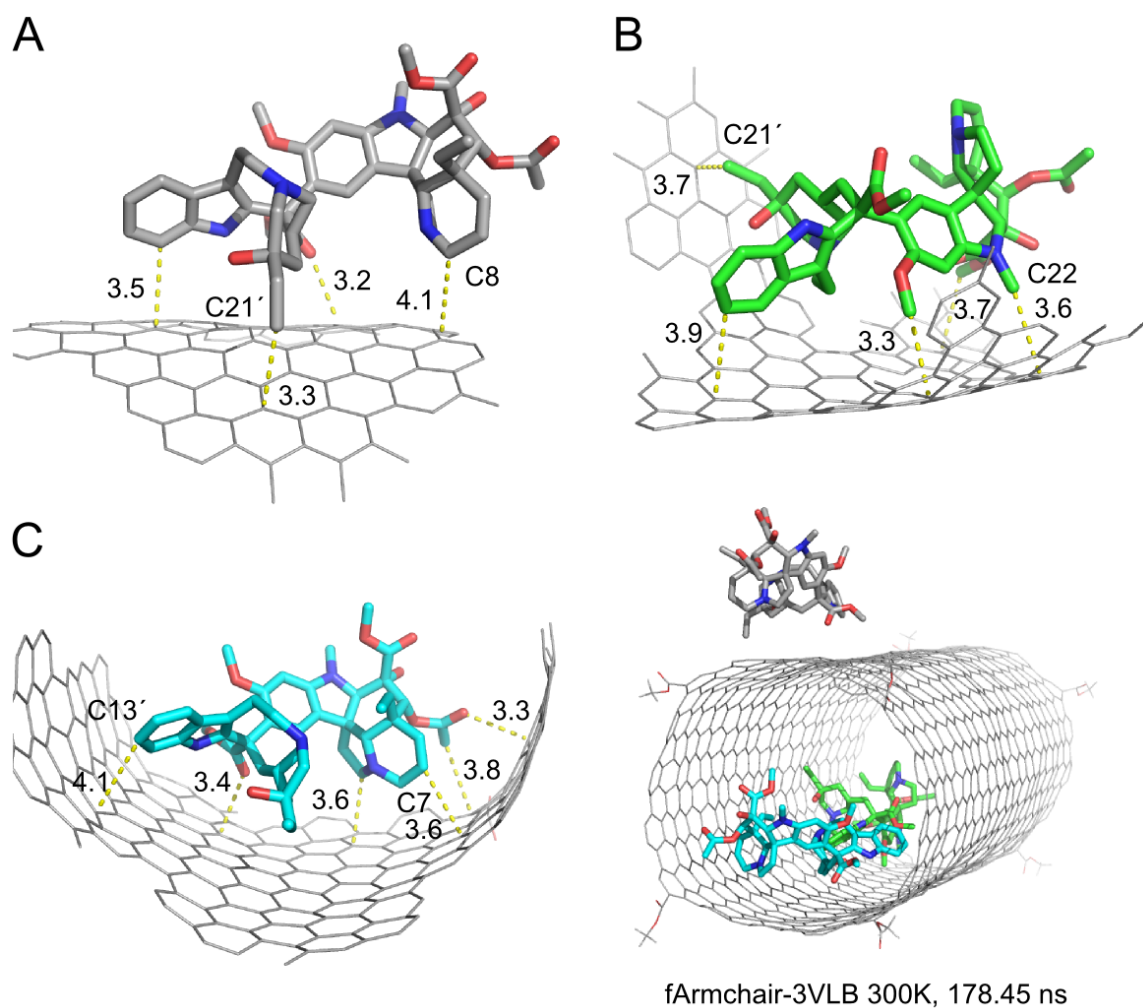


Figure 3.8 Stable orientations of (A) VLB1, (B) VLB2 and (C) VLB3 at 300 K with respect to fArmchair SWNT. Dashed lines indicate the nearest distance to the sidewall in Å. VLB1 is in gray, VLB2 is in green and VLB3 is in cyan.

In fArmchair-3VLB at 300 K, VLB3 entered the tube from outside; the noteworthy phenomenon did not occur in the CNT-1VLB systems or the CNT-2VLB systems. The key factors that likely triggered this event were LJ and Coulomb interactions between fArmchair SWNT and VLB3. The entering process, from ~ 0.4 ns to ~ 1 ns, was

accompanied by a dramatic increase in LJ interactions. The strong LJ interactions played a key role in encapsulating the VLB3 molecule, which was in line with the studies on DNA encapsulation by SWNT.⁴³ The electrostatic attractions between the methyl ester groups and VLB3, although weak (~ 3.5 kJ/mol), could be significant in directing and pulling VLB3 into the tube. (**Figure 3.9**, **Appendix E** Figure E2)

VLB2, the already encapsulated drug molecule, did not appear to play a role in the encapsulation of VLB3. This was because there were not any inter-drug interactions between VLB2 and VLB3 as the COM distance was above the 2-nm threshold during the entering process of VLB3.

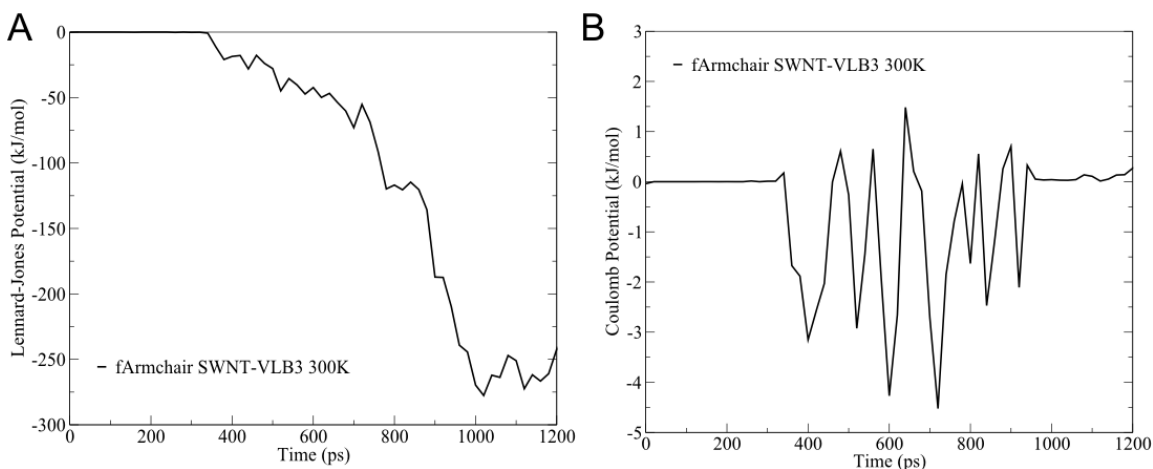


Figure 3.9 (A) LJ and (B) Coulomb interactions between fArmchair SWNT and VLB3 in the process of VLB3 entering the tube.

At 277 K, VLB1 and VLB3, initially set outside the tube, continuously moved along the exterior of the tube during the simulation and had the parallel exterior-bound position;

VLB2, initially encapsulated in the tube, continuously moved inside the tube during the entire simulation time. (**Appendix E** Figure E3)

The distances between the CNT sidewall and VLB atoms C8, O24, C33, C8' as well as C21' were tracked over the simulation. (**Appendix E** Figure E4)

3.3.3.1.3 Intermolecular drug interactions

When VLB molecules distributed both outside and inside the tube, the CNT sidewall acted as a shield by greatly weakening the inter-drug LJ and electrostatic interactions between the attached VLB and the encapsulated VLB. For fArmchair-3VLB at 300 K, both LJ and Coulomb interactions were significant for the two VLB molecules inside the tube. However, the interactions of VLB2 and VLB3 with VLB1 outside the tube were negligible. At 277 K, both LJ and Coulomb interactions were significant for the two VLB molecules VLB1 and VLB3 outside the tube, however, their interactions with VLB2 in the tube were negligible. (**Appendix E** Figure E5)

The shielding effect from CNT sidewall was further verified by the COM distance among the three VLB molecules. When the COM distance was below 2 nm, only both VLB molecules located either outside the tube or inside the tube would interact with each other. Even when two VLB molecules are close enough to each other, such as VLB1 outside ~1.5 nm from VLB2 inside at 277 K, no interactions were observed. Without the sidewall barrier, LJ and Coulomb interactions reached the maximum approximately at the same time as the minimum COM distance. (**Appendix E** Figure E6)

3.3.3.2 fChiral-3VLB

3.3.3.2.1 vdW force between VLB and SWNT

For functionalized chiral SWNT carrier, the stable LJ interactions for VLB1, VLB2 and VLB3 of fChiral-3VLB at 300 K were -83.79 kJ/mol, -204.56 kJ/mol and -116.28 kJ/mol, respectively, after convergence at ~ 150 ns. At 277 K, the stable LJ interactions for VLB1, VLB2 and VLB3 were -102.87 kJ/mol, -208.10 kJ/mol and -121.59 kJ/mol, respectively. The decrease of temperature made VLB1–CNT interactions stronger, but showed little effects on the encapsulated VLB2 and the attached VLB3. (**Figure 3.10**)

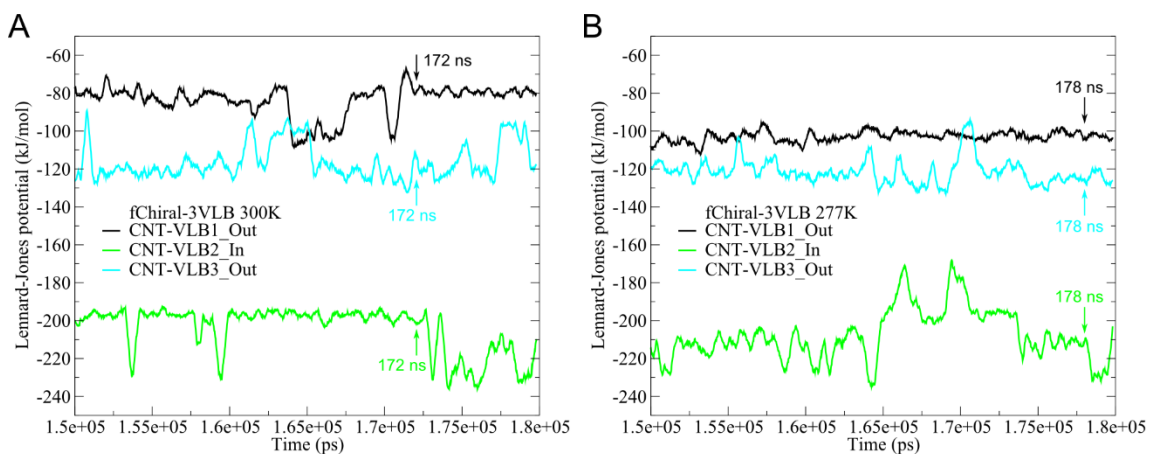


Figure 3.10 The LJ interactions between CNT and VLBs in fChiral-3VLB at (A) 300 K and (B) 277 K, respectively. Arrow indicates one of the time frames corresponding to stable LJ energy. VLB1 is in black, VLB2 is in green and VLB3 is in cyan.

3.3.3.2.2 VLB orientation with respect to fChiral SWNT

At 300 K, VLB1, initially attached to the exterior of the tube, continuously stayed outside during the entire simulation time and had the nonparallel exterior-bound position. VLB2,

initially encapsulated in the tube, continuously stayed in the tube during the entire simulation time. VLB3, initially attached outside the tube, continuously stayed outside and had the parallel exterior-bound position. (**Appendix E** Figure E7)

The distances between the CNT sidewall and VLB atoms C8, C26, O31, C5', C12' as well as O24' were tracked over the simulation. (**Appendix E** Figure E8)

At 277 K, VLB1 and VLB3, initially located outside the tube, continuously stayed outside during the simulation process and had parallel exterior-bound positions; VLB2, initially encapsulated in the tube, continuously moved inside the tube during the entire simulation time. (**Appendix E** Figure E9)

The distances between the CNT sidewall and VLB atoms O24, C33, C12', C14' as well as O24' were tracked over the simulation. (**Appendix E** Figure E10)

3.3.3.2.3 Inter-drug interactions

The shielding effect by CNT sidewall on both electrostatic and LJ interactions was also observed in fChiral-3VLB at 300 K and 277 K, LJ and Coulomb interactions were significant only for VLB1 and VLB3 both located outside the tube. (**Appendix E** Figure E11)

When the COM distance was within 2 nm, only VLB molecules located outside the tube interacted with each other. (**Appendix E** Figure E12)

3.3.3.3 fZigzag-3VLB systems

3.3.3.3.1 vdW force between VLB and SWNT

For functionalized zigzag SWNT carrier, the stable LJ interactions for VLB1, VLB2 and VLB3 of fZigzag-3VLB at 300 K were -100.44 kJ/mol, -211.06 kJ/mol and -120.87

kJ/mol, respectively, after convergence at ~ 150 ns. At 277 K, the stable LJ interactions for VLB1, VLB2 and VLB3 were -84.24 kJ/mol, -223.66 kJ/mol and -192.01 kJ/mol, respectively. The large increase of LJ interactions for VLB3 at 277 K system resulted from the encapsulation. (**Figure 3.11**)

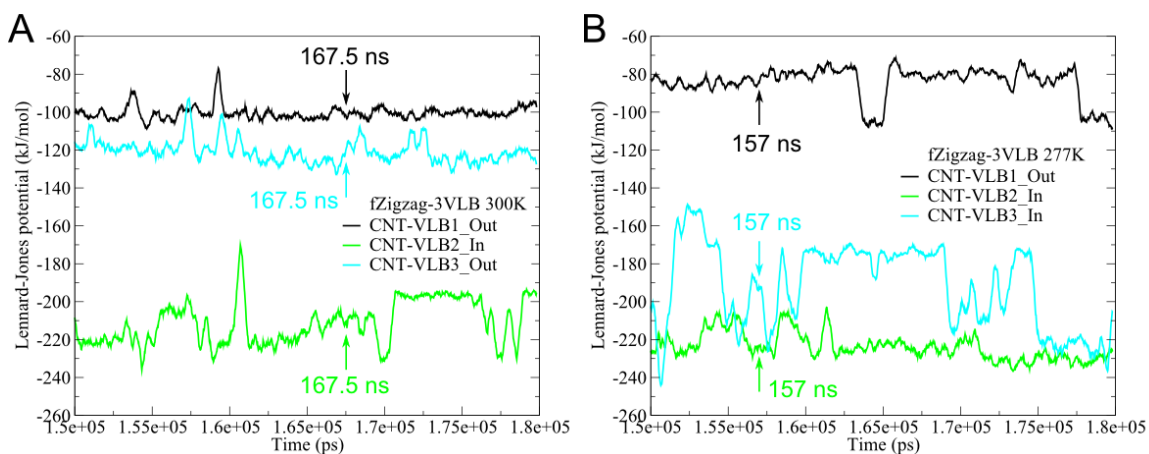


Figure 3.11 The LJ interactions between CNT and VLB molecules of fZigzag-3VLB at (A) 300 K and (B) 277 K, respectively. Arrow indicates one of the time frames corresponding to stable LJ energy.

3.3.3.3.2 VLB orientations with respect to fZigzag SWNT

At 300 K, VLB1 and VLB3, initially located outside the tube, continuously stayed outside and had the parallel exterior-bound position. VLB2, initially encapsulated in the tube, continuously moved inside the tube during the simulation. (**Appendix E** Figure E13)

The distances between the CNT sidewall and VLB atoms C8, O24, C33, C8', C21' as well as O24' were tracked over the simulation. (**Appendix E** Figure E14)

At 277 K, VLB1, initially located outside the tube, continuously moved outside and had the nonparallel exterior-bound position. VLB2, initially encapsulated in the tube, continuously moved inside the tube during the entire simulation time. VLB3, initially

located outside the tube, entered the tube at ~ 3 ns and remained encapsulated during the rest of the simulation time. (**Appendix E** Figure E15)

The distances between the CNT sidewall and VLB atoms C8, C21, C33, C5', C13' as well as O24' were tracked over the simulation. (**Appendix E** Figure E16)

3.3.3.3 Inter-drug interactions

The inter-drug interactions in fZigzag-3VLB were similar to those observed in the other CNT-3VLB systems. The encapsulation of VLB3, observed in fArmchair-3VLB at 300 K, also happened to the VLB3 of fZigzag-3VLB at 277 K. VLB3 entered the tube during ~ 1.5 ns to ~ 5.5 ns. The entering process was longer than that of the VLB3 of fArmchair-3VLB at 300 K. The key factors facilitating the encapsulation were LJ and Coulomb interactions between fZigzag SWNT and VLB3. VLB3 completely entered the tube at ~ 3.5 ns and remained at the end of the tube until ~ 6 ns before it moved further to the interior of the tube. (**Appendix E** Figure E17, E18)

Hilder and Hill deduced that the optimum SWNT radius to encapsulate paclitaxel and doxorubicin ranged from 9.13 to 12.68 Å and 8.86 to 10.51 Å, respectively, which were 18.26-25.36 Å and 17.72-21.02 Å in diameter, respectively.¹⁸ The CNT diameter used in this study (~ 21.8 Å) is in the optimized range of paclitaxel encapsulation and just slightly above the upper limit of doxorubicin entry. However, this diameter is clearly not ideal because VLB molecules can be encapsulated and trapped in the CNTs. The two VLB molecules, entered the tube in two independent systems, were trapped in the interior during the extended simulation up to 350 ns. (**Appendix E** Figure E19)

The encapsulation was irreversible due to the intensive interactions nearly twice as strong as that in the external attachment, consequently, encapsulation prevented the unloading of VLB. The irreversible encapsulation phenomenon observed in these investigations was consistent with studies of fullerene encapsulation through the open end of armchair (10, 10) SWNT reported by Berber and co-workers.⁴⁴ The remedy for removing the unloading hurdle caused by encapsulation lies in shrinking the tube diameter to block VLB entry so that all drug molecules are loaded to the exterior wall and delivered and unloaded to the target without being trapped inside the tube. The encapsulation that occurred in this study was quite rare, which is consistent with the findings by Berber *et al.*⁴⁴ Optimization requires a balance between small tube diameter to avoid drug encapsulation and large exterior surface area to enhance the interactions between the drug and the carrier. Further studies are needed in order to find an optimized diameter range for SWNTs to enable strong drug-carrier interactions that can overcome all barriers in the transportation process and to ensure the majority of VLB molecules are delivered to the target site.

3.3.4 Interaction energy levels

Throughout different systems, VLB had three stable orientations with the exterior tube sidewall. The nonparallel exterior-bound position with the low interaction energy of nearly -80 kJ/mol mainly involved interactions between the vindoline moiety of VLB and the sidewall. The parallel exterior-bound position gave a medium interaction energy of nearly -100 kJ/mol and involved interactions between both catharanthine and vindoline moieties of VLB and the sidewall, with C16 and N1 facing toward the tube. The parallel

exterior-bound position with higher interaction energy of nearly -120 kJ/mol involved the interactions of both sub-parts of VLB with the sidewall, with C16 and N1 facing away from the tube. Unlike the attachment-mode, the movement of VLB inside the tube under the encapsulation mode was more flexible. Interestingly, VLB displayed the three orientations described in the attachment-mode in one trajectory under the encapsulation mode, the interaction energy fluctuated accordingly. Compared to the small portion of the curved exterior sidewall exposed to the VLB attached to the outside of a tube, more surface area was available to VLB under encapsulation which resulted in a much stronger interaction energy of nearly -210 kJ/mol. (**Figure 3.12**)

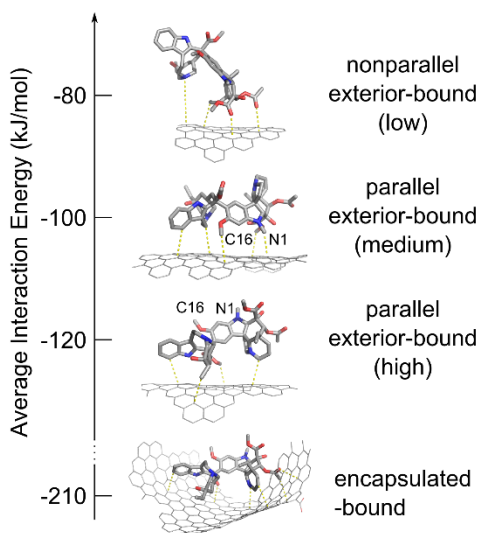


Figure 3.12 The stable orientations of VLB corresponding to different energy levels.

3.3.5 Effect of functionalization

Functionalization of CNT termini affects the strength of the drug–carrier interactions. At 300 K, CNT esterification in a system with one VLB molecule strengthened the VLB–CNT interactions by 20.7 kJ/mol. In a system with two VLB molecules, the

functionalization weakened the VLB–CNT interactions of one VLB molecule by 15.0 kJ/mol, but did not affect the other VLB molecule. Moreover, in CNT–3VLB, with two VLB molecules initially positioned outside the tube and one VLB encapsulated inside, upon the transition of one of the VLB molecules from outside the tube into the tube, functionalization of the CNT showed an increase of 15.6 kJ/mol in VLB–CNT interactions for the VLB that remained outside the tube. Therefore, functionalization enhanced the drug–carrier interactions when only one VLB was loaded outside the tube. For multiple payloads, it is inferred that the strength was also affected by the loading capacity of the carrier and that, upon functionalization, the interactions would be strengthened with sufficiently long tube.

Nevertheless, at 277 K, when one drug was loaded, functionalization weakened the interactions by 34.5 kJ/mol. When two VLB molecules were loaded, functionalization did not affect one VLB molecule but weakened the interactions for the other VLB by 35.8 kJ/mol, which had a greater effect compared with the system at 300 K. In the system with three VLB molecules, functionalization weakened the interactions for one of the molecules outside the tube by 17.9 kJ/mol but did not affect the other VLB outside the tube. Overall, functionalization weakened the drug-carrier interactions at 277 K.

The encapsulated molecules were not affected by esterification of the CNT as the structure of the side with which they interacted was not influenced by modifications on tube ends. Based on these observations, it is proposed that longer CNTs would have a larger loading capacity for the attachment of drug molecules. The esterified functionalization would strengthen the interactions at 300 K and most VLB molecules

would orient in the parallel exterior-bound position with the most stable energy level. Alternatively, at 277 K, if attached to a longer tube, most VLB molecules would likely orient in the nonparallel exterior-bound position with the least stable energy level.

The high toxicity of pristine CNTs⁴⁵⁻⁴⁶ can be reduced by functionalization. The introduction of polar groups would also increase the solubility and dispersion of CNTs. CNT functionalization is an essential step leading to the manufacture of commercial CNT-based drug carriers.

3.3.6 Effect of temperature

In non-functionalized systems, the VLB-CNT interactions in CNT-1VLB_Out and the overall VLB-CNT interactions in SWNT-2VLB were enhanced at 277 K. Conversely, the lower temperature weakened the VLB-CNT interactions in CNT-1VLB_In.

In functionalized systems, the lower temperature reduced the VLB-CNT interactions for the VLB attached to the exterior of the tube but did not affect the VLB inside the tube. For a system with two VLB molecules loaded outside the tube, the lower temperature did not affect the VLB-CNT interactions.

In functionalized systems with three VLB molecules, the reduced temperature did not influence the encapsulated VLB, however, it showed different effects on the attached VLB molecules depending on the chirality of CNTs. In the armchair CNT system, one of the two attached VLB molecules entered the tube, the lower temperature did not affect VLB-CNT interactions for the VLB molecule that remained outside the tube. In the chiral CNT system, the lower temperature slightly increased the interactions for one of the VLB molecules by 19.1 kJ/mol. In the zigzag CNT system, one of the two attached

VLB molecules entered the tube, while the lower temperature slightly decreased the interactions for the VLB molecule that remained outside the tube by 16.2 kJ/mol. Therefore, aiming for the delivery of multiple drug molecules by functionalized CNT, the functionalized armchair CNT is the best option for the delivery at room temperature and 277 K. At 277 K, the enhanced drug-carrier interactions make functionalized chiral CNTs a particularly good choice for delivery at temperatures below 300 K.

3.4 Conclusions

In this chapter, the stable orientations of VLB with respect to the CNT carrier, and the effect of temperature change as well as CNT structure on several different VLB–CNT systems with one to three VLB molecules have been discussed. VLB showed three stable orientations on the CNT sidewall under the attachment loading mode, which corresponded to three energy levels with low, medium and high strength of interactions with the energy gap between each orientation of ~ 20 kJ/mol. The encapsulation mode of loading VLB could be challenging for drug release to the target, as all VLB molecules placed inside the tube remained encapsulated during the entire simulation. The stable VLB orientations have been observed among all three different types of CNT carriers, and chirality shows slight impact on drug orientations due to the different arrangement of carbon atoms. When the diameter of CNT is large enough to accommodate a VLB molecule into the tube, with the proper orientation and strong interactions, a VLB molecule can enter the tube and become trapped. This occurred to one of the VLB molecules attached to the functionalized armchair CNT at 300 K and to the

functionalized zigzag CNT at 277 K. These simulations provide clues to design appropriate CNT-based drug-carriers so that unwanted encapsulation can be avoided.

Functionalization is necessary to reduce the toxicity of CNT and to improve the biocompatibility with biological systems, and it would likely enhance the VLB–CNT interactions of a longer CNT with higher loading capacity at 300 K. In terms of the possible temperature-adapted cancer treatment, the functionalized armchair CNT is a good option for the drug delivery at both 277 K and 300 K because of the relatively strong drug–carrier interactions. The functionalized chiral CNT is especially suitable for VLB delivery at 277 K.

Overall, this study has revealed the interactions of VLB with CNT in various systems, which offers fundamental knowledge for the design and optimization of CNT-based carriers for VLB delivery.

3.5 Bibliography

1. De Volder, M. F. L.; Tawfick, S. H.; Baughman, R. H.; Hart, A. J. Carbon Nanotubes: Present and Future Commercial Applications. *Science* **2013**, *339*, 535-539.
2. Heister, E.; Brunner, E. W.; Dieckmann, G. R.; Jurewicz, I.; Dalton, A. B. Are Carbon Nanotubes a Natural Solution? Applications in Biology and Medicine. *ACS Applied Materials & Interfaces* **2013**, *5*, 1870-1891.
3. Maiti, U. N.; Lee, W. J.; Lee, J. M.; Oh, Y.; Kim, J. Y.; Kim, J. E.; Shim, J.; Han, T. H.; Kim, S. O. 25th Anniversary Article: Chemically Modified/Doped Carbon

- Nanotubes & Graphene for Optimized Nanostructures & Nanodevices. *Advanced Materials* **2014**, *26*, 40-67.
4. Mundra, R. V.; Wu, X.; Sauer, J.; Dordick, J. S.; Kane, R. S. Nanotubes in Biological Applications. *Current Opinion in Biotechnology* **2014**, *28*, 25-32.
 5. Karimi, M.; Solati, N.; Ghasemi, A.; Estiar, M. A.; Hashemkhani, M.; Kiani, P.; Mohamed, E.; Saeidi, A.; Taheri, M.; Avci, P., et al. Carbon Nanotubes Part Ii: A Remarkable Carrier for Drug and Gene Delivery. *Expert Opinion on Drug Delivery* **2015**, *12*, 1089-1105.
 6. Liu, Z.; Fan, A. C.; Rakhra, K.; Sherlock, S.; Goodwin, A.; Chen, X.; Yang, Q.; Felsher, D. W.; Dai, H. Supramolecular Stacking of Doxorubicin on Carbon Nanotubes for in Vivo Cancer Therapy. *Angewandte Chemie International Edition* **2009**, *48*, 7668-7672.
 7. Weng, X.; Wang, M.; Ge, J.; Yu, S.; Liu, B.; Zhong, J.; Kong, J. Carbon Nanotubes as a Proteintoxin Transporter for Selective Her2-Positive Breast Cancer Cell Destruction. *Molecular BioSystems* **2009**, *5*, 1224-1231.
 8. Podesta, J. E.; Al-Jamal, K. T.; Herrero, M. A.; Tian, B.; Ali-Boucetta, H.; Hegde, V.; Bianco, A.; Prato, M.; Kostarelos, K. Antitumor Activity and Prolonged Survival by Carbon-Nanotube-Mediated Therapeutic Sirna Silencing in a Human Lung Xenograft Model. *Small* **2009**, *5*, 1176-1185.
 9. Raffa, V.; Ciofani, G.; Vittorio, O.; Riggio, C.; Cuschieri, A. Physicochemical Properties Affecting Cellular Uptake of Carbon Nanotubes. *Nanomedicine* **2010**, *5*, 89-97.

10. Kang, B.; Chang, S.; Dai, Y.; Yu, D.; Chen, D. Cell Response to Carbon Nanotubes: Size-Dependent Intracellular Uptake Mechanism and Subcellular Fate. *Small* **2010**, *6*, 2362-2366.
11. Lacerda, L.; Russier, J.; Pastorin, G.; Herrero, M. A.; Venturelli, E.; Dumortier, H.; Al-Jamal, K. T.; Prato, M.; Kostarelos, K.; Bianco, A. Translocation Mechanisms of Chemically Functionalised Carbon Nanotubes across Plasma Membranes. *Biomaterials* **2012**, *33*, 3334-3343.
12. Delogu, L. G.; Venturelli, E.; Manetti, R.; Pinna, G. A.; Carru, C.; Madeddu, R.; Murgia, L.; Sgarrella, F.; Dumortier, H.; Bianco, A. Ex Vivo Impact of Functionalized Carbon Nanotubes on Human Immune Cells. *Nanomedicine* **2011**, *7*, 231-243.
13. Bianco, A.; Kostarelos, K.; Prato, M. Applications of Carbon Nanotubes in Drug Delivery. *Current Opinion in Chemical Biology* **2005**, *9*, 674-679.
14. Liu, Z.; Sun, X.; Nakayama-Ratchford, N.; Dai, H. Supramolecular Chemistry on Water-Soluble Carbon Nanotubes for Drug Loading and Delivery. *ACS Nano* **2007**, *1*, 50-56.
15. Liu, Z.; Chen, K.; Davis, C.; Sherlock, S.; Cao, Q.; Chen, X.; Dai, H. Drug Delivery with Carbon Nanotubes for in Vivo Cancer Treatment. *Cancer Research* **2008**, *68*, 6652-6660.
16. Kang, B.; Yu, D.; Dai, Y.; Chang, S.; Chen, D.; Ding, Y. Cancer-Cell Targeting and Photoacoustic Therapy Using Carbon Nanotubes as “Bomb” Agents. *Small* **2009**, *5*, 1292-1301.

17. Tamsyn, A. H.; James, M. H. Modelling the Encapsulation of the Anticancer Drug Cisplatin into Carbon Nanotubes. *Nanotechnology* **2007**, *18*, 275704.
18. Hilder, T. A.; Hill, J. M. Probability of Encapsulation of Paclitaxel and Doxorubicin into Carbon Nanotubes *Micro & Nano Letters* **2008**.
19. Jordan, M. A.; Wilson, L. Microtubules as a Target for Anticancer Drugs. *Nature Reviews Cancer* **2004**, *4*, 253-265.
20. Mollaamin, F.; Monajjemi, M.; Mehrzad, J. Molecular Modeling Investigation of an Anti-Cancer Agent Joint to Swcnt Using Theoretical Methods. *Fullerenes, Nanotubes and Carbon Nanostructures* **2013**, *22*, 738-751.
21. Gao, H.; Kong, Y. Simulation of DNA-Nanotube Interactions. *Annual Review of Materials Research* **2004**, *34*, 123-150.
22. Minoia, A.; Chen, L.; Beljonne, D.; Lazzaroni, R. Molecular Modeling Study of the Structure and Stability of Polymer/Carbon Nanotube Interfaces. *Polymer* **2012**, *53*, 5480-5490.
23. Chaban, V. V.; Savchenko, T. I.; Kovalenko, S. M.; Prezhdo, O. V. Heat-Driven Release of a Drug Molecule from Carbon Nanotubes: A Molecular Dynamics Study. *The Journal of Physical Chemistry B* **2010**, *114*, 13481-13486.
24. Alisaraie, L.; Tuszynski, J. A. Determination of Noscapine's Localization and Interaction with the Tubulin-A/B Heterodimer. *Chemical Biology & Drug Design* **2011**, *78*, 535-546.
25. Tuszynski, J.; Craddock, T. A.; Mane, J.; Barakat, K.; Tseng, C.-Y.; Gajewski, M.; Winter, P.; Alisaraie, L.; Patterson, J.; Carpenter, E., et al. Modeling the Yew Tree

- Tubulin and a Comparison of Its Interaction with Paclitaxel to Human Tubulin. *Pharmaceutical Research* **2012**, *29*, 3007-3021.
26. Li, Z.; Alisaraie, L. Microtubules Dual Chemo and Thermo-Responsive Depolymerization. *Proteins: Structure, Function, and Bioinformatics* **2015**, *83*, 970-981.
 27. Balasubramanian, K.; Burghard, M. Chemically Functionalized Carbon Nanotubes. *Small* **2005**, *1*, 180-192.
 28. Jorgensen, W. L.; Tirado-Rives, J. The Opls [Optimized Potentials for Liquid Simulations] Potential Functions for Proteins, Energy Minimizations for Crystals of Cyclic Peptides and Crambin. *Journal of the American Chemical Society* **1988**, *110*, 1657-1666.
 29. Jorgensen, W. L.; Maxwell, D. S.; Tirado-Rives, J. Development and Testing of the Opls All-Atom Force Field on Conformational Energetics and Properties of Organic Liquids. *Journal of the American Chemical Society* **1996**, *118*, 11225-11236.
 30. Price, M. L. P.; Ostrovsky, D.; Jorgensen, W. L. Gas-Phase and Liquid-State Properties of Esters, Nitriles, and Nitro Compounds with the Opls-Aa Force Field. *Journal of Computational Chemistry* **2001**, *22*, 1340-1352.
 31. Kaminski, G. A.; Friesner, R. A.; Tirado-Rives, J.; Jorgensen, W. L. Evaluation and Reparametrization of the Opls-Aa Force Field for Proteins Via Comparison with Accurate Quantum Chemical Calculations on Peptides. *The Journal of Physical Chemistry B* **2001**, *105*, 6474-6487.

32. Van Der Spoel, D.; Lindahl, E.; Hess, B.; Groenhof, G.; Mark, A. E.; Berendsen, H. J. C. Gromacs: Fast, Flexible, and Free. *Journal of Computational Chemistry* **2005**, *26*, 1701-1718.
33. Hess, B.; Kutzner, C.; van der Spoel, D.; Lindahl, E. Gromacs 4: Algorithms for Highly Efficient, Load-Balanced, and Scalable Molecular Simulation. *Journal of Chemical Theory and Computation* **2008**, *4*, 435-447.
34. Oostenbrink, C.; Villa, A.; Mark, A. E.; Van Gunsteren, W. F. A Biomolecular Force Field Based on the Free Enthalpy of Hydration and Solvation: The Gromos Force-Field Parameter Sets 53a5 and 53a6. *Journal of Computational Chemistry* **2004**, *25*, 1656-1676.
35. Ribeiro, A. A. S. T.; Horta, B. A. C.; Alencastro, R. B. d. Mktop: A Program for Automatic Construction of Molecular Topologies. *Journal of the Brazilian Chemical Society* **2008**, *19*, 1433-1435.
36. JCrystalSoft. <http://www.jcrystal.com/> (accessed November 30, 2014).
37. Xiu, P.; Zhou, B.; Qi, W.; Lu, H.; Tu, Y.; Fang, H. Manipulating Biomolecules with Aqueous Liquids Confined within Single-Walled Nanotubes. *Journal of the American Chemical Society* **2009**, *131*, 2840-2845.
38. Xiu, P.; Yang, Z.; Zhou, B.; Das, P.; Fang, H.; Zhou, R. Urea-Induced Drying of Hydrophobic Nanotubes: Comparison of Different Urea Models. *The Journal of Physical Chemistry B* **2011**, *115*, 2988-2994.

39. Darden, T.; York, D.; Pedersen, L. Particle Mesh Ewald: An N·Log(N) Method for Ewald Sums in Large Systems. *The Journal of Chemical Physics* **1993**, *98*, 10089-10092.
40. Hess, B.; Bekker, H.; Berendsen, H. J. C.; Fraaije, J. G. E. M. Lincs: A Linear Constraint Solver for Molecular Simulations. *Journal of Computational Chemistry* **1997**, *18*, 1463-1472.
41. WestGrid consortium. <http://www.westgrid.ca/> (accessed November 25, 2013).
42. Bau, R.; Jin, K. K. Crystal Structure of Vinblastine. *Journal of the Chemical Society, Perkin Transactions 1* **2000**, 2079-2082.
43. Gao, H.; Kong, Y.; Cui, D.; Ozkan, C. S. Spontaneous Insertion of DNA Oligonucleotides into Carbon Nanotubes. *Nano Letters* **2003**, *3*, 471-473.
44. Berber, S.; Kwon, Y.-K.; Tománek, D. Microscopic Formation Mechanism of Nanotube Peapods. *Physical Review Letters* **2002**, *88*, 185502.
45. Lam, C.-W.; James, J. T.; McCluskey, R.; Hunter, R. L. Pulmonary Toxicity of Single-Wall Carbon Nanotubes in Mice 7 and 90 Days after Intratracheal Instillation. *Toxicological Sciences* **2004**, *77*, 126-134.
46. Sayes, C. M.; Liang, F.; Hudson, J. L.; Mendez, J.; Guo, W.; Beach, J. M.; Moore, V. C.; Doyle, C. D.; West, J. L.; Billups, W. E., et al. Functionalization Density Dependence of Single-Walled Carbon Nanotubes Cytotoxicity in Vitro. *Toxicology Letters* **2006**, *161*, 135-142.

CHAPTER 4

Summary

In this thesis, the possible binding site of doxorubicin at the $\alpha\beta$ -tubulin heterodimer has been explored. The conformational changes of tubulin dimer triggered by the anti-mitotic drug VLB and the low temperature condition have been unveiled by means of MD simulation. The similar responses of tubulin heterodimer to both VLB and low temperature provide clues toward establishing novel strategies on combatting cancer diseases.

The stable orientations of VLB with respect to the CNT carrier as well as the effects of CNT structure and temperature change on several different VLB–CNT systems have also been discussed. These simulations provide guidance to design appropriate CNT carriers to avoid drug molecules being trapped inside the tube. Based on the fundamental knowledge revealed through the interactions of VLB with CNT in various systems, it is proposed that the functionalized armchair CNT is appropriate for the drug delivery at 277 K as well as 300 K, and the functionalized chiral CNT is suitable for VLB delivery at 277 K.

Future perspectives based on this work are summarized in the following two aspects. First, the DOX–MT system is worthwhile for further investigations using MD simulation

to elucidate more detailed interactions and ligand-induced conformational changes, by taking into account flexibilities of both protein and DOX in solution phase similar to the VLB–MT system as it has been discussed in Chapter 2. Second, the VLB–CNT research was the first phase of our project to study SWNTs as carriers for the drug whose delivery has not been examined so far. Hence, the fundamental knowledge to explore design rules is required to develop the project to a more advanced level. Further simulations could be carried out on CNTs longer than 50 Å with various diameters in order to compare the modelling results with *in vitro* experimental studies on CNT-based drug delivery systems.

List of Appendices

Appendix A

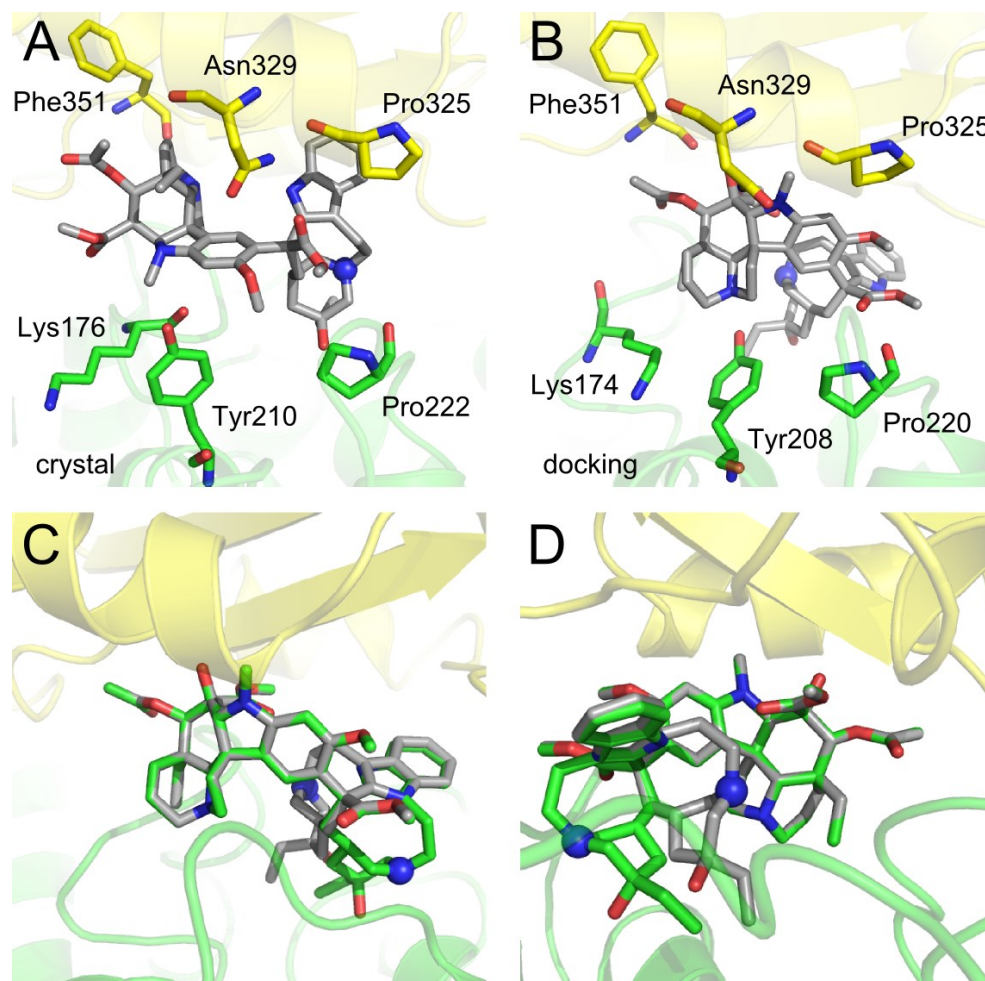


Figure A1 VLB geometry in (A) crystal structure of 4EB6 and (B) the first ranked docking solution. Some interacting residues from α -tubulin (yellow) and β -tubulin (green) are shown at the binding pocket. (C) Front and (D) back view of the 1st ranked (gray) and 6th ranked (green) docking poses. The protonated nitrogen is highlighted in a sphere.

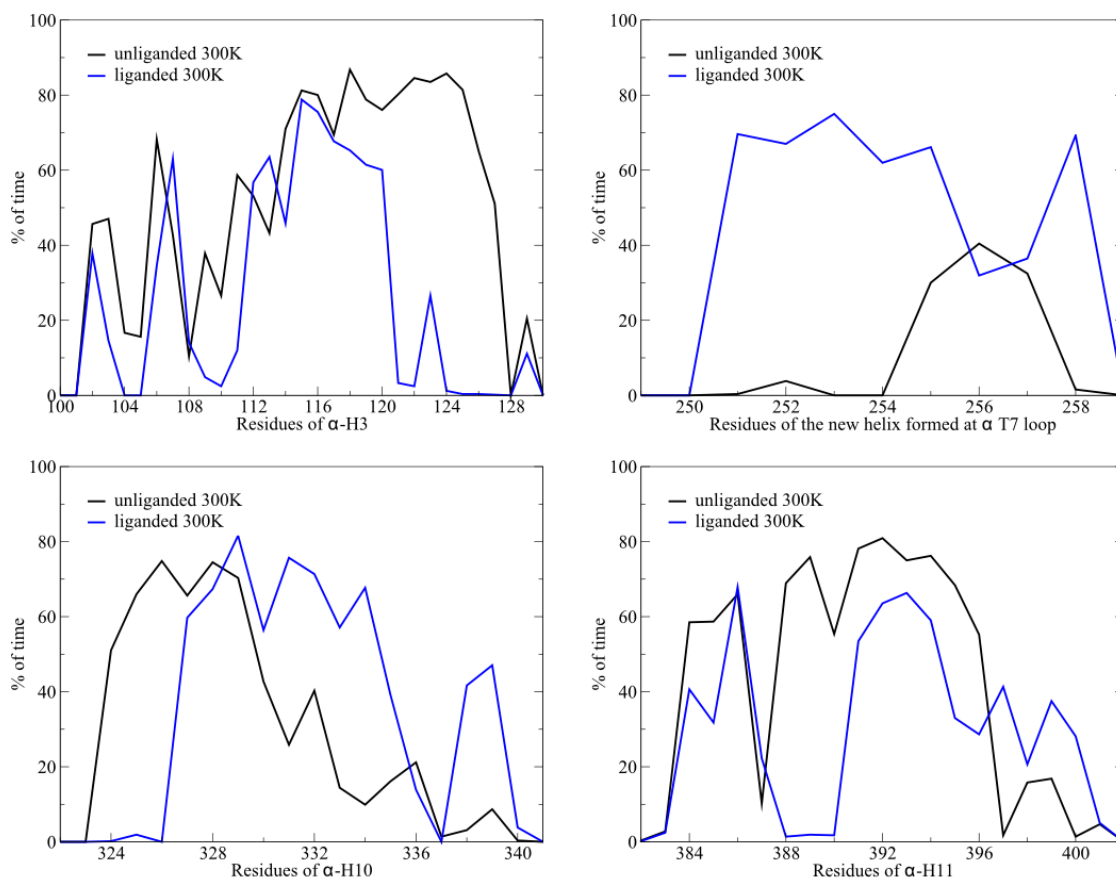


Figure A2 Helicity plots of H3, the new helix formed at T7 loop, H10 and H11 in α -tubulin comparing the unliganded and liganded system at 300 K.

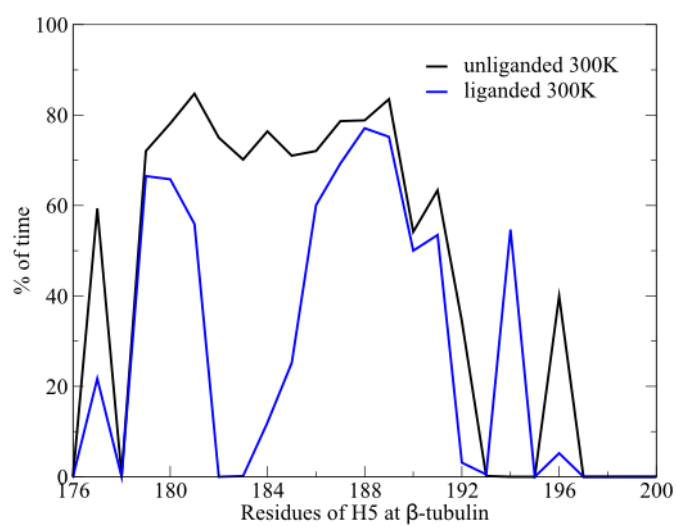


Figure A3 Helicity plots of H5 in β -tubulin comparing the unliganded and liganded systems at 300 K.

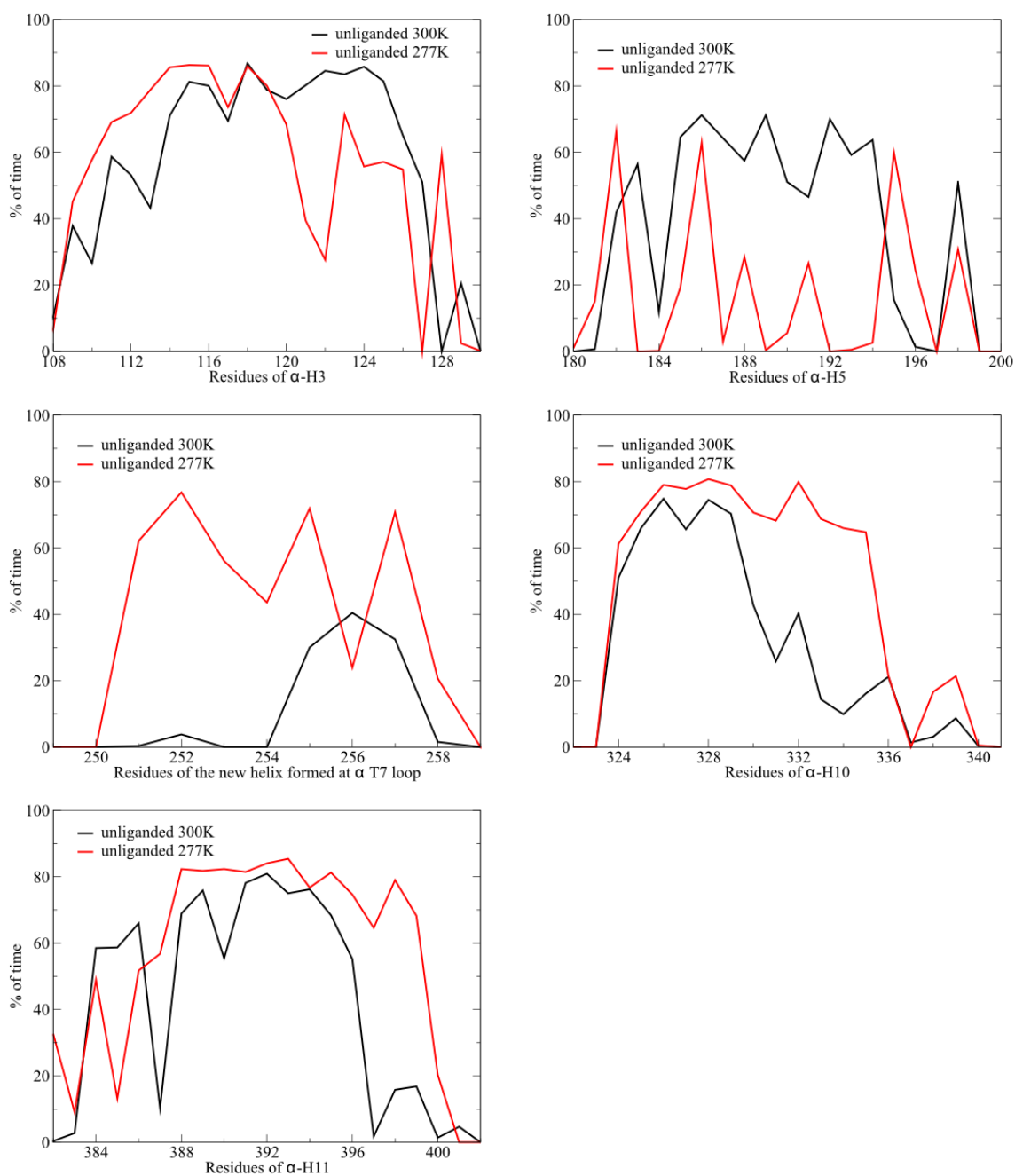


Figure A4 Helicity plots of H3, H5, the new helix formed at T7 loop, H10 and H11 in α -tubulin comparing the unliganded systems at 300 K and 277 K, respectively.

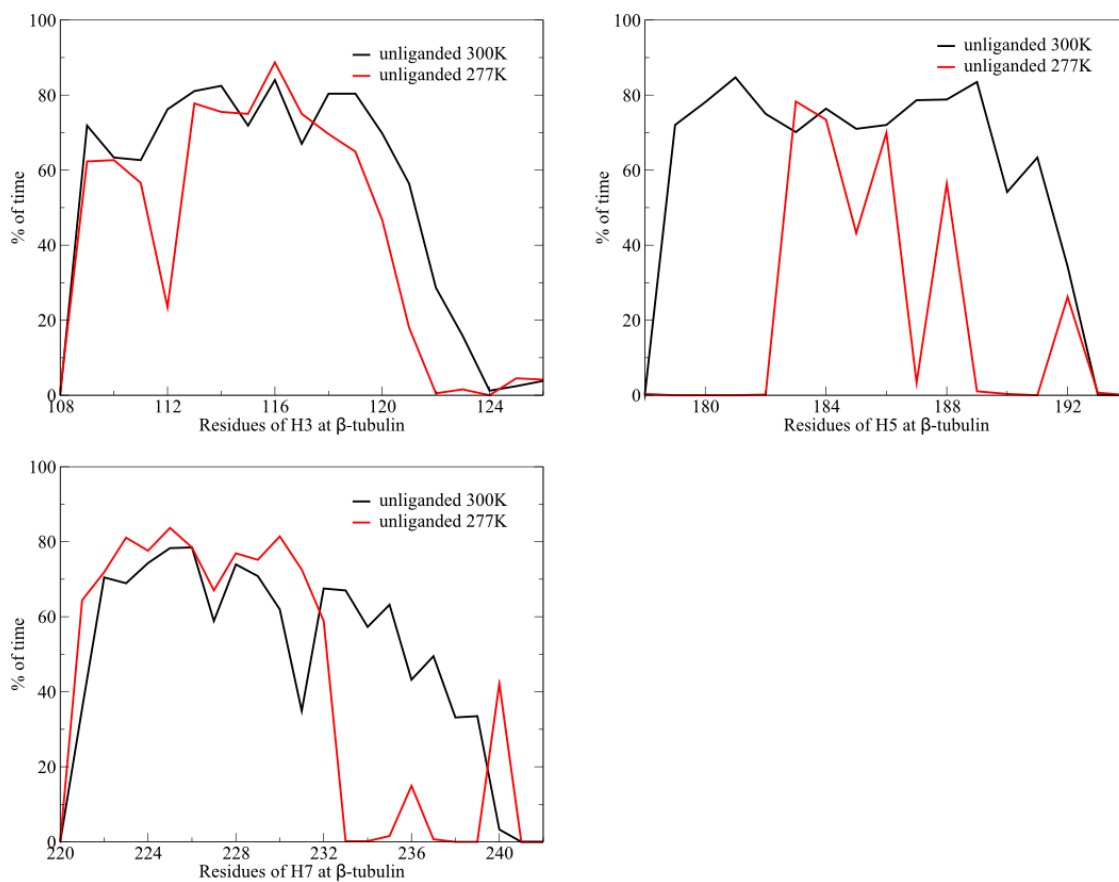


Figure A5 Helicity plots of H3, H5 and H7 in β -tubulin comparing the unliganded system at 300 K and 277 K, respectively.

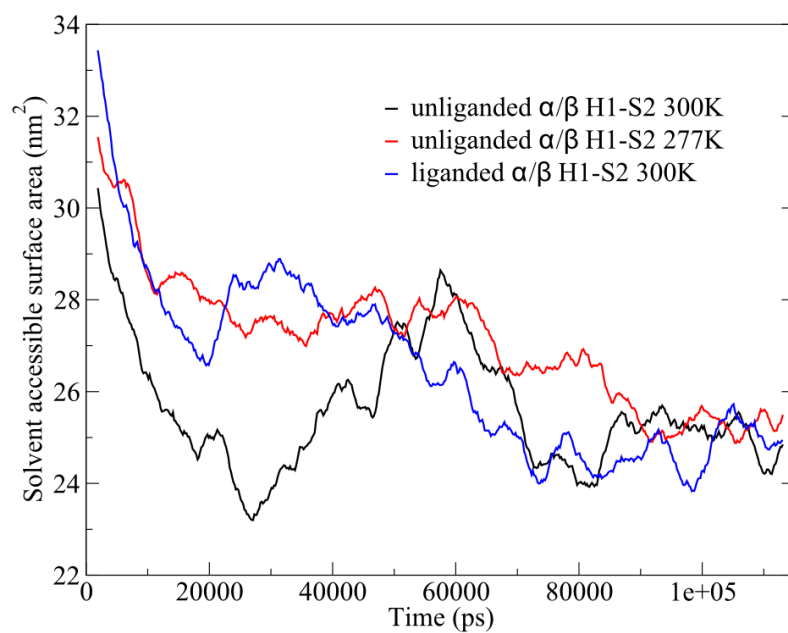


Figure A6 SASA of the loop H1-S2 in three systems changing over the course of the simulation time.

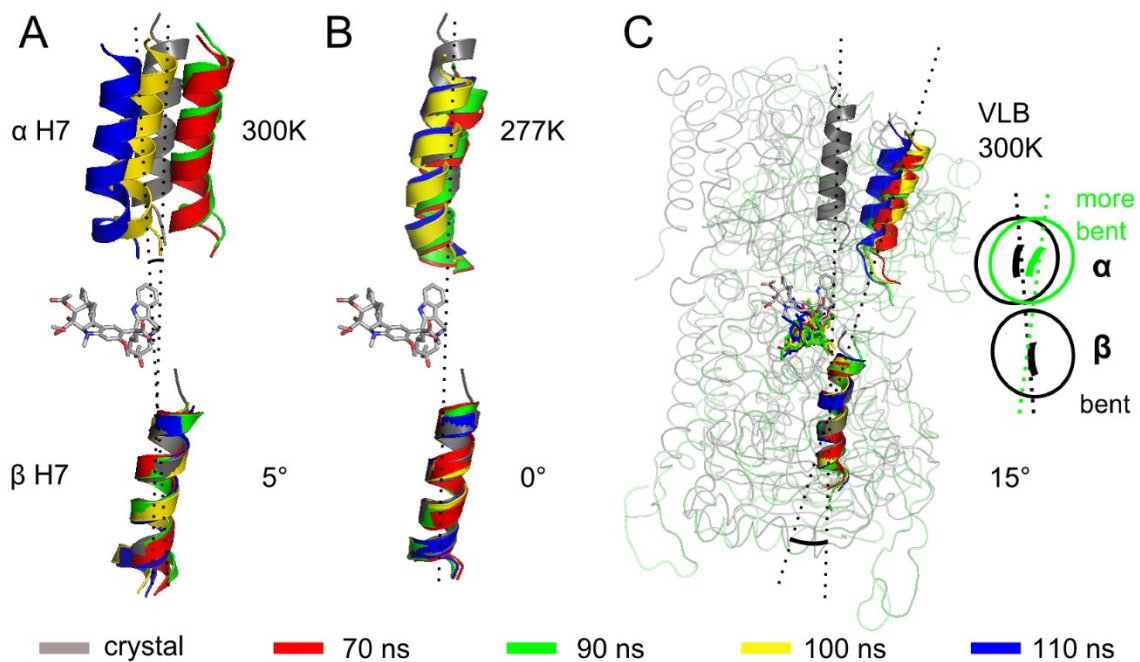


Figure A7 The curvature of $\alpha\beta$ -tubulin heterodimer represented by H7 orientation of the unliganded heterodimer at (A) 300 K, (B) 277 K and of (C) the liganded heterodimer at 300 K from the 2nd round simulations. The angles indicate the average deviation of heterodimers shifting from the curved conformation in the crystal structure. The inset scheme at (C) describes the structure caused by VLB with more bending than the crystal structure.

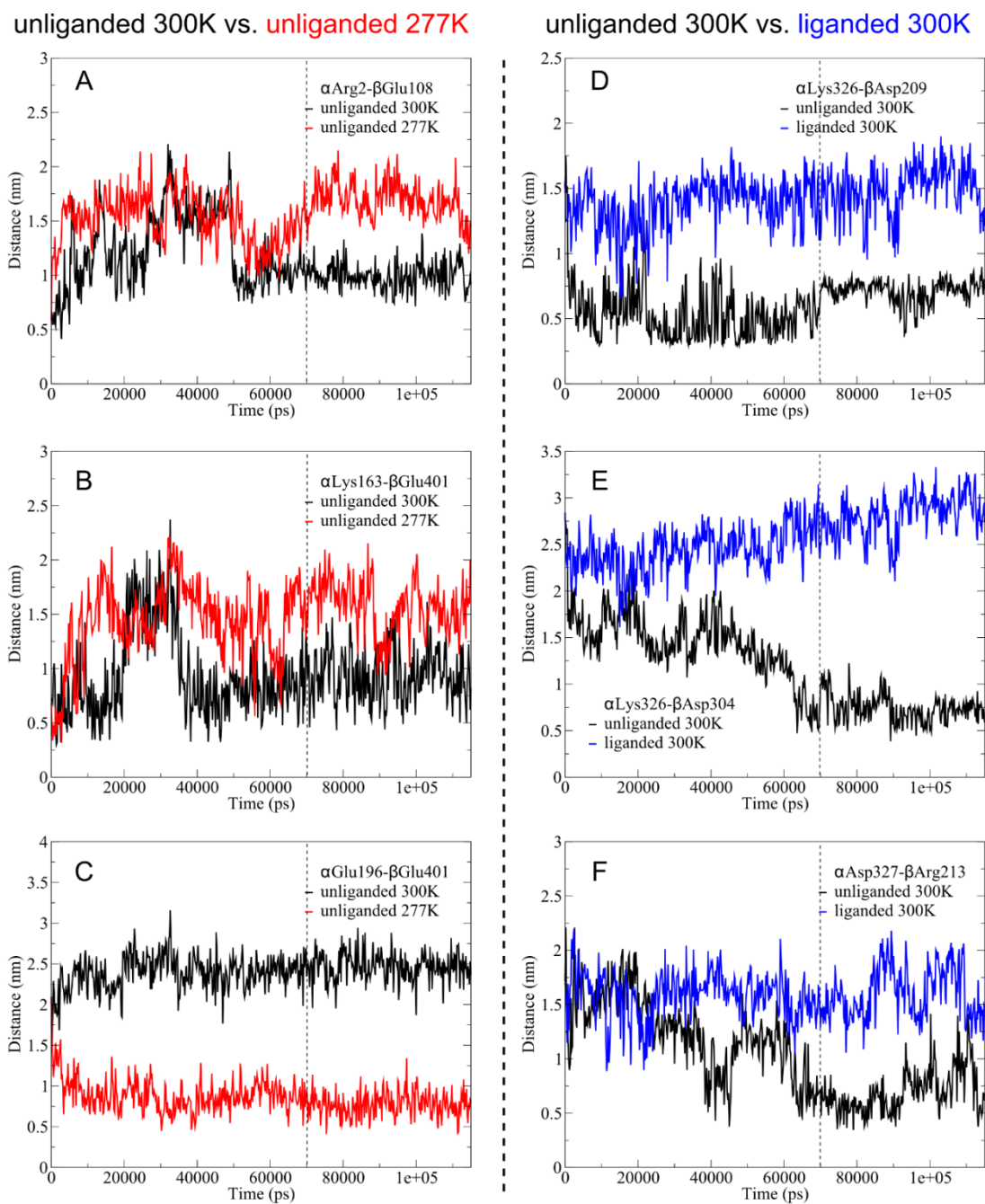


Figure A8 The distance between the charged residues contributing to the electrostatic surface. Each panel is a comparison of a pair of charged residues under two different conditions. The dashed line indicates the convergence point.

Table A1 The top 10 docking solutions of the mono-protonated VLB ranked by *FlexX*.

Rank	Score (kJ/mol)	Match (kJ/mol)	Lipophilic (kJ/mol)	Ambiguous (kJ/mol)	Clash (kJ/mol)	RMSD (Å)
1	-8.0814	-13.0764	-13.542	-8.5235	4.8606	6.3851
2	-6.2647	-14.7242	-11.4641	-9.289	7.0126	10.7734
3	-6.1923	-15.6398	-12.7842	-9.3892	9.4209	8.6124
4	-5.3067	-15.6806	-13.5578	-9.0258	10.7575	8.1732
5	-4.4144	-12.9817	-16.1357	-9.473	11.9761	7.5182
6	-3.7758	-10.6882	-12.59	-7.3485	4.6505	6.3335
7	-3.4799	-12.7875	-13.0774	-7.8528	8.0378	8.3967
8	-3.3683	-15.5418	-9.7845	-8.9348	8.6928	9.1038
9	-2.0776	-15.5224	-13.6993	-8.3718	13.3159	7.4438
10	-1.9751	-10.7183	-11.3053	-6.2374	4.0859	8.8255

Score: total score of the docking solution

Match: contribution of the matched interacting groups

Lipophilic: contribution of the lipophilic contact area

Ambiguous: contribution of the lipophilic-hydrophilic (ambiguous) contact area

Clash: contribution of the clash penalty

RMSD: RMSD of coordinates from reference coordinates

Appendix B

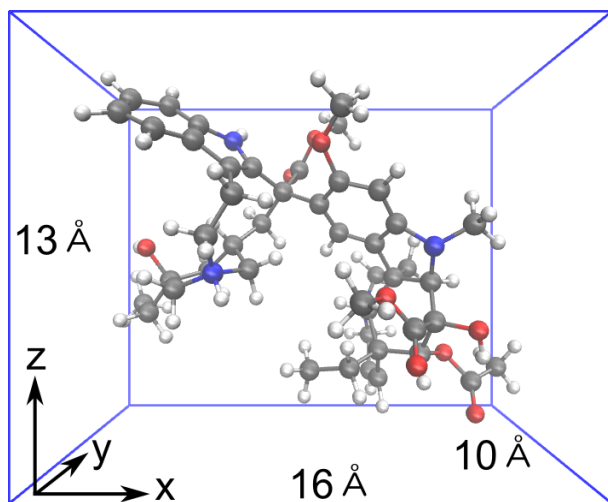


Figure B1 Size of VLB showing in a 3D box.

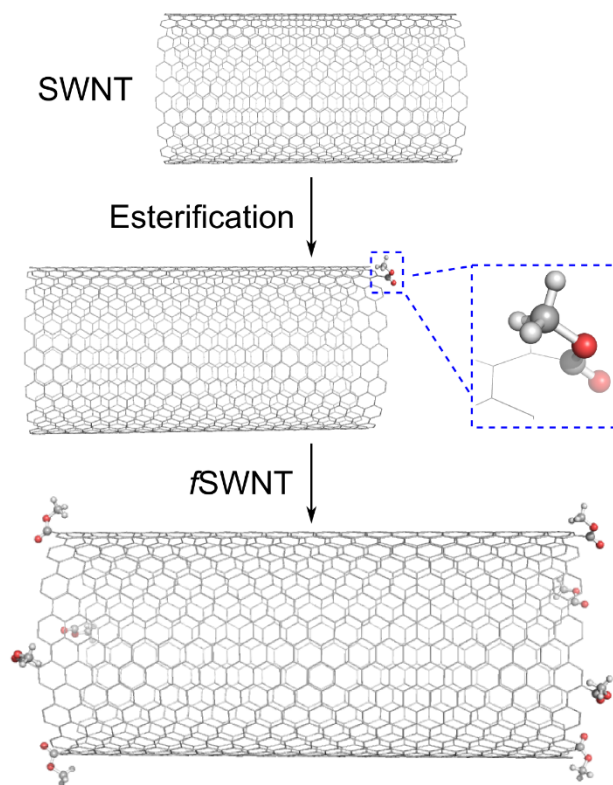


Figure B2 Esterification of SWNT.

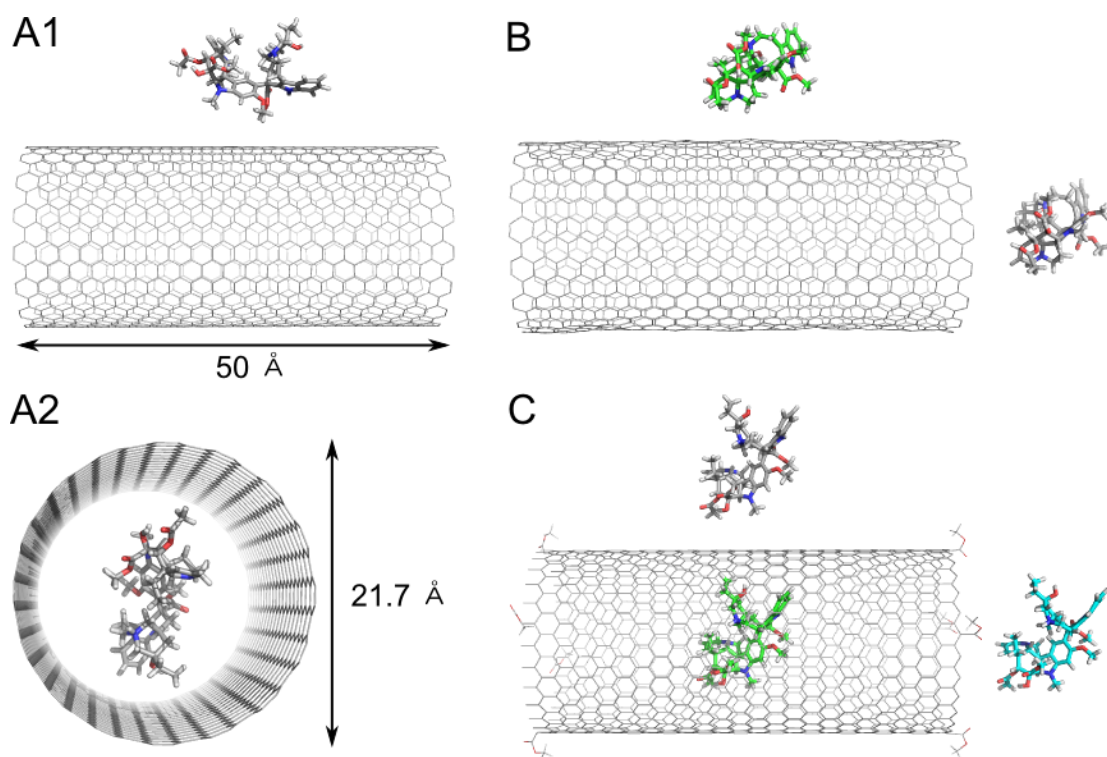


Figure B3 Initial configurations of CNT-1VLB system (A1, attached VLB; A2, encapsulated VLB), CNT-2VLB system (B) and CNT-3VLB system (C, fZigzag used as an example). Double arrow lines indicate the length and diameter of the armchair SWNT.

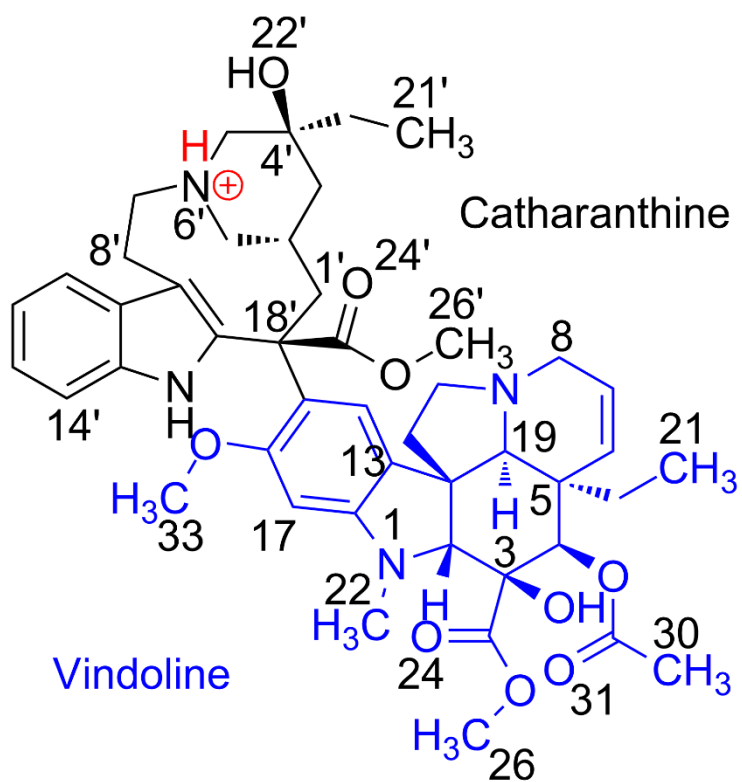


Figure B4 Chemical structure of mono-protonated VLB.

Table B1 Dimensional parameters of SWNT.

CNT type	Armchair (16, 16)	Chiral (17, 15)	Zigzag (28, 0)
Length (Å)	50	50	50
Diameter (Å)	21.7	21.7	21.9

Table B2 Diameter of six armchair SWNTs.

Armchair CNT	Diameter (Å)
(11, 11)	14.927
(12, 12)	16.283
(13, 13)	17.64
(14, 14)	18.977
(15, 15)	20.354
(16, 16)	21.711

Appendix C

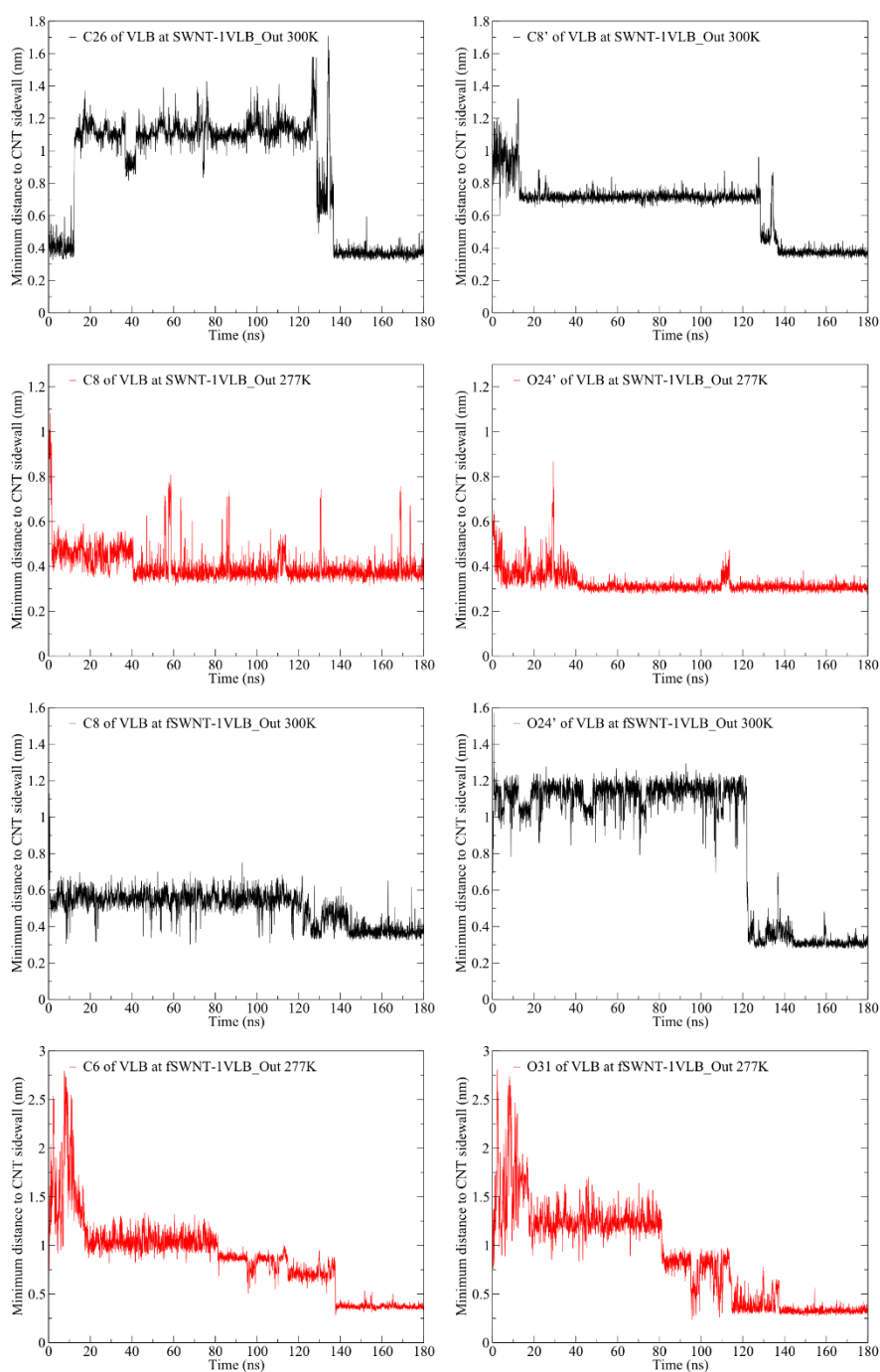


Figure C1 The distances between selected VLB atoms and CNT sidewall over the simulation for the non-functionalized and functionalized SWNT-1VLB_Out systems.

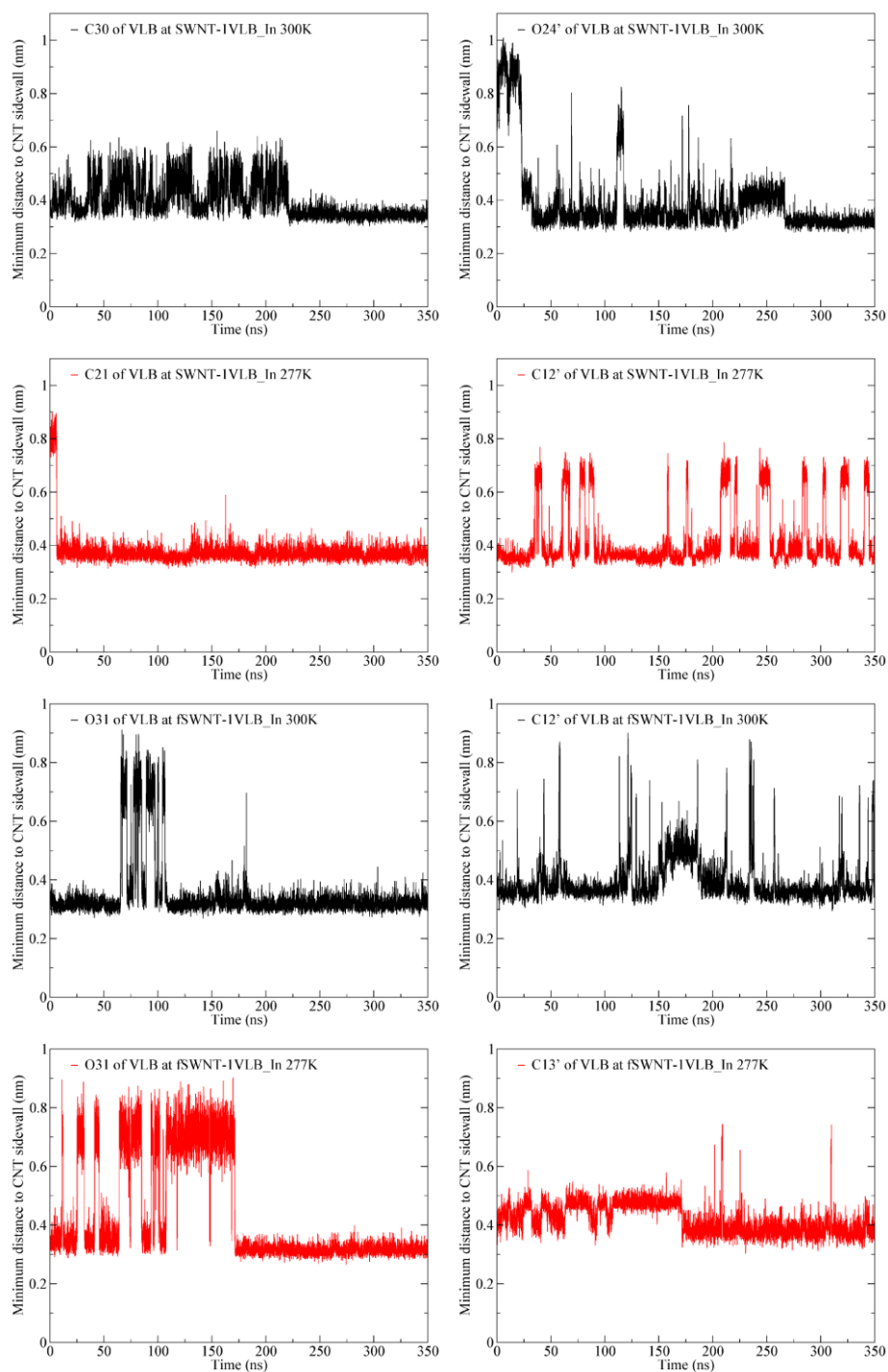


Figure C2 The minimum distances of selected VLB atoms to CNT sidewall for the non-functionalized and functionalized SWNT-1VLB_In over the entire simulation time.

Appendix D

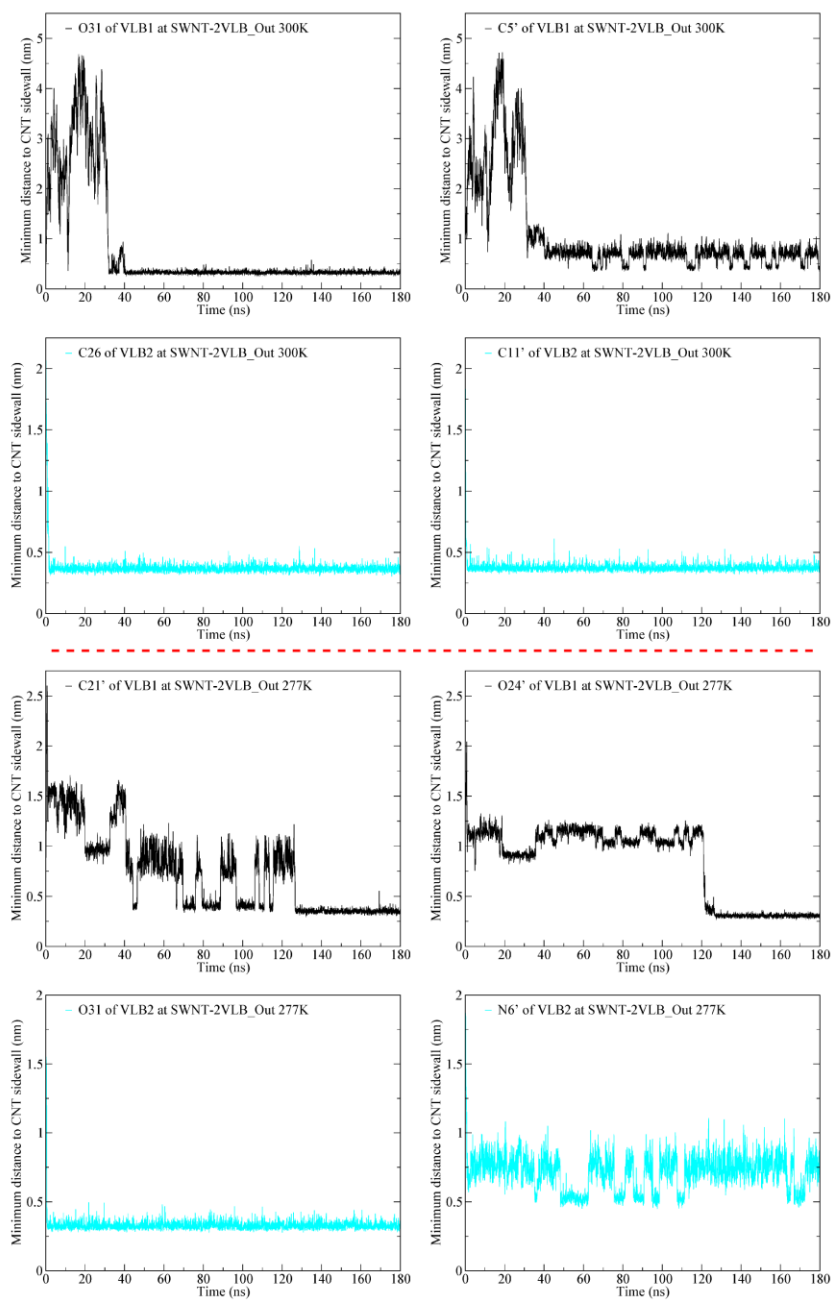


Figure D1 The distances between selected atoms in VLB1 and VLB2 and CNT sidewall for SWNT-2VLB at 300 K (above red dashed line) and 277 K (below red dashed line). VLB1 is in black and VLB2 in cyan.

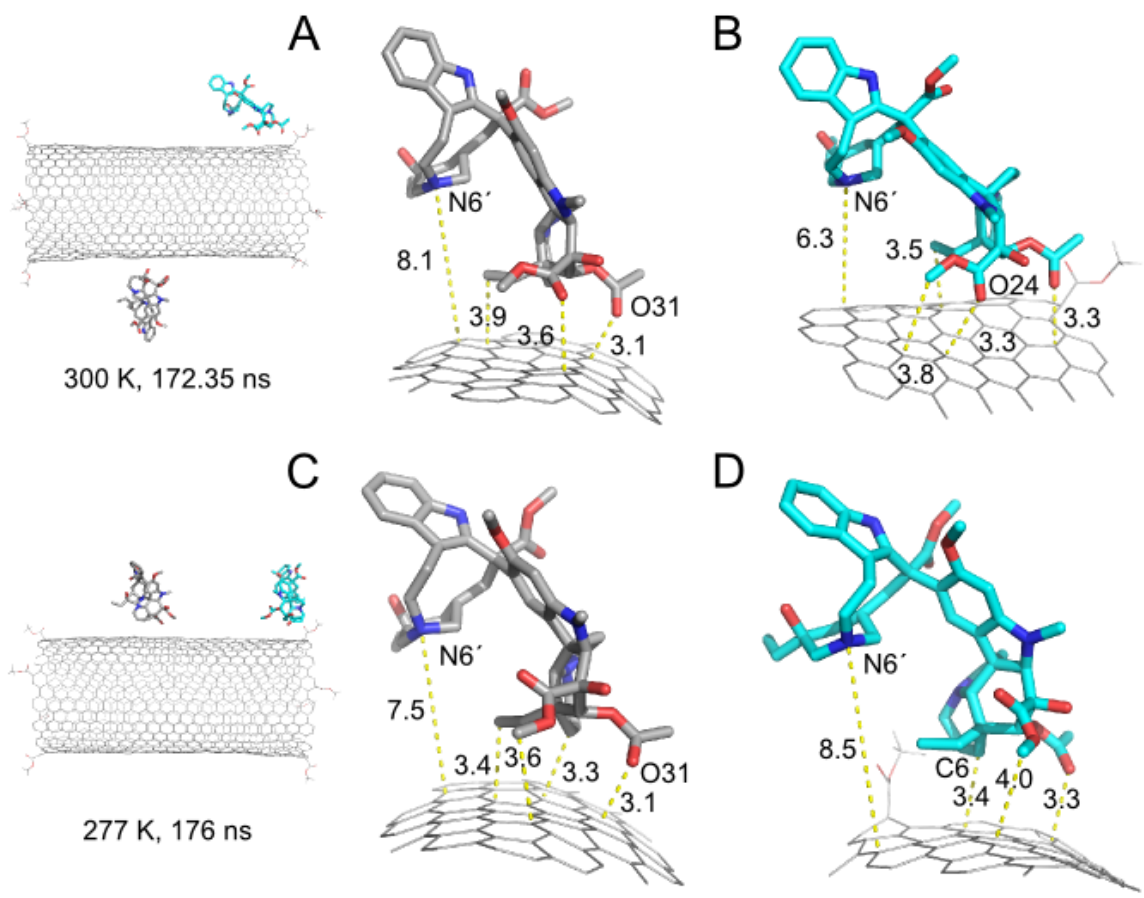


Figure D2 Stable orientations of (A) VLB1 and (B) VLB2 at 300 K as well as (C) VLB1 and (D) VLB2 at 277 K with respect to fSWNT sidewall. Dashed lines indicate the nearest distance to the sidewall in Å. VLB1 is in gray and VLB2 is in cyan.

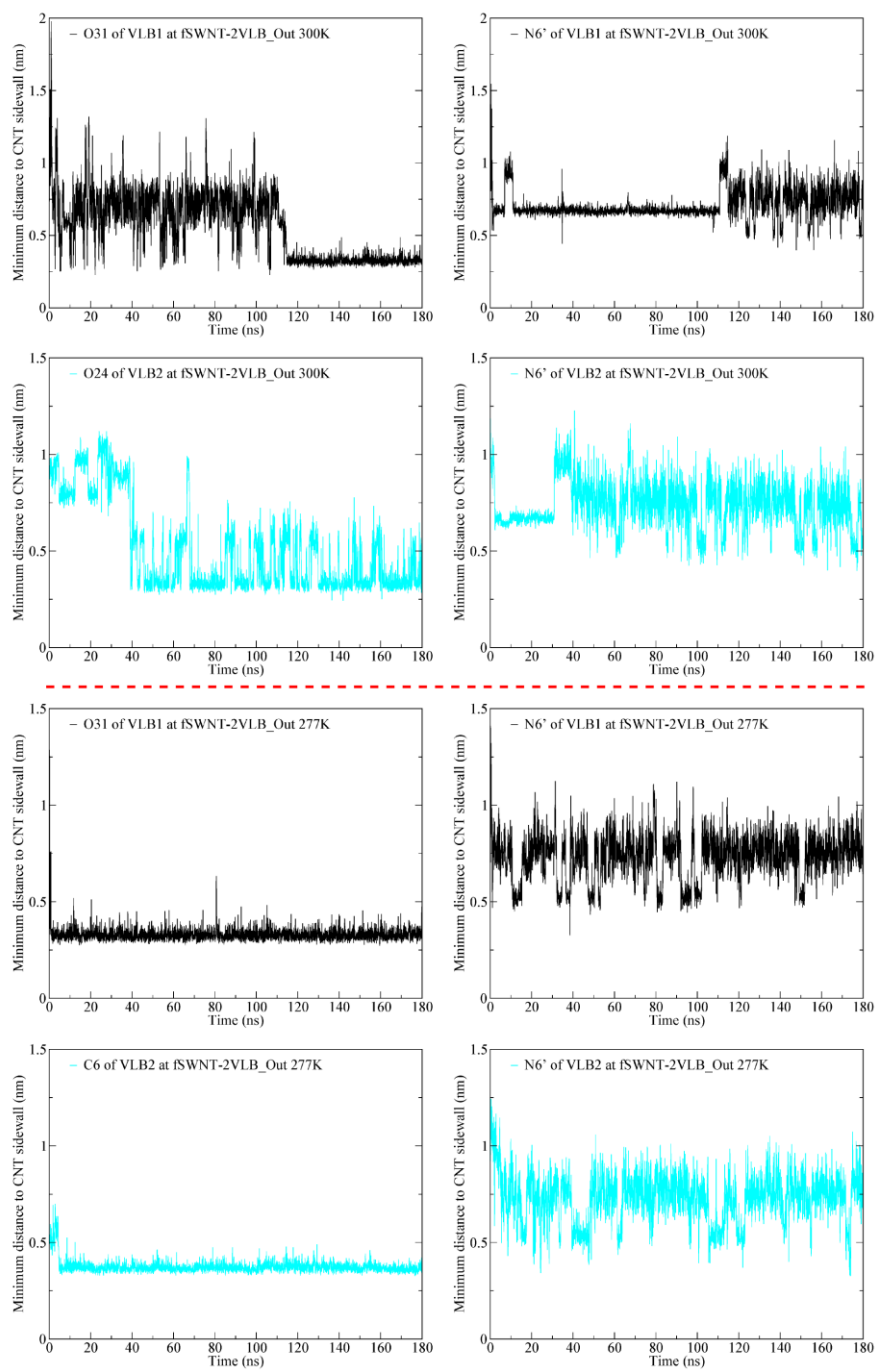


Figure D3 The distances between selected atoms in VLB1 and VLB2 and CNT sidewall for fSWNT-2VLB at 300 K (above dashed red line) and 277 K (below dashed red line). VLB1 is in black and VLB2 is in cyan.

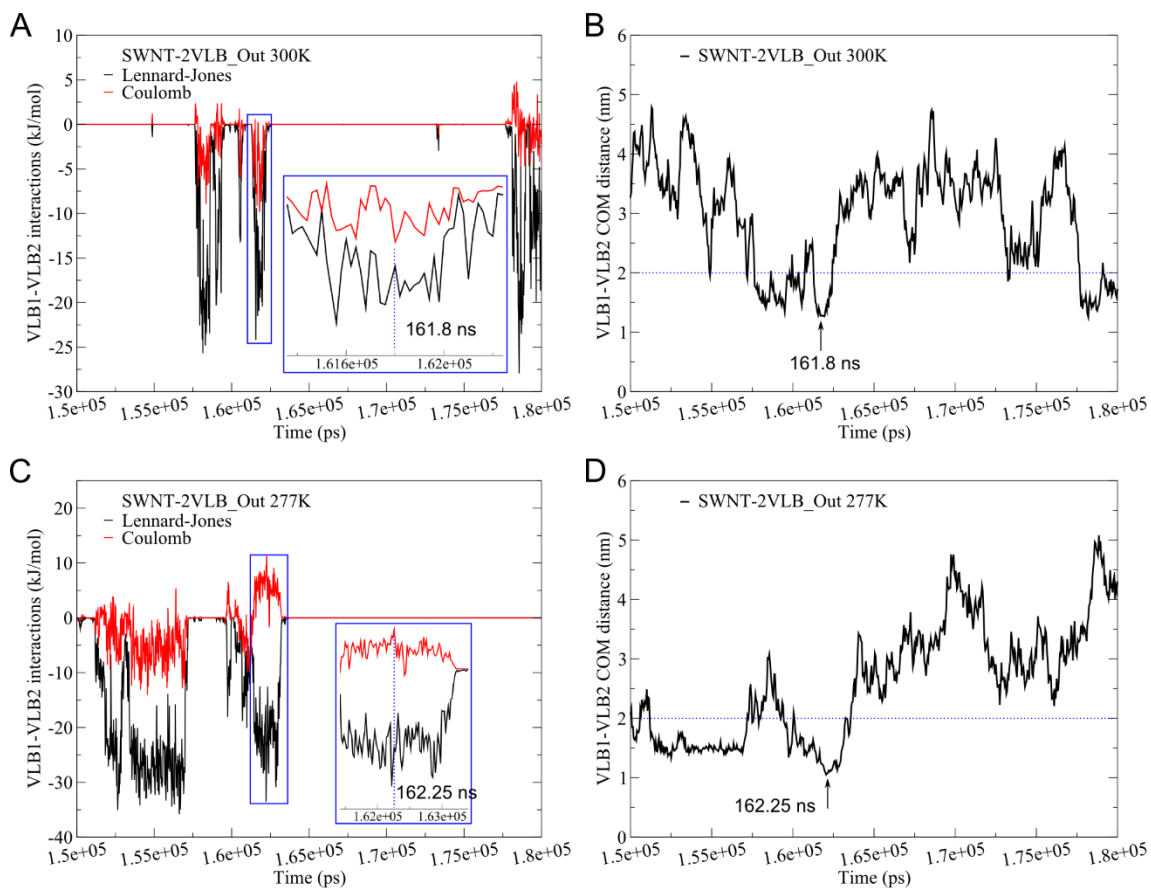


Figure D4 LJ and Coulomb interactions between VLB1 and VLB2 in SWNT-2VLB_Out at (A) 300 K and (C) 277 K. The corresponding COM distance between VLB1 and VLB2 changing from 150 to 180 ns at (B) 300 K and (D) 277 K. The inset close-up depicts a range where both interactions are significant. Vertical dashed lines indicate the time frame with relatively strong LJ and Coulomb interactions. Arrows indicate the time corresponding to the minimum COM distance.

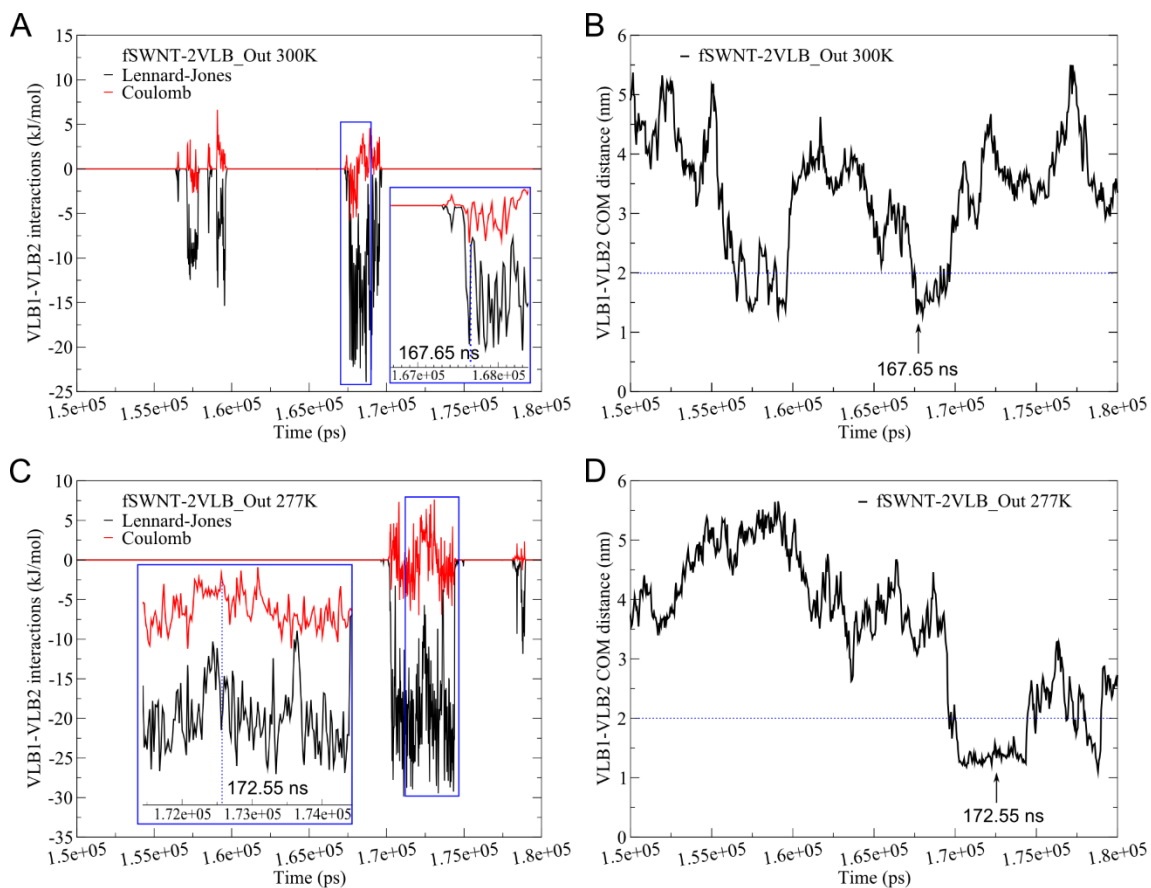


Figure D5 LJ and Coulomb interactions between VLB1 and VLB2 in fSWNT-2VLB_Out at (A) 300 K and (C) 277 K. The corresponding COM distance of VLB1 and VLB2 from 150 to 180 ns at (B) 300 K and (D) 277 K. The enlarged inset in (A) and (C) depict a range where both interactions are significant. Vertical dashed lines indicate the time frame with relatively strong LJ and Coulomb interactions. Arrows indicate the time corresponding to minimum COM distance.

Appendix E

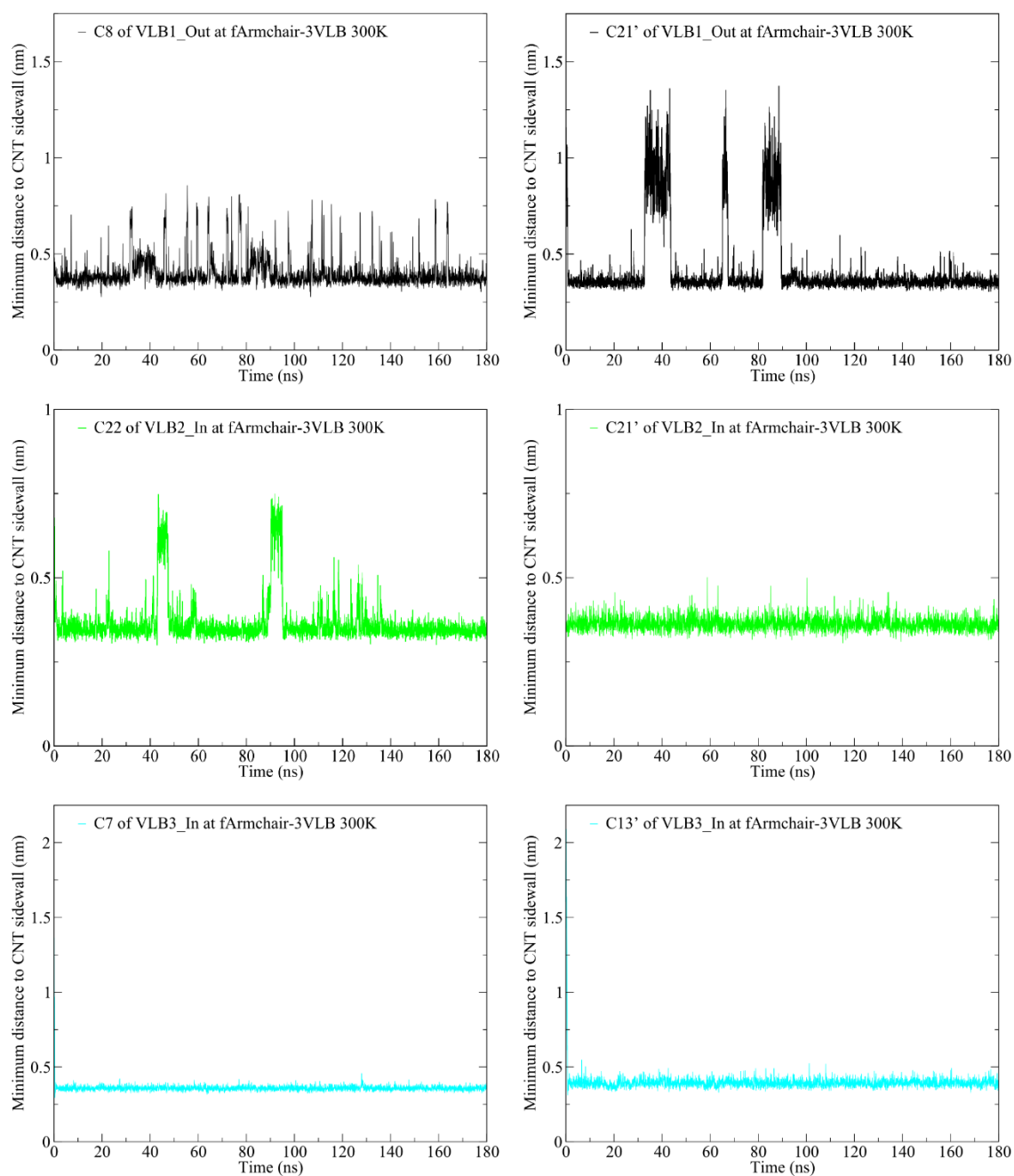


Figure E1 The distances between selected atoms in VLB1, VLB2 and VLB3 and CNT sidewall for fArmchair-3VLB at 300 K. VLB1 is in black, VLB2 is in green and VLB3 is in cyan. (same color code as below)

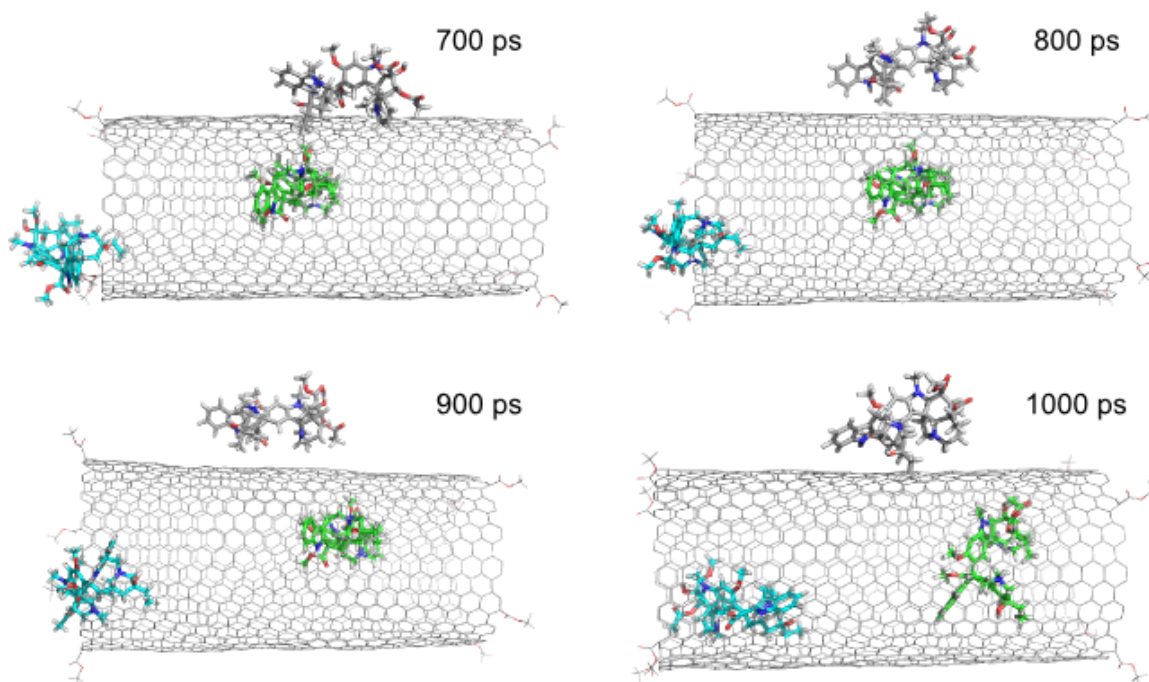


Figure E2 Four frames in the process of VLB3 entering fArmchair SWNT at 300 K.

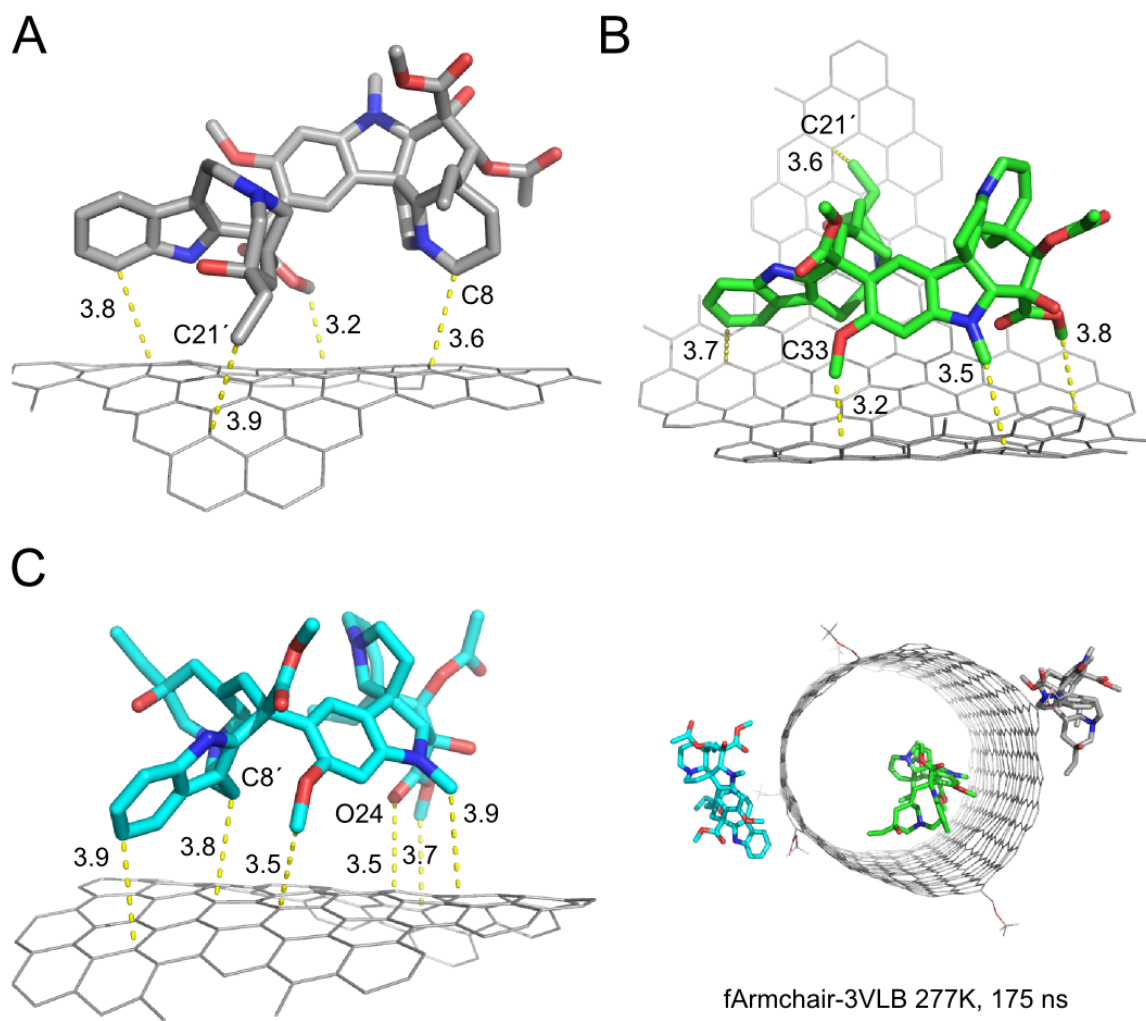


Figure E3 Stable orientations of (A) VLB1, (B) VLB2 and (C) VLB3 at 277 K with respect to fArmchair SWNT. Dashed lines indicate the nearest distance to the sidewall in Å.

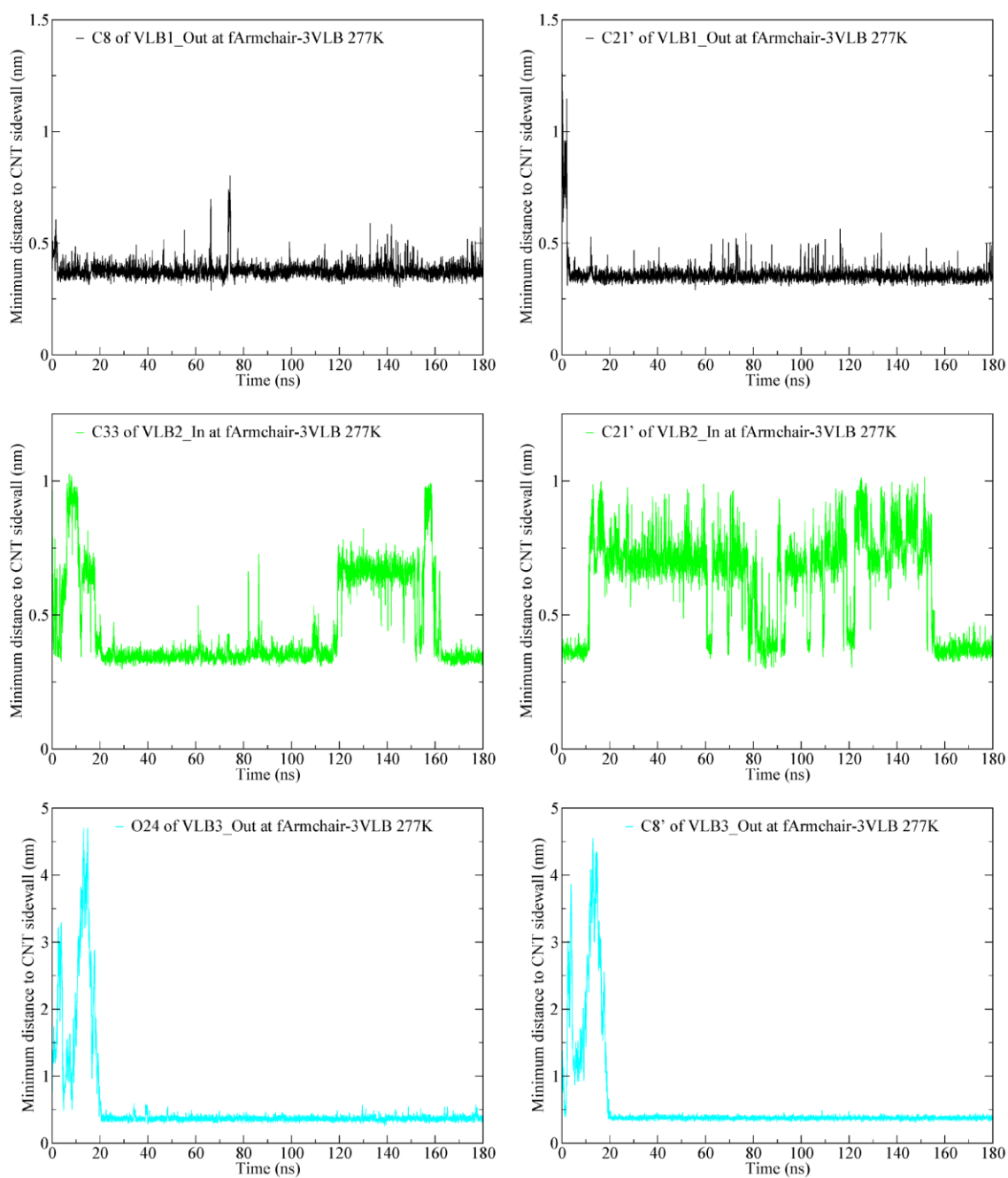


Figure E4 The distances between selected atoms in VLB1, VLB2 and VLB3 and the CNT sidewall for fArmchair-3VLB at 277 K.

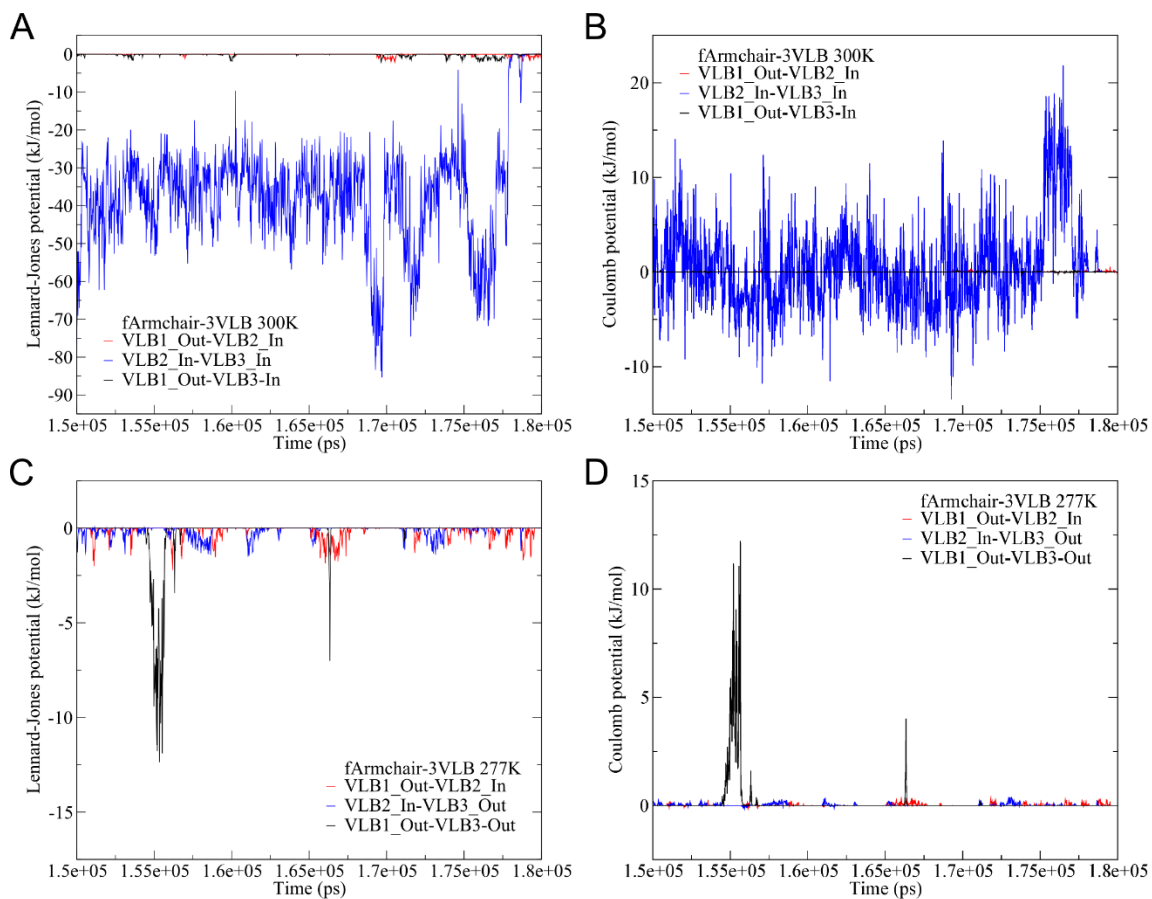


Figure E5 The inter-VLB LJ interactions at (A) 300 K and (C) 277 K as well as the inter-VLB Coulomb interactions at (B) 300 K and (D) 277 K for fArmchair-3VLB.

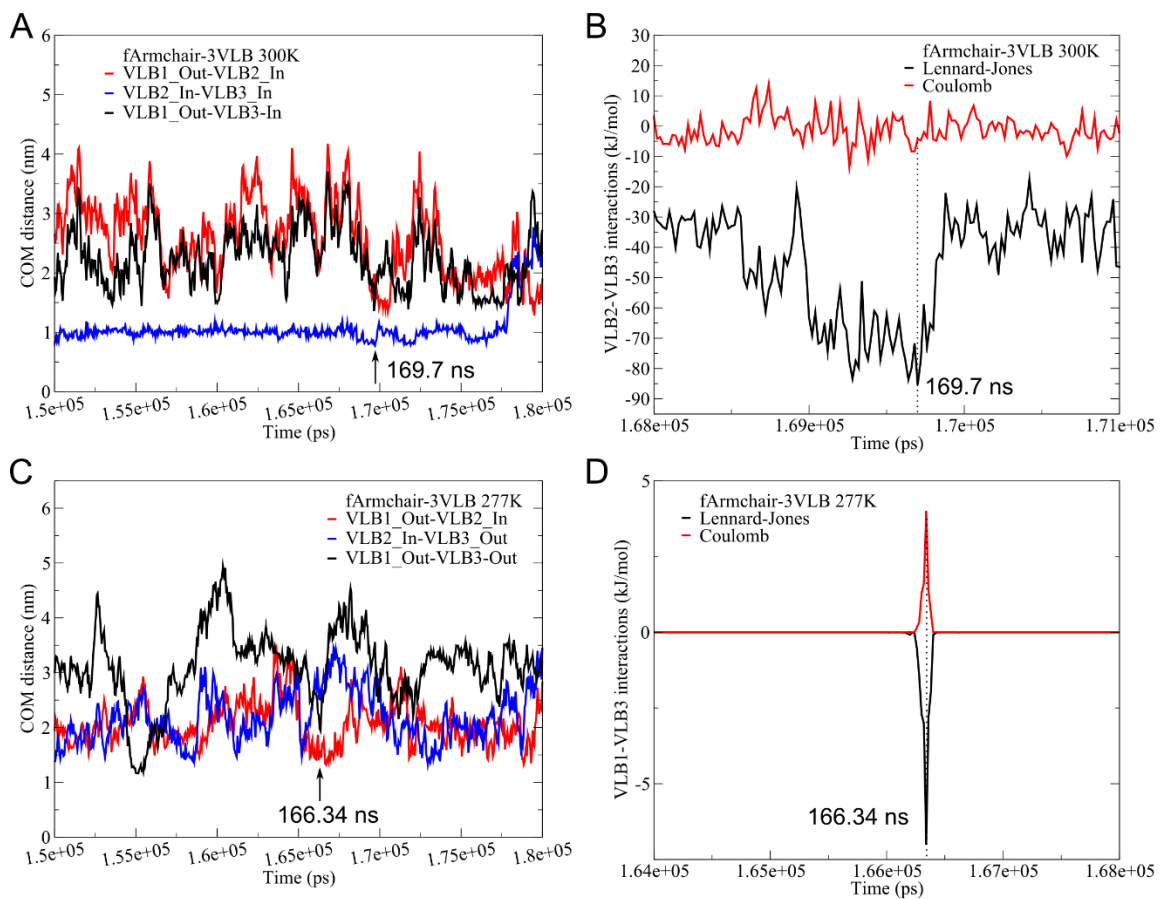


Figure E6 The inter-VLB COM distances among VLB1, VLB2 and VLB3 changing from 150 to 180 ns for fArmchair-3VLB at (A) 300 K and (C) 277 K. The significant inter-VLB interactions at (B) 300 K and (D) 277 K. Arrows indicate the time corresponding to the minimum COM distance.

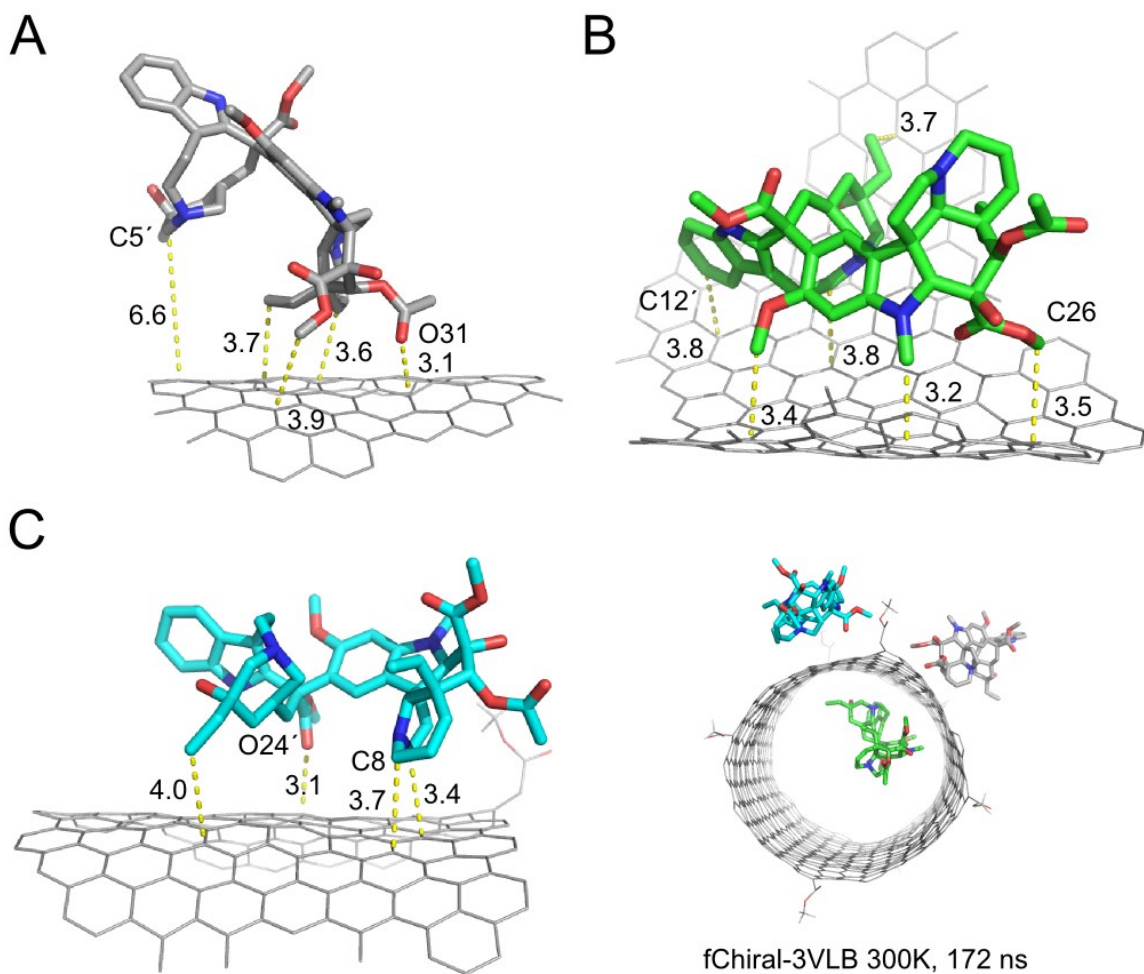


Figure E7 Stable orientations of (A) VLB1, (B) VLB2 and (C) VLB3 at 300 K with respect to fChiral SWNT. Dashed lines indicate the nearest distance to the sidewall in Å. VLB1 is in gray, VLB2 is in green and VLB3 is in cyan.

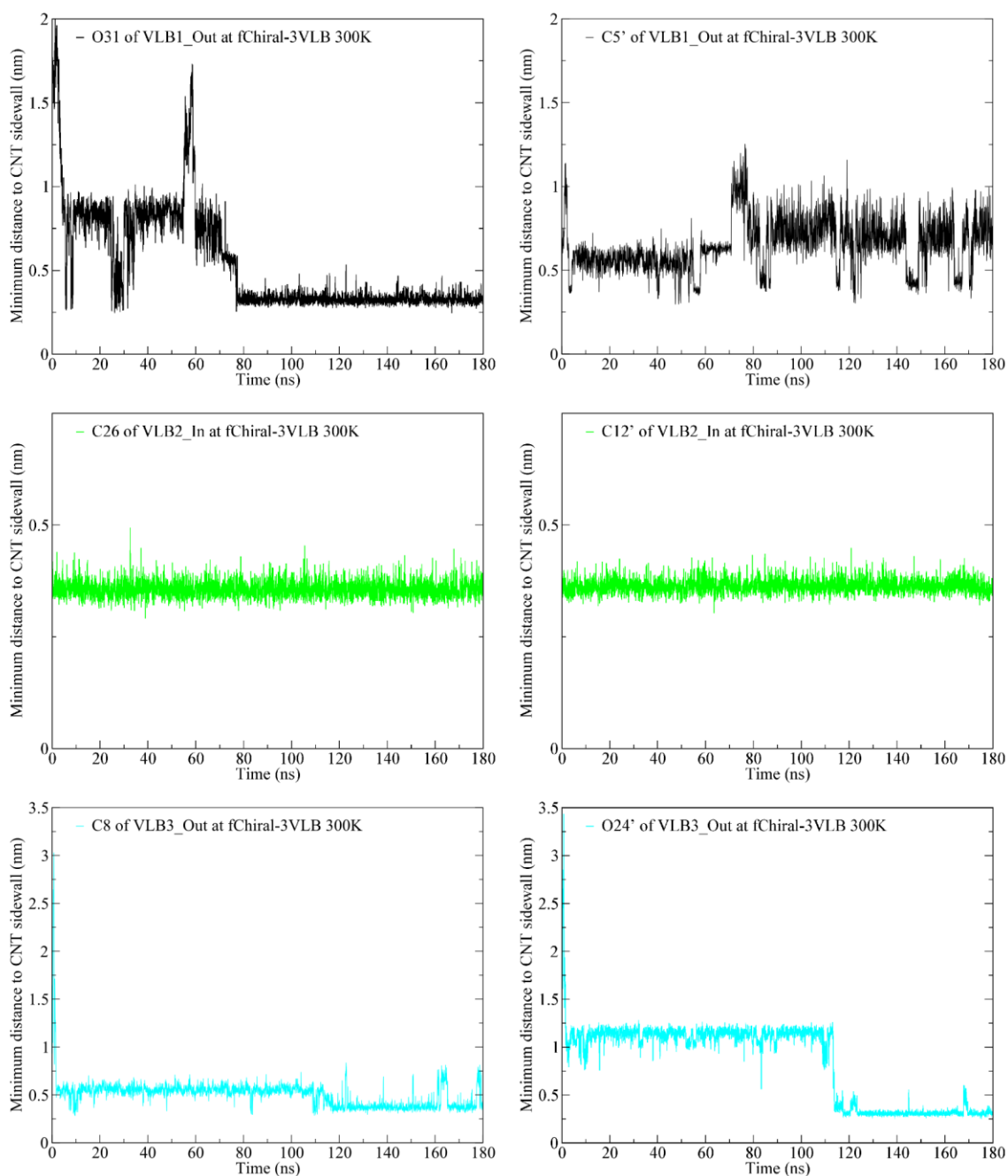


Figure E8 The distances between selected atoms in VLB1, VLB2 and VLB3 and the CNT sidewall of fChiral-3VLB at 300 K.

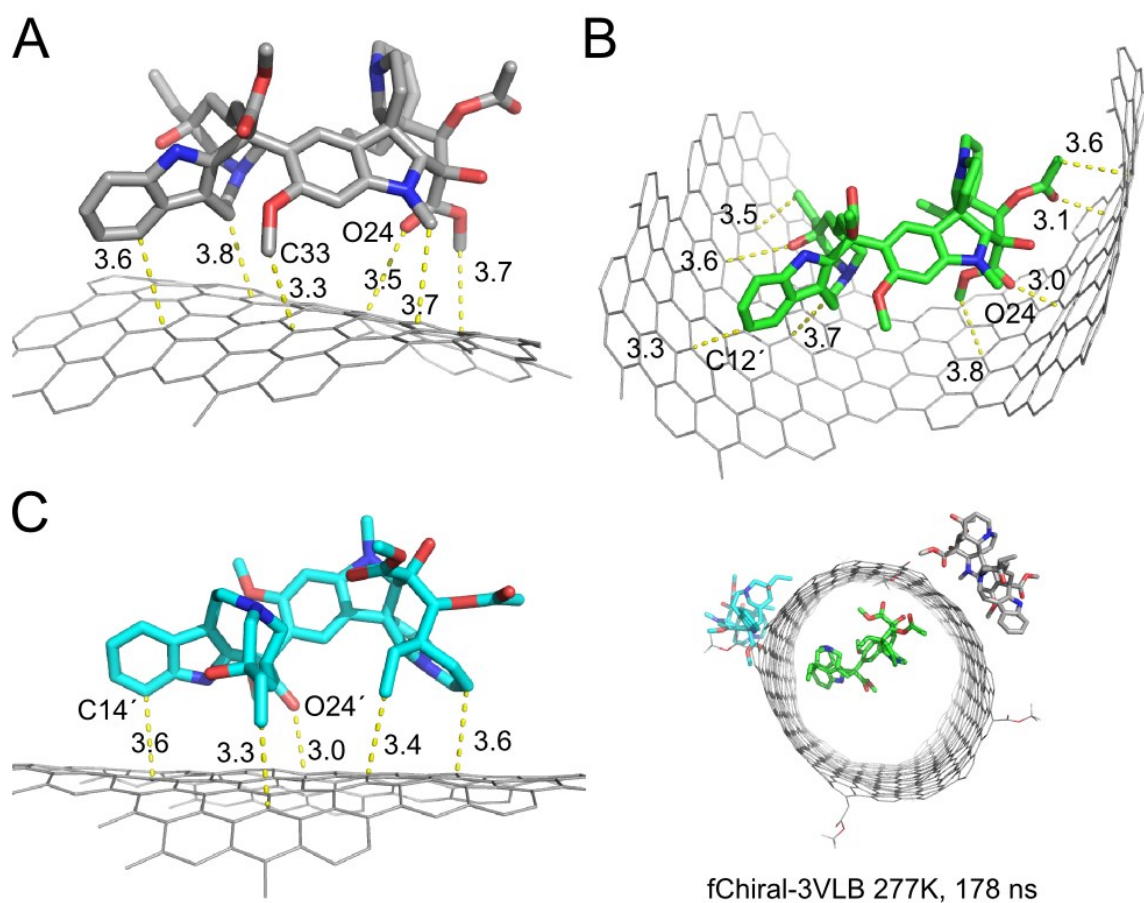


Figure E9 Stable orientations of (A) VLB1, (B) VLB2 and (C) VLB3 at 277 K with respect to fChiral SWNT. Dashed lines indicate the nearest distance to the sidewall in Å. VLB1 is in gray, VLB2 is in green and VLB3 is in cyan.

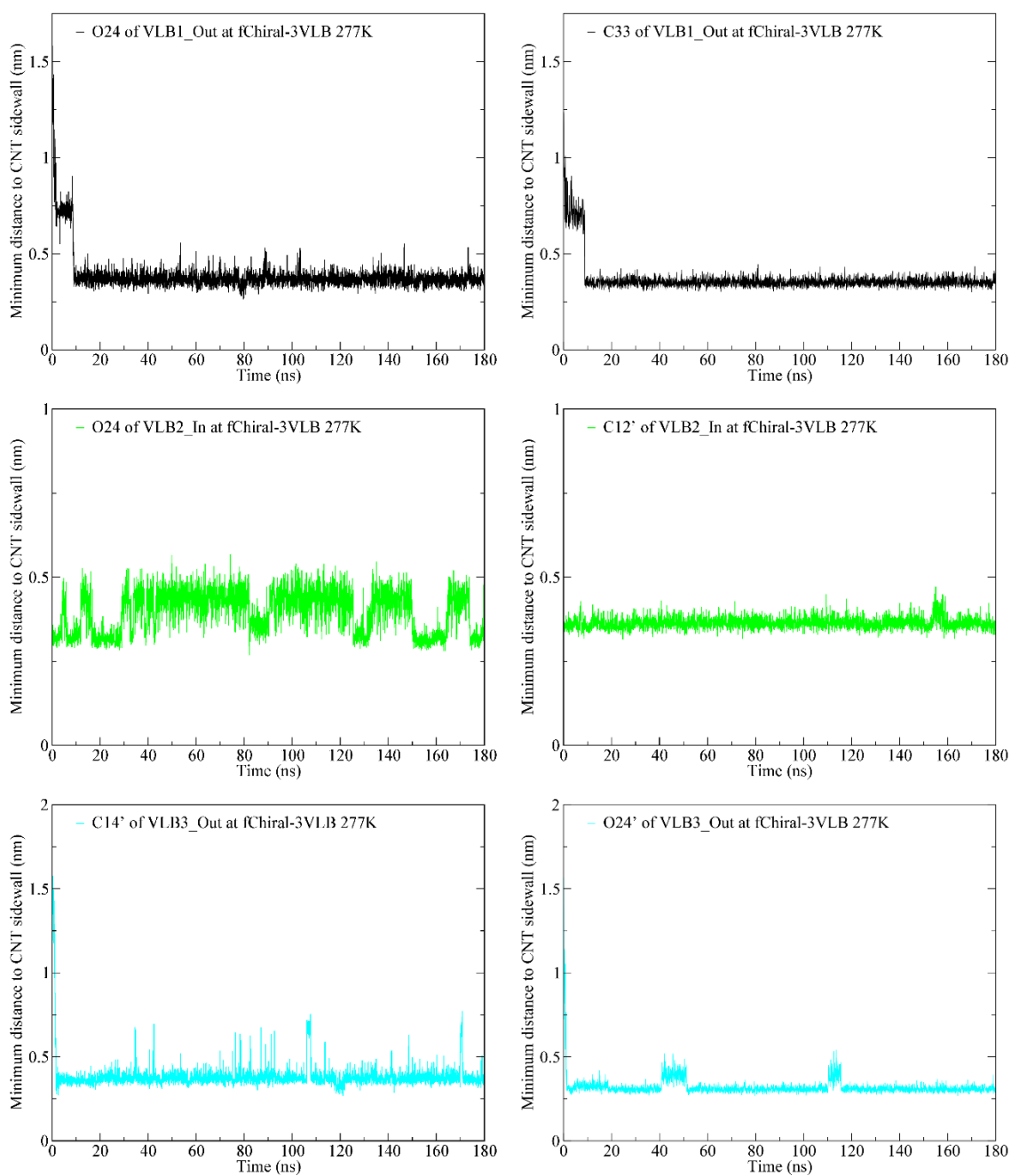


Figure E10 The distances between the selected atoms in VLB1, VLB2 and VLB3 and the CNT sidewall for fChiral-3VLB at 277 K.

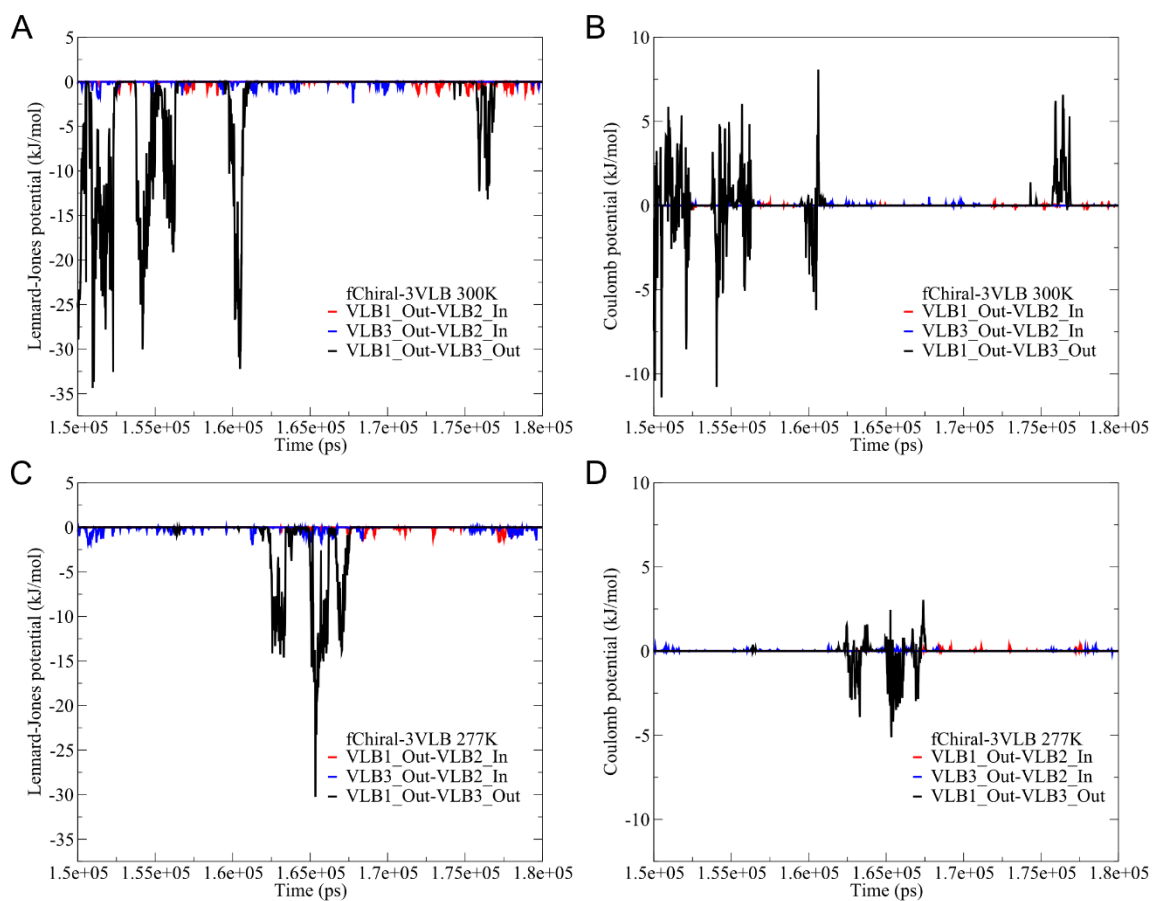


Figure E11 The inter-VLB LJ interactions at (A) 300 K and (C) 277 K as well as the inter-VLB Coulomb interactions at (B) 300 K and (D) 277 K for fChiral-3VLB.

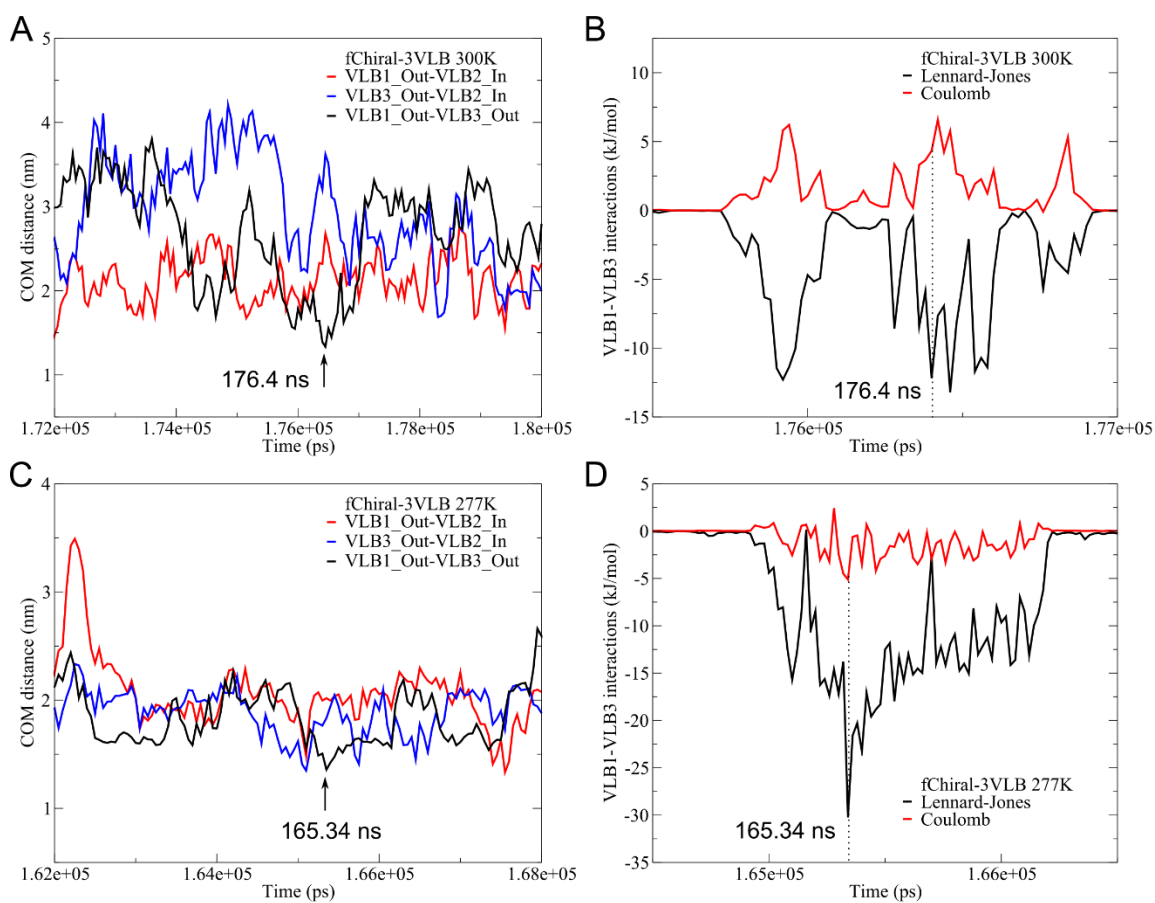


Figure E12 The inter-VLB COM distances changing from 150 to 180 ns for fChiral-3VLB at (A) 300 K and (C) 277 K. The significant VLB1-VLB3 interactions at (A) 300 K and (C) 277 K. Numbers indicate the time corresponding to the minimum COM distance.

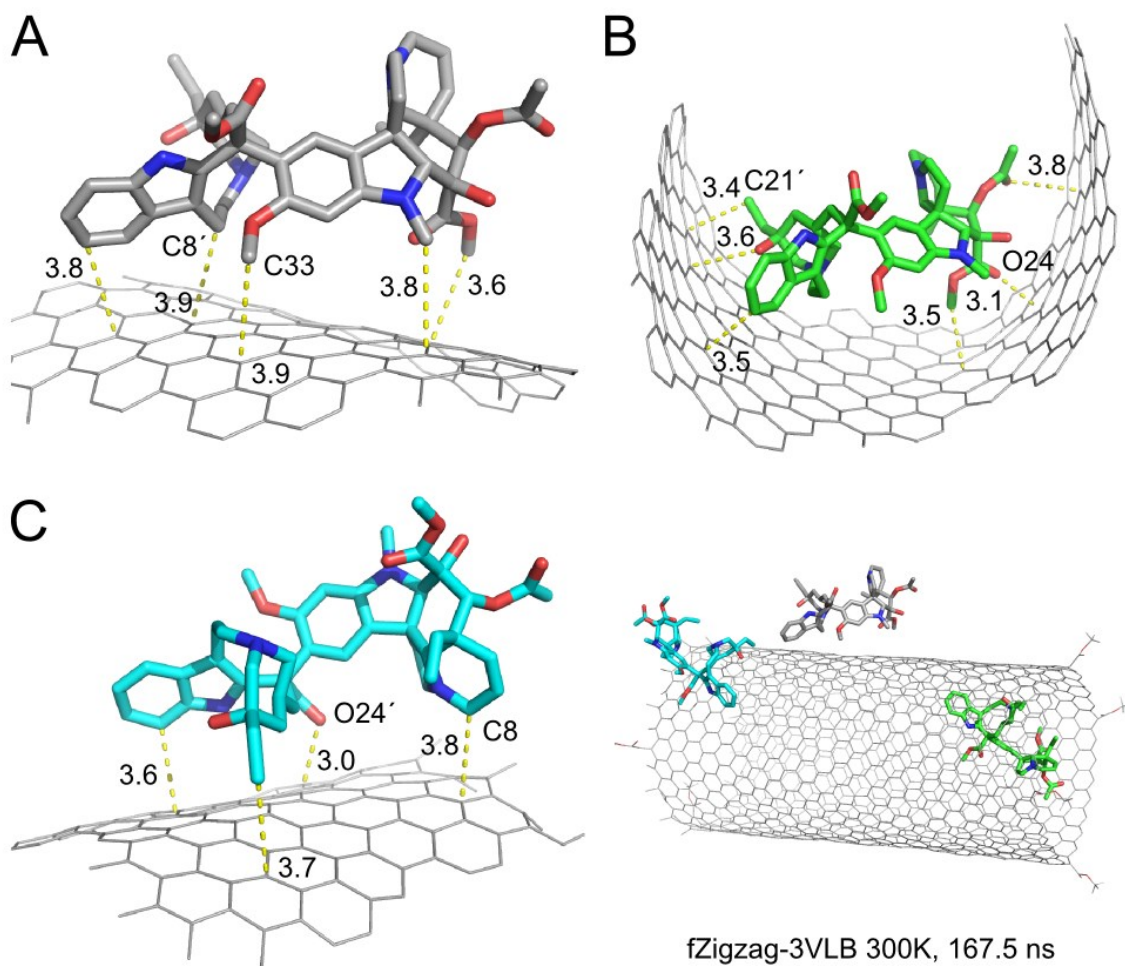


Figure E13 Stable orientations of (A) VLB1, (B) VLB2 and (C) VLB3 at 300 K with respect to fZigzag SWNT. Dashed lines indicate the nearest distance to the sidewall in Å.

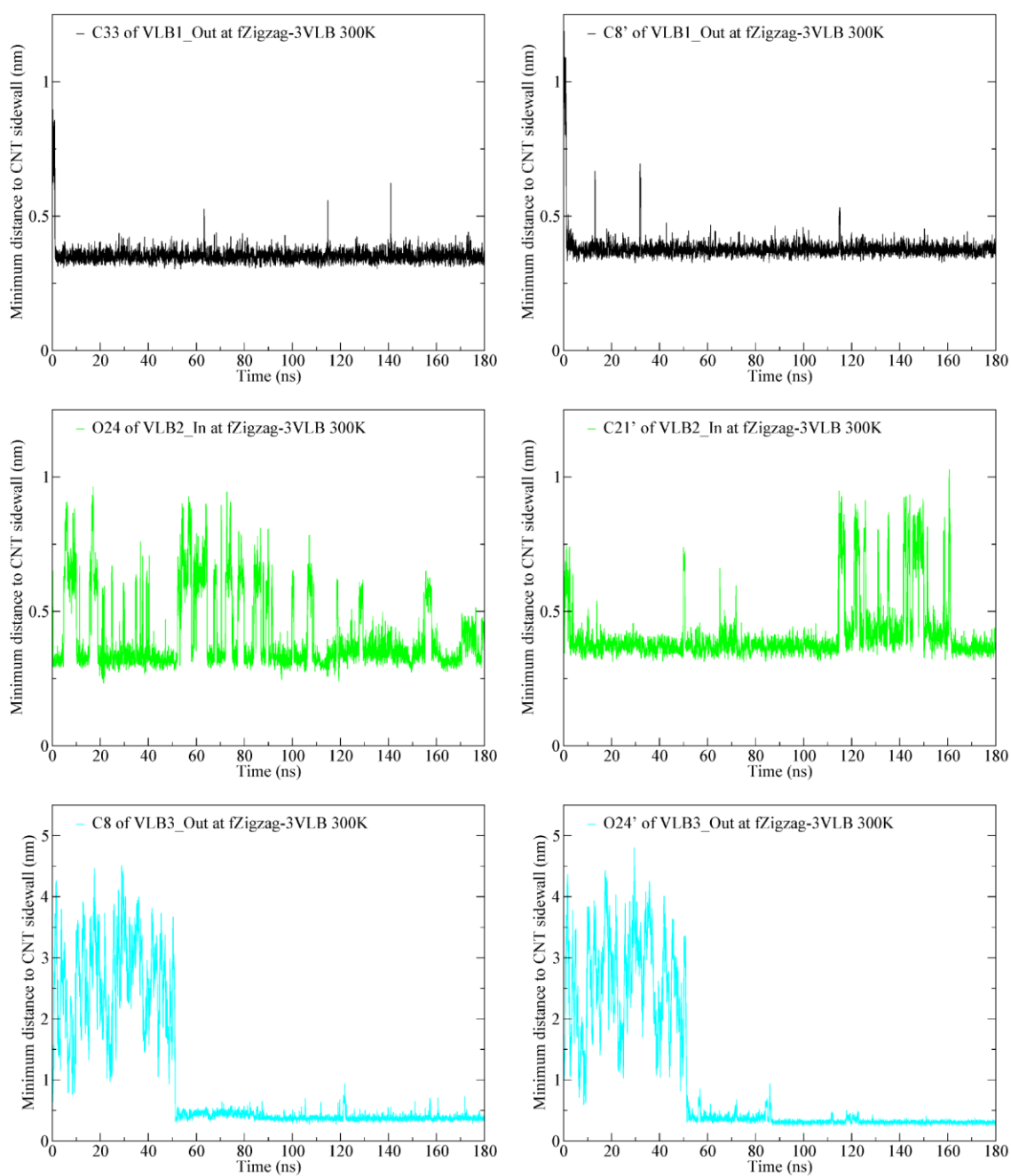


Figure E14 The distances between the selected atoms in VLB1, VLB2 and VLB3 and the CNT sidewall for fZigzag-3VLB at 300 K.

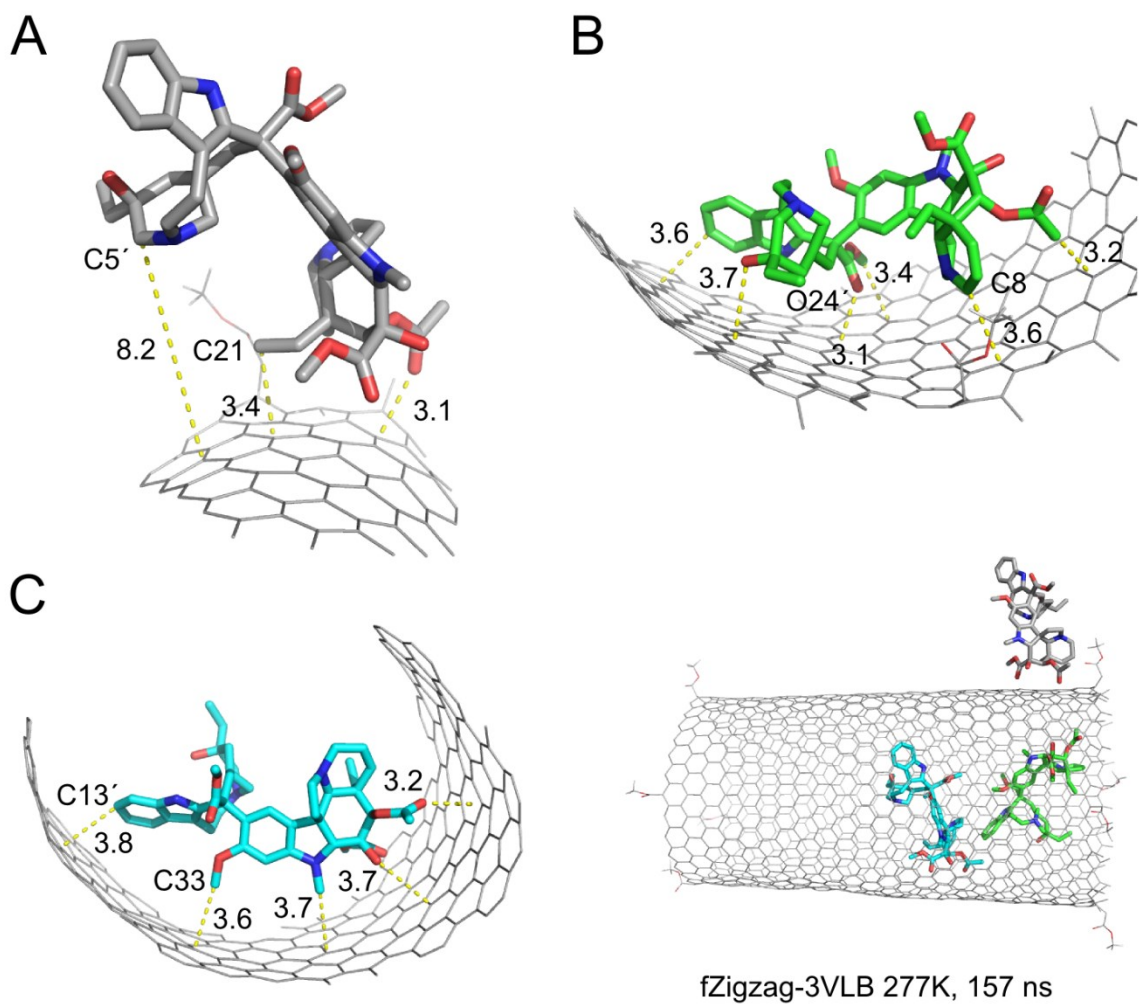


Figure E15 Stable orientations of (A) VLB1, (B) VLB2 and (C) VLB3 at 277 K with respect to fZigzag SWNT. Dashed lines indicate the nearest distance to the sidewall in Å.

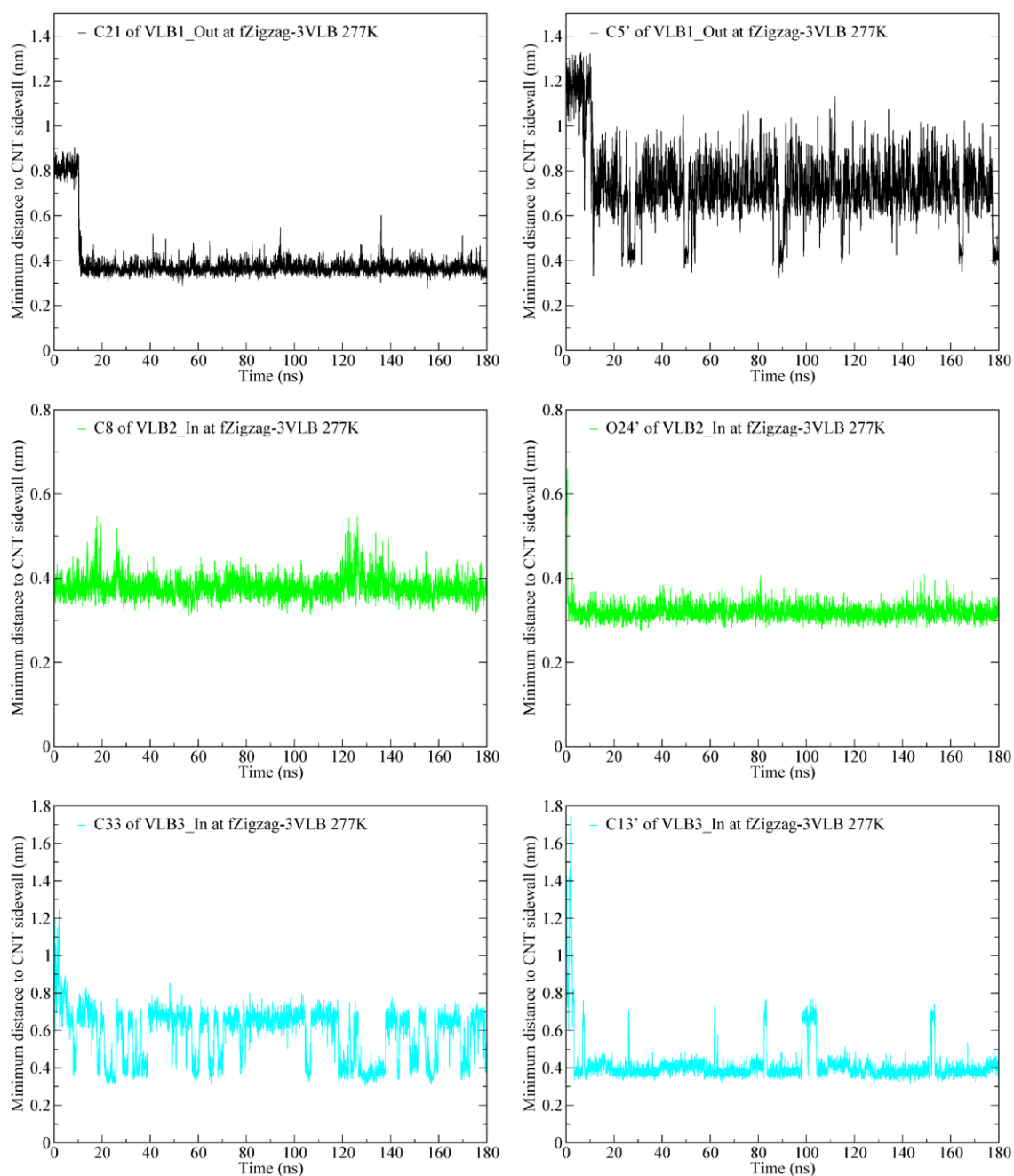


Figure E16 The distances between the selected atoms in VLB1, VLB2 and VLB3 and the CNT sidewall for fZigzag-3VLB at 277 K.

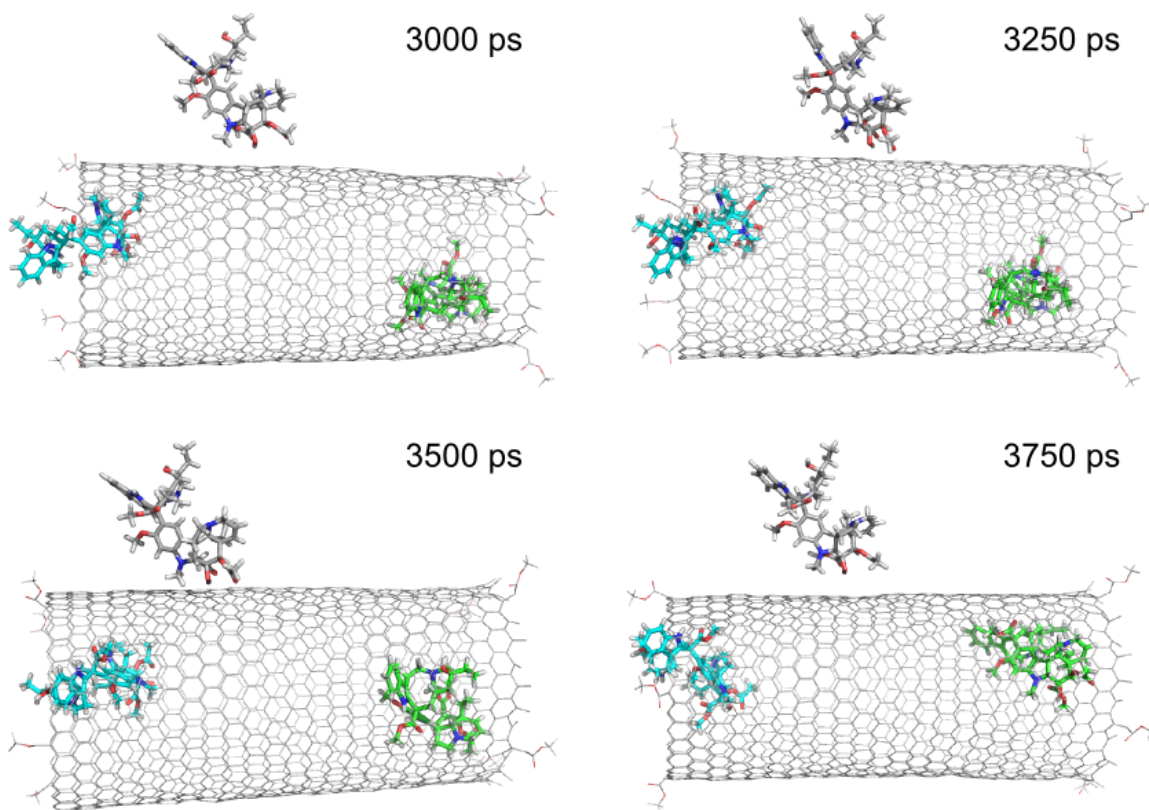


Figure E17 Four frames in the process of VLB3 entering fZigzag SWNT at 277 K.

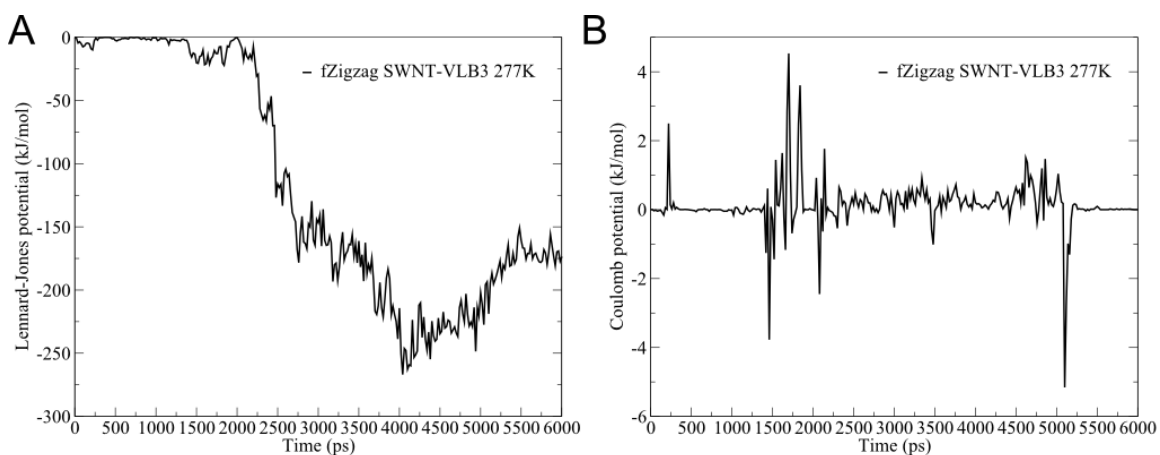


Figure E18 (A) LJ and (B) Coulomb interactions between fZigzag SWNT and VLB3 in the process of VLB3 entering the tube.

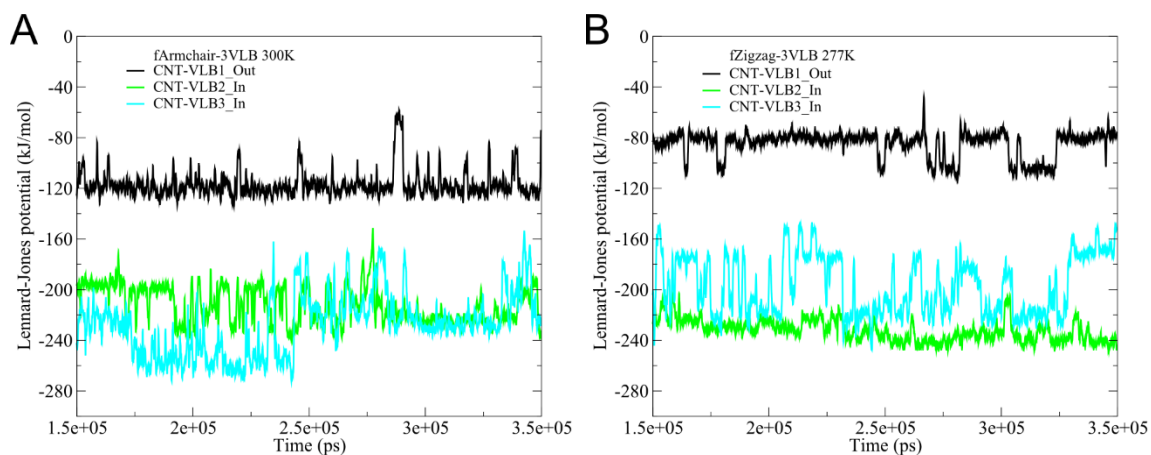


Figure E19 The LJ interactions between CNT and VLB molecules of (A) fArmchair-3VLB at 300 K and (B) fZigzag-3VLB at 277 K, after the convergence of MD simulations until the extension to 350 ns. VLB1 is in black, VLB2 is in green and VLB3 is in cyan.